Università di Roma · La Sapienza

FACOLTA' DI SCIENZE MATEMATICHE, FISICHE E NATURALI

Corso di Laurea in Astronomia e Astrofisica

Study of the high energy Cosmic Rays large scale anisotropies with the ANTARES neutrino telescope

Dissertazione di Laurea Magistrale

Relatore:
Prof. Antonio Capone

Autore:
Giulia Illuminati

ANNO ACCADEMICO 2014-2015

Contents

Chapter 1

Introduction

Cosmic rays in the TeV to PeV range are mainly charged particles that contribute an energy density in the Galaxy of about 1 eV cm $^{-3}$, believed to originate in our Galaxy, possibly in local astrophysical accelerators such as supernova remnants. After escaping from their sources, cosmic rays propagate through the interstellar medium where they are deflected from their original direction due to the presence of magnetic fields. This scattering process efficiently isotropizes the trajectories of cosmic rays before their arrival at Earth. However, it is predicted that a dipolar anisotropy with an amplitude of $\sim 10^{-3}$ or lower should subsist in their arrival directions. Such a large-scale anisotropy was observed for the first time at TeV energies by detectors in the Northern hemisphere, e.g. Milagro, Tibet and Super- Kamiokande and then, in the Southern hemisphere, using data from IceCube. The measured deviation from an isotropic distribution is of the order of 0.1% and the excess region and deficit region have the size of several tens degrees. The cosmic-ray muon spatial distribution at these energies may be not isotropic for different reasons, like the instabilities related to temperature and pressure variations in the Earth's atmosphere. Moreover, at cosmic-ray energies lower of around one TeV the movements of solar plasma through the heliosphere may change the Earth's magnetic field, causing a modulation of the cosmic-ray anisotropy. Furthermore the Compton- Getting effect predicts a dipole effect due to the moving of the Earth with respect to an isotropic cosmic-ray rest system. If the Earth is moving in the rest system, the cosmic ray flux from the forward direction becomes larger.

The aim of this work is to analyse data collected so far by the ANTARES neutrino telescope in order to search for a large scale anisotropy in the arrival direction of CRs on the celestial sphere. The ANTARES neutrino telescope, located in the Northern hemisphere, at a depth of 2475m in the Mediterranean Sea, about 40 km off the French coast near Toulon, can detect down-going muons from the North as the above mentioned detectors. It consists of an array of 12 lines anchored to the sea bed, each supporting 25 storeys made of triplets of 10-inch photomultipliers (PMTs). Its main purpose is to detect high energy neutrinos from galactic or extragalactic sources. Neutrinos are detected indirectly through the detection of Cherenkov light produced by the path in water of relativistic muons emerging from charged-current muon neutrino interactions in the surroundings. Although ANTARES is optimized for upward-going particle detection, the most abundant data sample is due to the atmospheric down-going

muons produced in air showers induced by interactions of primary cosmic- rays in the Earth's atmosphere. Muons with energies above around 500 GeV at the sea level can reach the detector, inducing enough Cherenkov light to reconstruct the direction of the muon. The muons represent a high statistic data set that can provide information about primary cosmic rays at energies above few TeV.

The sidereal variation of the CR intensity is induced by the anisotropy in their arrival direction. However, it can also be caused by the detector exposure asymmetries, non-uniform time coverage, diurnal and seasonal variation of the atmospheric temperature. The main challenge for this analysis is accounting for the detector asymmetry, and unequal time coverage in the data due to the detector run selection. This geometrical asymmetry results in a preferred reconstructed muon direction since the muons would pass by more strings in one direction in the detector compared to another. The combination of detector asymmetry with a non-uniform time coverage would induce an azimuthal asymmetry and consequently artificial anisotropy of the arrival direction of cosmic rays. Moreover the combined effect of atmosphere, sea and detector modifies the measured coszenith muons distribution, expected to be uniform at the entrance into the atmosphere for the incoming CRs. After correcting for spacial effects, further corrections are needed in order to take into account that the atmospheric temperature fluctuations can affect the observed muon fluxes. Indeed, the density in the upper atmosphere is related to the temperature and so the relative probability for a meson to decay or to interact is also a function of the temperature. This time variations of the cosmic-ray muon flux could mimic a flux anisotropy. Once all these corrections have been applied, it will be possible to observe the obtained rate of events in equatorial coordinates and a study of the rate modulation along the R.A. will be performed by means of harmonic functions.

Chapter 2

Cosmic Rays

Cosmic rays are high energy charged particles, originating in outer space, that travel at nearly the speed of light and strike the Earth from all directions. Most cosmic rays are the nuclei of atoms, ranging from the lightest to the heaviest elements in the periodic table. Cosmic rays also include high energy electrons, positrons, and other subatomic particles. The term "cosmic rays" usually refers to galactic cosmic rays, which originate in sources outside the solar system, distributed throughout our Milky Way galaxy. However, this term has also come to include other classes of energetic particles in space, including nuclei and electrons accelerated in association with energetic events on the Sun (called solar energetic particles), and particles accelerated in interplanetary space. Their discovery is commonly attributed to the Austrian physicist Viktor Hess (1912) when, after many balloon flights, he found that an electroscope on board discharged considerably with height. Hess concluded that the increase of the ionization with altitude was originated by radiation coming from space [1]. Moreover, the absence of day-night variations excluded the Sun as a possible source. Hess, after his results were confirmed by W. Kolhorster in a number of flights up to 9200 m, was awarded the Nobel Prize in physics in 1936 for the discovery of the *cosmic rays*.

2.1 Energy Spectrum

The cosmic radiation incident at the top of the terrestrial atmosphere includes all stable charged particles and nuclei with lifetimes of the order of 10^6 years or longer. Technically, "primary" cosmic rays are those particles accelerated at astrophysical sources and "secondaries" are those particles produced in interaction of the primaries with interstellar gas. Thus electrons, protons and helium, as well as carbon, oxygen, iron, and other nuclei synthesized in stars, are primaries. Nuclei such as lithium, beryllium, and boron (which are not abundant end-products of stellar nucleosynthesis) are secondaries. Antiprotons and positrons are also in large part secondary. The energy spectrum of cosmic rays, shown in fig. 2.1, spans ten orders of magnitude in particle energy and about thirty orders of magnitude in flux.

At energies larger than few GeV the energy dependence of the spectrum can be described as a power law of the form $\Phi(E) = K(\frac{E}{1\mathrm{GeV}})^{-\alpha}\ \frac{particles}{\mathrm{cm}^2\ \mathrm{s}\ \ \mathrm{sr}\ \ \mathrm{GeV}}$,

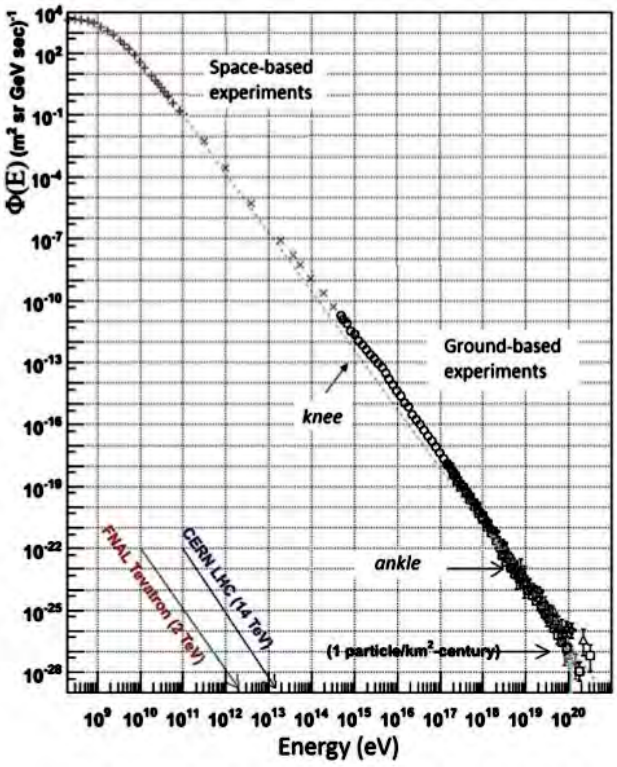

Figure 2.1: The differential energy spectrum $\Phi(E)$ (units: particles/m^2 sr s GeV) of cosmic rays over eleven decades of energy. The *red/blue arrows* indicate the equivalent center of mass energy reached at the Tevatron collider at Fermilab and at the LHC collider at CERN. The *dashed line* shows a E^{-3} spectrum.

where E is the primary cosmic-ray energy, α is the spectral index, and K is a normalization factor. Although the spectrum is remarkably smooth given its wide energy range, some features in the spectral slope are observed [2] [3] [4] at different energies:

- $\alpha = 2.67$ if $E < 10^{15}$eV;
- $\alpha = 3.10$ if $10^{15}eV < E < 10^{18}$eV;
- $\alpha = 2.6$ if $E > 10^{18}$eV.

The first important feature, the spectral softening at energies around 3×10^{15} eV, is usually referred to as the cosmic ray "knee." It is believed that cosmic rays up to this energy originate inside our galaxy and that the change in spectral index is associated with a change in the chemical composition of the cosmic ray particles. The second change in the spectral index is a spectral hardening at an energy of a few EeV, known as the "ankle." Based on magnetic confinement arguments, it is believed that cosmic rays with energies beyond the ankle cannot be confined in the galaxy volume by the galactic magnetic field and so this break could mark the transition between galactic and extragalactic cosmic rays. The

Larmor radius for a particle with charge $q = eZ$, velocity $v = \beta c$, immersed in a magnetic field B, is given by:

$$R_L = \frac{E}{Z|e|\vec{B}\beta c} \tag{2.1}$$

As the Galaxy is filled with a magnetic field whose average intensity is $B \sim 4\mu$G, we obtain the following Larmor radii for protons at different energies:

$$\begin{aligned} R_L(E = 10^{12}\text{eV}) &= 10^{15}\text{cm} = 3 \times 10^{-4}\ \text{pc} \\ R_L(E = 10^{15}\text{eV}) &= 10^{18}\text{cm} = 0.3\ \text{pc} \\ R_L(E = 10^{18}\text{eV}) &= 10^{21}\text{cm} = 300\ \text{pc} \end{aligned} \tag{2.2}$$

These values of R_L should be compared with the Galaxy dimensions. Particles below 10^{18} eV are strongly constrained inside the galactic volume by the galactic magnetic field since the Larmor radius for this energies is comparable to the dimension of the Galactic disk (fig. 2.2).

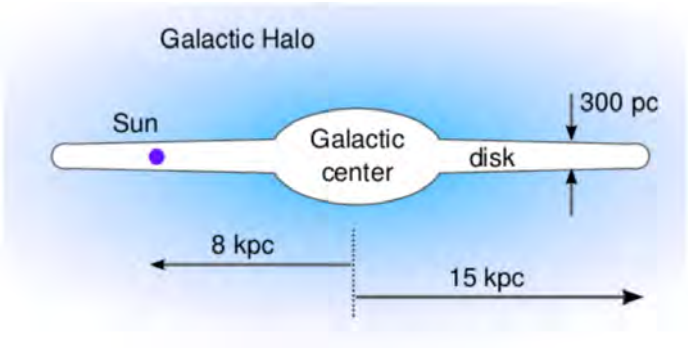

Figure 2.2: Simplified model of the structure of the Milky Way galaxy.

The flux is then strongly suppressed at energies above 4×10^{19} eV [5]. A spectral cutoff of this nature was originall1y theorized in 1966 by K. Greisen, V. Kuzmin and G. Zatsepin (GZK cut-off) [6] [7]. They foresaw that the flux of CRs originating at cosmological distances would greatly be attenuated above a threshold energy $E_{GZK} = 5 \times 10^{19}$ eV since, during propagation, protons would interact with 2.7 K Cosmic Microwave Background (CMB) photons, producing the Δ^+ resonance. The Δ^+ then immediately decays in one of the following final states:

$$p + \gamma \longrightarrow \Delta^+ \longrightarrow \pi^0 + p \tag{2.3}$$

$$p + \gamma \longrightarrow \Delta^+ \longrightarrow \pi^+ + n \tag{2.4}$$

Since the produced neutrons decay into $pe^-\nu_e$, a proton is always present in the final state, so the overall effect of the interaction is that the energy of the CR proton above threshold is reduced and high-energy photons and neutrinos are produced ($\pi^0 \to \gamma\gamma, \pi^+ \to \nu_\mu\mu^+, \mu^+ \to e^+\nu_e\bar{\nu_\mu}$). This process limits the *energy loss lenght* ($l^{-1} = \frac{1}{E}\frac{dE}{dx}$) of protons with energies higher than the threshold energy for pion-production to a few tens of Mpc:

$$l_{p\gamma} = \frac{1}{y \times \sigma_{p\gamma} \times n_{\gamma_{CMB}}} = 30\text{Mpc} \tag{2.5}$$

where

- $y = \frac{(E-E')}{E} = \frac{\Delta E_p}{E} \sim \frac{m_\pi}{m_p} \simeq 0.1$ is the fraction of energy lost per interaction and can be qualitatively estimated considering that in the final state of the process a proton and a pion are present;
- $\sigma_{p\gamma} \simeq 250\mu$b is the cross-section of the processes $\gamma p \to \pi^0 p$ and $\gamma p \to \pi^+ n$, studied in laboratory as a function of the photon energy in the laboratoty frame [9].
- $n_\gamma \simeq 400\text{cm}^{-3}$ is the CMB photons number density.

Therefore only photons with energy below $\sim 10^{20}$ eV can arrive on Earth coming from a distance larger than ~ 30 Mpc. The eventual detection of CR protons with energy exceeding that value corresponds to particles originated in sources nearer than the Virgo cluster.

The GZK cut-off is not the only effect that can affect the CR energy spectrum: at least other two aspects have to be considered [8]. During the propagation, protons can scatter off CMB photons and an electron-positron couple can be produced in the process

$$p + \gamma \longrightarrow p + e^+ + e^- \tag{2.6}$$

with a threshold energy given by $E_p \geq \frac{m_e m_p}{E_\gamma} \simeq 2 \times 10^{18}$ eV where E_γ is the average energy of the CMB photon. The cross section of this process is comparable with that of the production of the Δ^+ resonance, while the fraction of energy loss has a value about two orders of magnitude smaller giving rise to an average energy loss length about two orders of magnitude larger ($\sim 10^3$ Mpc). Finally, an adiabatic energy loss that is independent on CRs energy is due to the expansion of the Universe: $l_{ad} = \frac{c}{H_0} \simeq 4$ Gpc where c is the light velocity and $1/H_0 \sim 13.7$ Gy is the Hubble time. Fig. 2.3 shows the energy loss lenght for the three effects.

2.2 Composition

Cosmic rays consist of two populations of particles: a predominant hadronic component (99%), and a small fraction of high-energy electrons and positrons (1%). The composition of the hadronic component is dominated by protons ($\sim$ 85%), followed by helium nuclei ($\sim$ 12%) and elements with $Z > 2$ contributing with the remaining 3% of the flux. A remarkable feature of the measured CR abundances of nuclear species is the evident similarity to the abundances found in the solar system as shown in fig. 2.4 .

It is worthwhile to note that all the elements present in the solar system have been found in cosmic rays as well. The first conclusion that can be drawn is that the accelerated matter arriving on Earth comes from a region whose surrounding material has the same chemical composition of our Solar System, so it is reasonable to assume that the mechanism that originated this material is the same that originated the Sun and the planets.

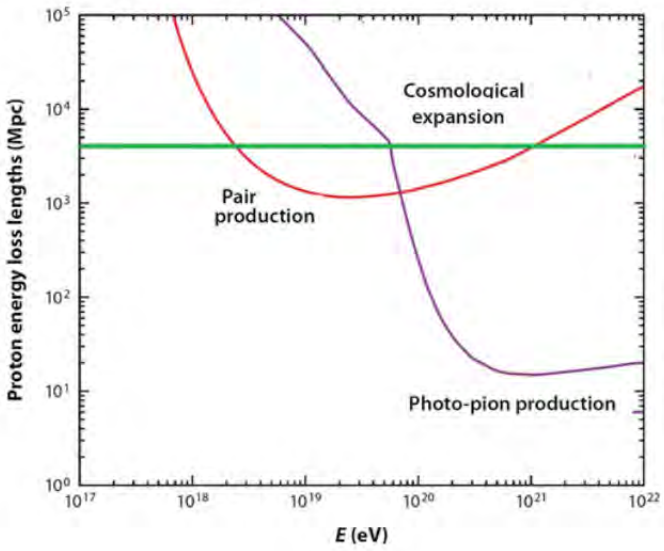

Figure 2.3: The energy loss lengths for a high-energy proton propagating through the CMB radiation field.

However, some remarkable differences between the two exist. The most relevant corresponds to the overabundance of CRs elements like lithium, beryllium, and boron ($Z = 3 - 5$), and those with $Z = 20 - 25$ with respect to the cosmic chemical composition. This difference is interpreted as due to the effect of the propagation in the Galaxy: these secondary cosmic rays originate in the fragmentation of stable and abundant primary nuclei such as carbon ($Z = 6$), oxygen ($Z = 8$), and iron ($Z = 26$) in spallation processes that occur in the interstellar medium. The ratio of secondary to primary abundances provides a measure of the material that CRs have encountered since they were accelerated and thus, since the spallation cross-section of the relevant nuclei is known at GeV energies, it can be used to infer a first-order estimate of the average time spent by a CR in the Galaxy volume i.e. the escape time τ_{esc}.

2.2.1 Escape Time

The relevant quantity for the production of secondaries is the *path lenght* ξ:

$$\xi = \rho_{ISM} \cdot x = c \cdot \rho_{ISM} \cdot \tau \quad [\text{g cm}^{-2}] \tag{2.7}$$

where ρ_{ISM} (g cm^{-3}) is the average density of the interstellar material, x (cm) is the distance traveled between the production and the exit from the Galaxy, τ represents a characteristic time of the phenomenon and c is the velocity of light (assuming relativistic particles). The value of $\xi = \xi_{esc}$ which reproduces the observed ratio ($R_{CR} \simeq 0.25$) between L (*light elements*) and M (*medium elements*) abundances corresponds to the mean amount of interstellar matter traversed by CRs before escaping from the confinement volume. As described in [11], to determine ξ_{esc} a system of differential equations for the

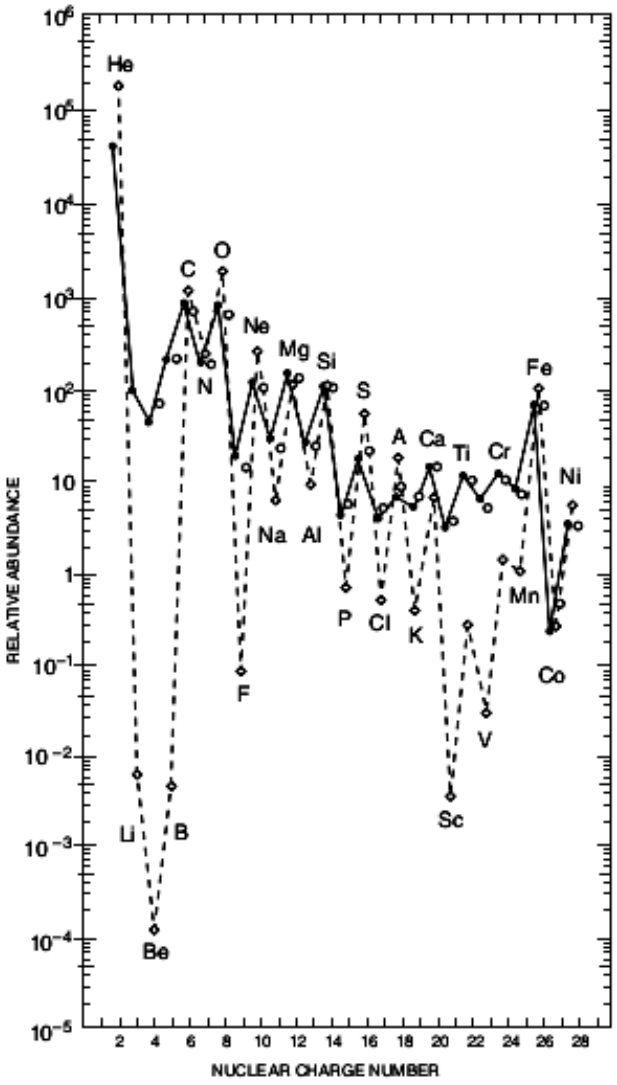

Figure 2.4: Comparison between the chemical composition of low-energy galactic CRs (solid line) and the abundances measured in the solar system (dashed line) [10]. All abundances are normalized at Silicam-100.

number of M and L nuclei as a function of ξ has to be set. The equation that describes the reduction of the number of M nuclei during their journey is:

$$\frac{d}{d\xi}N_M(\xi) = -\frac{N_M(\xi)}{\lambda_M} \tag{2.8}$$

where $\lambda_M \simeq 6.0$g cm $^{-2}$ is the mean free path for spallation processes for M nuclei.

The differential equation that describes the number of secondary L nuclei as a function of path length ξ contains a positive source term and a negative attenuation term:

$$\frac{d}{d\xi}N_L(\xi) = \frac{P_{ML}}{\lambda_M}N_M(\xi) - \frac{N_L(\xi)}{\lambda_L} \tag{2.9}$$

where $\lambda_L \simeq 8.4$g cm $^{-2}$ is the mean free path for spallation processes for L nuclei and $P_{ML} = 0.28$ is the average probability that a medium M element fragments into a lighter L element. The two functions, solutions of the differential equations, are shown in fig. 2.5 [11].

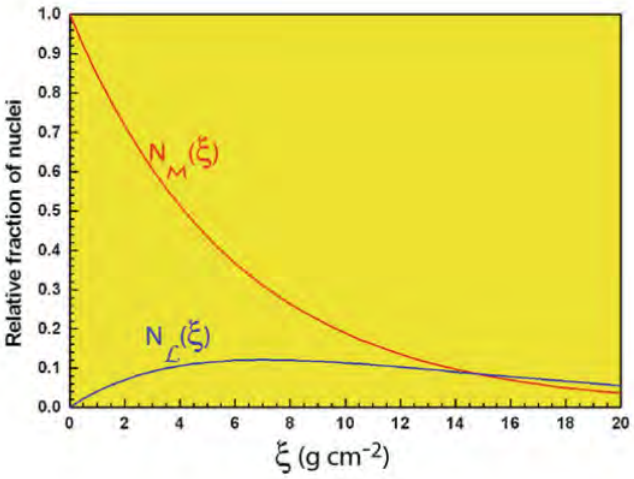

Figure 2.5: Evolution of the number of M and L nuclei as a function of the galactic path lenght ξ. Near the astrophysical accelerators ($\xi = 0$), the L nuclei are absent. As ξ increases, N_L increases as light nuclei are produced by fragmentation of M nuclei.

The value of $\xi = \xi_{esc}$ which reproduces the observed ratio R_{CR} between N_L and N_M is $\xi_{esc} = x_{esc} \cdot \rho_{ISM} = 5$ g cm^{-2}, that corresponds to a $x_{esc} = \frac{\xi_{esc}}{\rho_{ISM}} =$ 3 Mpc and so to a $\tau_{esc} = \frac{x_{esc}}{c} = 10^7$ y.

The obtained value of x_{esc} can be explained only if the propagation of cosmic rays follows a *random walk* since it is orders of magnitude larger than the thickness of the galactic disk (fig. 2.2). A rankom walk motion can be the conseguence of a tangled motion of charged particles in the galactic magnetic field. Since the gyromagnetic radius increases with energy (2.1), it is expected that the escape time τ_{esc} decreases as the particle energy increases.

2.3 Propagation

2.3.1 Galactic Cosmic Rays

Over the years, several propagation models have been proposed where cosmic rays undergo random walks in the galaxy so that long permanence times compatible with those derived from the data could be explained. One of the early models is the so-called *leaky box approximation* in which particles injected by sources Q distributed uniformly over the galactic volume (the box) have a constant probability per unit time of escape. Each cosmic ray spends a mean time τ_{esc} in the volume and traverses a mean amount of matter $\xi_{esc} = \rho\beta c\tau_{esc}$ if the particle is moving with a velocity βc through the interstellar medium (ISM) of density ρ. Gaisser [12] analyses the case of a source with injection spectrum $Q(E,t) = N_0(E)\delta(t-t_0)$, where particles are injected instantaneously at time t_0 with energy spectrum $N_0(E)$. The observed spectrum in the leaky box model will then be $N(E,t) = N_0(E)\exp(\frac{-t}{\tau_{esc}})$. Neglecting energy losses and gains, the transport equation for cosmic rays of species i can be written as:

$$\frac{N_i(E)}{\tau_{esc}(E)} = Q_i(E) - (\frac{\beta c\rho}{\lambda_i} + \frac{1}{\gamma\tau_i})N_j(E) + \frac{\beta c\rho}{m}\sum_{k>1}\sigma_{i,k}N_k(E) \tag{2.10}$$

where σ_{ik} is the spallation cross section for the production of secondaries of species i from heavier nuclei of species k, $\gamma\tau_i$ is the Lorentz dilated lifetime of the nucleus and λ is the interaction lenght of protons or nuclei in the ISM. If we assume a primary nucleus P with a very long lifetime (so that the decay term in Eq. 2.10 vanishes) that receives no contribution from spallation of heavier nuclei (so that the spallation term vanishes) we can write a solution for the flux at Earth as:

$$N_P(E) = \frac{Q_P(E)\tau_{esc}(R)}{1+\lambda_{esc}(R)/\lambda_P} \tag{2.11}$$

Since $\lambda_P >> \lambda_{esc}(\lambda_P \approx 55$ g cm$^{-2}, \lambda_{esc} = c\tau_{esc})$, the ratio at denominator can be neglected, thus:

$$N_P(E) = Q_P(E)\tau_{esc}(E). \tag{2.12}$$

Therefore the energy dependence of τ_{esc}, and thus how the propagation affects the CR energy spectrum, has to be deduced in order to derive the link between the spectrum at the source and the one on Earth. The measurement of the *secondary-to-primary ratios* of stable nuclei provides a tool for such estimation. In particular, the ratio beetween boron and carbon (B/C) can be used as reference ratio since B is entirely secondary, i.e., produced by heavier primary CR nuclei. C, N, and O are the major progenitors of B, and the production cross-section is better known than those of Be and Li. The measured B/C ratio from different experiments as a function of energy is shown in fig. 2.6.

Apart from a mild increase of the ratio starting up to $\sim$ 1GeV/nucleon due to the dependence, at low energies, of the nuclear cross-section on the relative velocity between nuclei, at higher energies, where the fragmentation nuclear cross-section is almost constant, the B/C ratio decreases. This is only a consequence of different path lengths ξ for nuclei with different energies. A

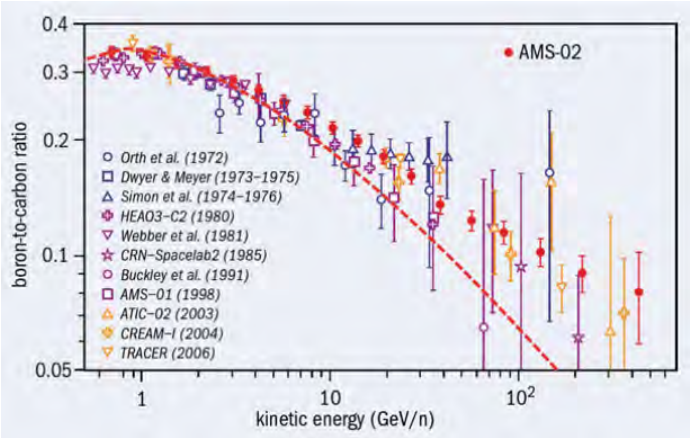

Figure 2.6: Observed boron to carbon abundance ratio, measured as a function of the kinetic energy per nucleon by different space and balloon experiments. The compilation is from the AMS-02 [13]. Previous results of other experiments are shown. The dashed line represents the result of a prediction with the leaky box model, assuming an energy-dependent escape path length $\xi_{esc} \propto E^{-0.6}$ [14]

dependence of the path length on the particle rigidity R ($R \equiv \frac{pc}{Ze} \simeq \frac{E}{Ze}$ for relativistic particles) can be empirically assumed: particles with low rigidity suffer a larger deflection during the motion in a magnetic field because, according to 2.1, the Larmor radius is $r_L = R/B$. Thus, it is reasonable to assume that the path length decreases when the rigidity R increases as:

$$\xi_{esc}(R) = \xi_0 (\frac{R}{R_0})^{-\delta} \tag{2.13}$$

where $\delta = 0.6$, $\xi_0 = 11.8$ g cm^{-2} and $R_0 = 5$GV/c are the tipical values of the parameters derived from experimental data. According to eq. 2.7, the energy dependence of τ_{esc} is given by:

$$\tau_{esc} = \tau_0 (\frac{R}{R_0})^{-0.6} = \tau_0 (\frac{E}{E_0})^{-0.6} \tag{2.14}$$

where the last equality holds for high energy particles.

Now it is possible to go back to eq. 2.12. By replacing $\tau_{esc}(E)$ with the result obtained in 2.16 we get:

$$\Phi(E) \propto Q_P(E) \cdot E^{-\delta} \tag{2.15}$$

where $\Phi(E) \propto E^{-\alpha}$ represents the primary spectrum of CRs observed on Earth and $\alpha = 2.7$ below the knee, thus:

$$Q_P(E) = \frac{\Phi(E)}{E^{-\delta}} \propto E^{-\alpha} \cdot E^{\delta} = E^{-2.1} \tag{2.16}$$

The spectral index at the source 2.1 is in good agreement with the expected spectrum for acceleration in astrophysical shocks.

2.3.2 Extragalactic Cosmic Rays

Cosmic rays with energies above 10^{18} eV cannot be contained by the magnetic field of the galaxy and can propagate over intergalactic distances. If their energy is large enough to reach in the center-of-mass system the resonant production of the Δ^+, they experience energy losses due to the GZK effect, which reduces their mean free path to a few tens of Mpc. Since in intergalactic space the magnetic field intensities are expected to be much lower than in the Galaxy ($B < 10^{-9}$G), the trajectories of ultra-high-energy cosmic rays (UHECRs) are less deflected and they can be used to search for cosmic rays sources as they point back to their origin. Once entered the Galaxy UHECRs feel little influence from magnetic fields. The deflection angle of a particle of energy E moving in a direction perpendicular to a uniform magnetic field B after travelling the distance d is :

$$\Theta \sim \frac{d}{r_L} \sim 0.5^\circ Z(\frac{E}{10^{10}\text{eV}})^{-1}(\frac{d}{\text{kpc}})(\frac{B}{\mu G}) \tag{2.17}$$

Therefore a small deflection of $\sim 1^\circ - 5^\circ$ is expected for proton of energy 5×10^{19}eV. This result motivates the search for extragalactic sources of UHECRs since galactic sources would produce a clear anisotropy on Earth measurements, that is not observed.

2.4 Acceleration Mechanism

The identification of a process that could accelerate particles up to the extreme energies observed in the cosmic ray flux was an important theoretical challenge in the past century. The acceleration model has to explain the following features observed in experimental data:

- energy spectrum of the form $\Phi(E) \propto E^{-\alpha}$, indicating "non-thermal" acceleration processes: continuum emission not originated by blackbody radiation or thermal bremsstrahlung;
- the measured exponent is $\alpha \sim 2.7$ for protons and nuclei and $\alpha \sim 3$ for electrons up to the knee. Once corrected for propagation in the Galaxy, e spectral index $\alpha \sim 2$ at the source is expected;
- the observed chemical abundances of CRs below the knee are similar to the abundances of the elements as found in our Solar System;
- the observed exponent α becomes ~ 3.1 above the knee while the energy spectrum flattens again to form the ankle at $\sim 5 \times10^{18}$ eV.

In 1949, Enrico Fermi proposed a mechanism [15], known as the "Second Order Fermi Mechanism", for particles to gain energy through their interaction with magnetized clouds in interstellar space. Those particles involved in head-on collisions will gain energy and those involved in tail-end collisions will lose energy. On average, however, head-on collisions are more probable. In this way, particles gain energy over many collisions. Magnetized clouds are considered "magnetic mirrors" and are assumed to move randomly with typical velocity V. Let us derive the final energy gain of the accelerated particle in the case in

which the collision between the particle and the mirror takes place such that the angle between the initial direction of the particle and the normal to the surface of the mirror is Θ (Fig. 2.7) [16].

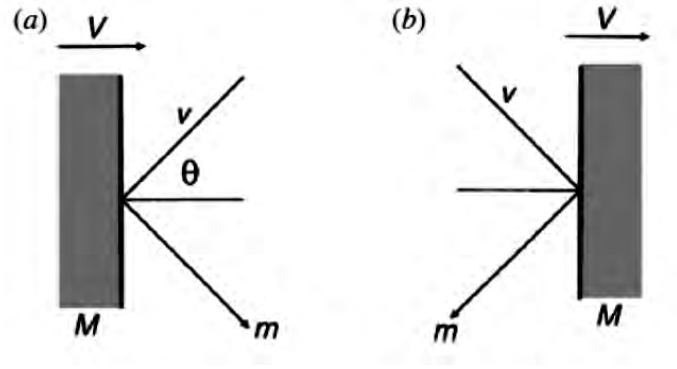

Figure 2.7: Illustration of a collision between a particle of mass m and a cloud of mass M: (a) a head-on collision; (b) a tail-end collision.

The mirror is considered infinitely massive so that its velocity is unchanged in the collision. Therefore, the centre of momentum frame of reference is that of the cloud moving at velocity V . The energy of the particle in this frame is

$$E' = \gamma_V(E + Vpcos\theta) \text{ , where } \gamma_V = \left(1 - \frac{V^2}{c^2}\right)^{-1/2} \tag{2.18}$$

The x component of the relativistic three-momentum in the centre of momentum frame is

$$p'_x = p'cos\theta' = \gamma_V(pcos\theta + \frac{VE}{c^2}) \tag{2.19}$$

In the collision, the particle's energy is conserved, $E'_{before} = E'_{after}$, and its momentum in the x direction is reversed, $p'_x \rightarrow -p'_x$. Therefore, transforming back to the observer's frame, we find

$$E'' = \gamma_V(E' + Vp'_x) \tag{2.20}$$

Substituting equations 2.18 and 2.19 into eq. 2.20 and recalling that $p_x/E = vcos\theta/c^2$, the change in energy of the particle is

$$E'' = \gamma_V^2 E\Big[1 + \frac{2Vv\cos\theta}{c^2} + \left(\frac{V}{c}\right)^2\Big] \tag{2.21}$$

Expanding to second order in V/c, we find

$$E'' - E = \Delta E = \frac{2Vv\cos\theta}{c^2} + \left(\frac{V}{c}\right)^2 \tag{2.22}$$

We now average over the angle θ. There is a slightly greater probability of head-on encounters as opposed to tail-end collisions: the probabilities are proportional to the relative velocities of approach of the particle and the cloud, namely, $v + Vcos\theta$ for (a) and $v - Vcos\theta$ for (b). Let us consider the case of a relativistic particle with $v \approx c$, then the probabilities are proportional to

$1+(V/c)cos\theta$ where $0 < \theta < \pi$. Recalling that the probability of the angle lying in the angular range θ to $\theta + d\theta$ is proportional to $sin\theta d\theta$, on averaging over all angles in the range 0 to π , the first term in 2.22 in the limit $v \to c$ becomes

$$\Big\langle \frac{2Vcos\theta}{c} \Big\rangle = \Big(\frac{2V}{c}\Big) \frac{\int_{-1}^{1} x[1+(V/c)x]\,dx}{\int_{-1}^{1}[1+(V/c)x]\,dx} = \frac{2}{3}\Big(\frac{2V}{c}\Big)^2 \tag{2.23}$$

where $x = cos\theta$. Thus, in the relativistic limit, the average energy gain per collision is

$$\Big\langle \frac{\Delta E}{E} \Big\rangle = \frac{8}{3}\Big(\frac{V}{c}\Big)^2 \tag{2.24}$$

Since the energy gain is quadratic in the velocity of the particle, this process is known as second order Fermi acceleration. Due to the low cloud velocities ($V << v \sim c$), the energy gain per collision is very small ($\sim V^2$) which implies that this process requires very long times to accelerate particles.

2.4.1 First Order Fermi Mechanism

A more efficient version of Fermi Acceleration was proposed independently by a number of workers in the late 1970's. In this model, particles are accelerated by a strong shock propagating through interstellar space. The following gives a schematic of the process as described in [16]. The model involves a strong shock propagating through a diffuse medium (diffusive shock acceleration), for example, the shock waves which propagate through the interstellar medium ahead of the supersonic shells of supernova remnants. The following features in the acceleration site are assumed:

- a flux of high energy particles is present both in front of and behind the shock front;
- the particles propagate at speeds close to that of light and so the velocity of the shock is very much less than those of the high energy particles;
- the thickness of the shock is normally very much smaller than the gyro-radius of the high energy particle and so the particles scarcely notice the shock;

Since the particles experience scatterings by streaming instabilities or turbulent motions on either side of the shock wave, when the they pass though the shock in either direction their velocity distribution rapidly becomes isotropic in the frame of reference of the moving fluid on either side of the shock. Fig. 2.8 illustrates the situation: a strong shock wave travels at a highly supersonic velocity $U >> c_s$, where c_s is the sound speed in the ambient medium (Fig. 2.8 a). In the frame of reference in which the shock front is at rest, the upstream gas flows into the shock front at velocity $v_1 = U$ and leaves the shock with a downstream velocity $v_2 = v_1/4$ (see [16]) (Fig. 2.8 b). Now consider high energy particles down-stream of the shock. The shock front moves at velocity U but the gas up-stream (i.e. behind) the shock advances at a speed $(3/4)U$ relative to the material down-stream. When a particle crosses the shock front from right to left, an elastic collision occurs and the particle gains energy. The

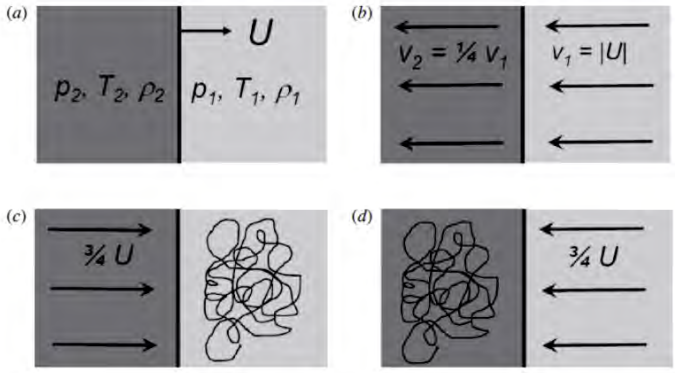

Figure 2.8: The dynamics of high energy particles in the vicinity of a strong shock wave.

velocity distribution of particles entered in the region behind the shock front will become isotropic with respect to that flow. A symmetric situation occurs for a particle diffusing from up-stream the shock, moving towards the ahead region in front of the shock (Fig. 2.8d). The distribution of the particle velocities is isotropic behind the shock. When crossing the shock front, a particle encounters gas moving towards the shock front, again with speed $(3/4)U$. It receives the same increase in energy on crossing the shock front from down-stream to up-stream as it did in traveling from up-stream to down-stream. The fact that in every passage through the shock front the particle receives an increase of energy is the clever aspect of the first-order Fermi acceleration mechanism. Every time the particle crosses the shock front it receives an increase of energy – there are never crossings in which the particles lose energy – and the increment in energy is the same going in both directions. Thus, unlike the original Fermi mechanism in which there are both head-on and following collisions, in the case of the shock front, the collisions are always head-on and energy is transferred to the particles. Analogous calculations to those used for the second order Fermi mechanism leads to the energy gain at each passage:

$$\left\langle \frac{\Delta E}{E} \right\rangle = \frac{4}{3}\left(\frac{V}{c}\right) \tag{2.25}$$

2.4.2 Power-law Energy Spectrum

The success of the Fermi models is due to the fact that it succedeed in deriving a power-law energy spectrum. We let $E = \beta E_0$ be the average energy of the particle after one collision and P be the probability that the particle remains within the accelerating region after one collision. After k collisions, there are $N = N_0 P^k$ particles with energies $E = E_0 \beta^k$. If we eliminate k between these quantities:

$$\frac{ln(N/N_0)}{ln(E/E_0)} = \frac{lnP}{ln\beta} \tag{2.26}$$

and then

$$\frac{N}{N_0} = (\frac{E}{E_0})^{lnP/ln\beta} \tag{2.27}$$

Therefore:

$$N(E)dE = \text{constant} \times E^{-1+(lnP/ln\beta)}dE \tag{2.28}$$

This result is valid both for first and second order Fermi mechanisms. However, in the framework of the diffusive shock acceleration model, a value for the spectral index equal to 2 can be obtained. Following the argument due to Bell (1978) and reported also in [16], $P = 1 - U/c$, hence:

$$lnP = ln(1 - \frac{U}{c}) \simeq -\frac{U}{c} \;\; ; ln\beta = ln(1 + \frac{U}{c}) \simeq +\frac{U}{c} \tag{2.29}$$

Thus, the exponent of the differential energy spectrum in 2.28 is:

$$\alpha_s = -1 - 1 = -2 \tag{2.30}$$

2.5 Origin

A galactic or extragalactic source can be considerated a good candidate as a CRs accelerator if it both provides powerful shocks and strong magnetic fields that can confine the particles for such a time that it can be accelerated up to the highest observed enegies. Once the Larmor radius of a particle is comparable to the size of the acceleration region, the probability of escape from the region increases significantly. The "Hillas criterion" expresses the relation between maximum achievable energy E_{max} , size R, and magnetic field strength B [17], and can be expressed as

$$E^{max} \simeq Z\beta \cdot \left(\frac{B}{\mu\text{G}}\right) \cdot \left(\frac{R}{\text{kpc}}\right) \;\; \text{EeV} \tag{2.31}$$

where Z is the cosmic ray charge, β is the velocity parameter of the shock wave. This relation is represented graphically in Fig. 2.9, where several types of astrophysical objects are shown according to their potential to accelerate cosmic rays.

2.5.1 Galactic Cosmic Rays

Core collapse supernovae are suitable candidates for the acceleration of CRs with energy below 10^{15} for the following reasons:

- Equilibrium (firstly hypothesized by Baade and Zwicky in 1934 [18]) between the loss of CRs due to their escape out of the galactic volume and the energy provided by supernova shock waves. The energy density of Galactic cosmic rays in our galaxy is $\sim$ 1 eV/cm^3. Assuming a typical cosmic-ray escape time of 6×10^6 years, the power needed to fill the Galactic disk (volume $\sim 4 \times 10^{66}$ cm^3) with cosmic rays is approximately $P_{CR} = 5 \times 10^{40}$ erg/s. Type II (core collapse) supernovae can eject several solar masses of material with bulk velocities of around $5 \times 10^7 m/s$. This corresponds to a total kinetic energy of around 10^{51} ergs, meaning

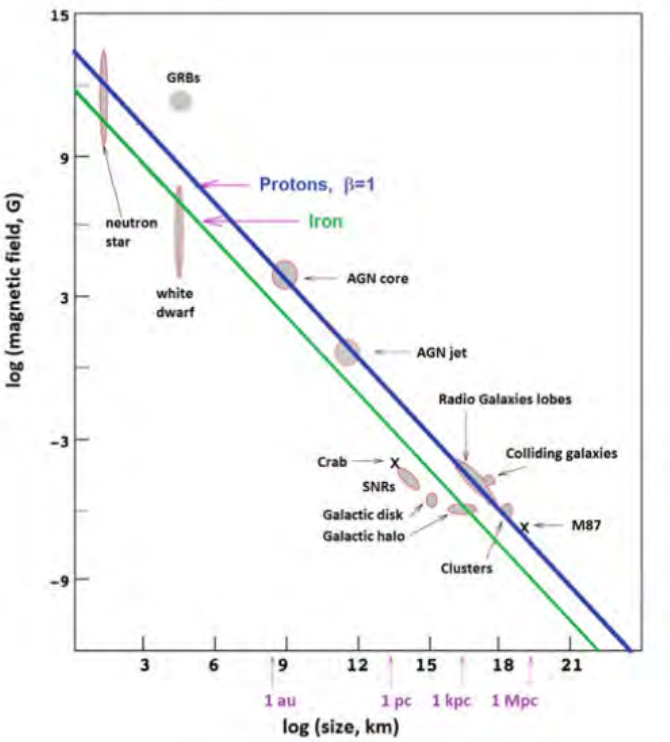

Figure 2.9: Example of the diagram first produced by Hillas. Acceleration of cosmic rays up to a given energy requires magnetic fields and sizes above the respective line. The blue (green) line corresponds to the condition for B, L to accelerate protons (iron) at 10^{20} eV.

that the power delivered by all Type II supernova is $P_{SN} \sim 3 \times 10^{42}$ erg/s, given a supernova rate of about three explosions per century in the galaxy. By requiring that $P_{CR} = P_{SN}$ we find that a mechanism able to trasfer energy from the kinetic energy of the shock waves to the particles with an efficiency of a few percent is needed.

- According to eq. 2.25, the particle gain in the first order Fermi mechanism is proportional to

$$\eta = 4/3(U/c) \tag{2.32}$$

where η can be considered the efficiency of energy trasfer from the shock wave to the particle. The everage energy emitted as kinetic energy K by a 10 $M_\odot$ supernova is ~ 1 % of the total binding energy. The velocity of the ejected mass is of the order of

$$U \simeq \sqrt{\frac{2K}{M}} \simeq 5 \times 10^8 \text{cm /s} \quad \longrightarrow \frac{U}{c} \simeq 2 \times 10^{-2} \tag{2.33}$$

Therefore η corresponds to the needed efficiency required to explain the CRS acceleration in supernovae explosion.

- The chemical composition of cosmic rays is very similar to the abundances of the elements in the Solar System which, in turn, is similar to that produced by core-collapse supernovae.

- It is possible to express the maximum energy that a charged particle can reach in the acceleration process due to the diffusive shock mechanism from a supernova explosion [11]. The rate of energy increase is given by the ratio between 2.25 and the characteristic period T_{cycle} of the process, i.e. the time between two successive scattering processes:

$$\frac{dE}{dt} \simeq \frac{\eta E}{T_{cycle}} \tag{2.34}$$

  where η has been defined in 2.32. T_{cycle} can be written as $T_{cycle} = \frac{\lambda_{cycle}}{U}$, where λ_{cycle} is the typical extentension of the confinement region, the Larmor radius, and U is the velocity of the shock front. Thus

$$\frac{dE}{dt} \simeq \frac{\eta E}{T_{cycle}} = \eta E \frac{U}{\lambda_{cycle}} = \eta E \frac{ZeBU}{E} \tag{2.35}$$

The maximum energy can be expressed as

$$E^{max} \simeq \frac{dE}{dt} \times T_{SN} = \eta Z e B R_{SN} \tag{2.36}$$

Inserting typical values we obtain $E^{max} \simeq 300 \cdot Z$ TeV. Thus this model explains the spectrum of cosmic-ray protons up to few hundreds of TeV which corresponds to the energy region where the knee begins: the transition between galactic and extragalactic CRs.

2.5.2 Extragalactic Cosmic Rays

According to the Hillas criterion (eq. 2.31), acceleration sources for the most energetic CRs have to provide a compensation between magnetic field and size so that the gratest energies can be reached. The following is a list of possible sources which also emit high-energy photons up to multi-TeV, emission naturally connected to the acceleration of electrons and/or protons in astrophysical sources. For each source typical values for B and L and the maximum achieveble energy for proton is also reported.

- AGN ($L \sim 0.1$ pc, $B \sim 1\mu$G , $E^{max} \sim 10^{20}$eV) are galactic nuclei, which presumably host a black hole with a typical mass of $M = 10^7 - 10^8 M_\odot$. They are characterized by jets with transverse dimensions of the order of a fraction of a parsec and magnetic fields necessary to explain the synchrotron radiation from such objects.

- Gamma Ray Burst (GRBs) ($L \sim 10^{-6}$ pc, $B \sim 10^6$G , $E^{max} \sim 10^{20}$eV) are the most energetic transient eruptions observed in the Universe whose emission mechanism is explained with the Fireball model. In this model, photon-proton interactions in the GRB fireball should produce TeV neutrinos detectable by neutrino telescopes. A recent analysis of IceCube data shows no neutrino emission associated with GRBs, which heavily

constraints neutrino emission models from GRBs and also their contribution to the cosmic ray flux near GZK energies [19].

- Magnetars ($L \sim 20$ km, $B \sim 10^{15}\mu$G , $E^{max} \sim 10^{20}$eV) are neutron stars with stronger magnetic fields and slower rotation periods. As GRBs, Magnetars are transient sources, thus they cannot be associated with the detection of UHECRs.

2.6 Cosmic-ray detectors

The detection of charged cosmic rays may be done at top of the Earth atmosphere in balloon or satellite based experiments whenever the fluxes are high enough (typically below tens or hundreds of GeV). They operate at an altitude above 15 km where they can detect the interaction of the primary particle inside the detector, but they are limited in detection area and so also limited in the energy range they can measure. Otherwise above this energy the observations are performed by exploiting the cascades induced in atmosphere by the interactions of cosmic rays.

In the following, two satellite experiments are presented. Their detection principle is aimed at (i) the identification of the particle, (ii) the measure of its electric charge and (iii) the measure of its energy and momentum. This is usually obtained by means of a magnetic field, a tracking system and a calorimeter.

- The PAMELA experiment launched in June 2006 measured charged particle and antiparticles out of the Earth atmosphere during a long (six years) time period. A good charge separation between electron and positrons was ensured by a permanent magnet of 0.43 T and a microstrip silicon tracking system up to energies of the order of the hundred of GeV measured by a silicon/tungsten electromagnetic calorimeter complemented by a neutron counter to enhance the electromagnetic/hadronic discrimination power. The trigger was provided by a system of plastic scintillators which were also used to measure the time-of-flight and an estimation of the specific ionization energy loss (dE/dX) (fig.2.10);

- The Alpha Magnetic Spectrometer (AMS-02) was installed in May 2011 on the International Space Station. Its layout is similar to PAMELA but with a much larger acceptance and a more complete set of sophisticated and higher performing detectors. Apart from the permanent magnet and the precision silicon tracker it consists of a transition radiation detector, time-of-flight and anti-coincidence counters, a ring imaging Cherenkov detector and an electromagnetic calorimeter (fig. 2.11).

2.6.1 Extensive air showers

High-energy hadrons, photons and electrons interact in the high atmosphere. The process characterizing hadronic and electromagnetic showers is similar (fig. 2.12). For photons and electrons above a few hundred MeV, the cascade process is dominated by the pair production and the bremsstrahlung mechanisms: an energetic photon scatters on an atmospheric nucleus and produces a pair, which

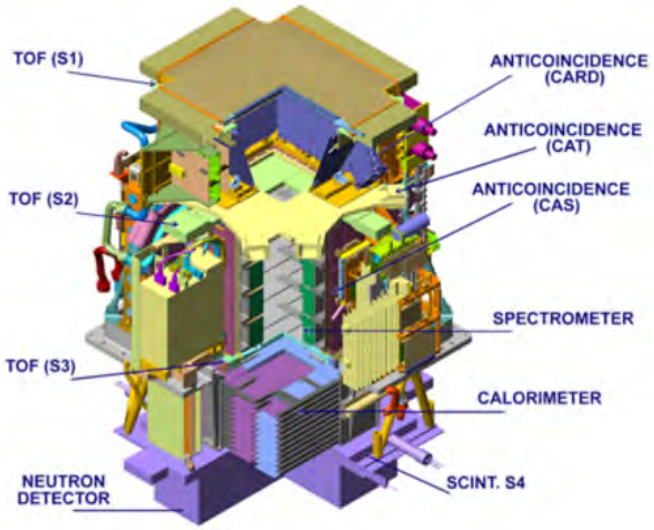

Figure 2.10: The PAMELA detector layout. Credit: PAMELA Collaboration.

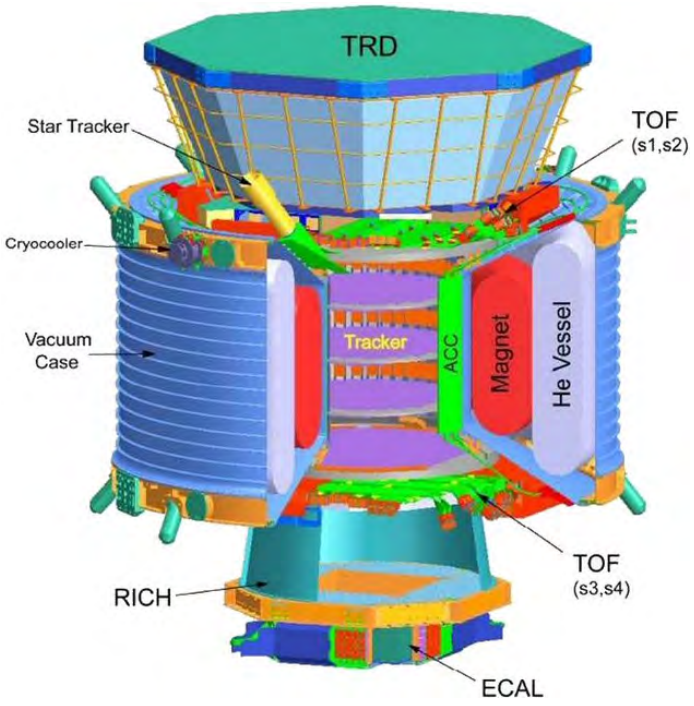

Figure 2.11: The AMS-02 detector layout. Credit: AMS Collaboration.

emits secondary photons via bremsstrahlung; such photons produce in turn a

e^+ e^- pair, and so on, giving rise to a shower of charged particles and photons.

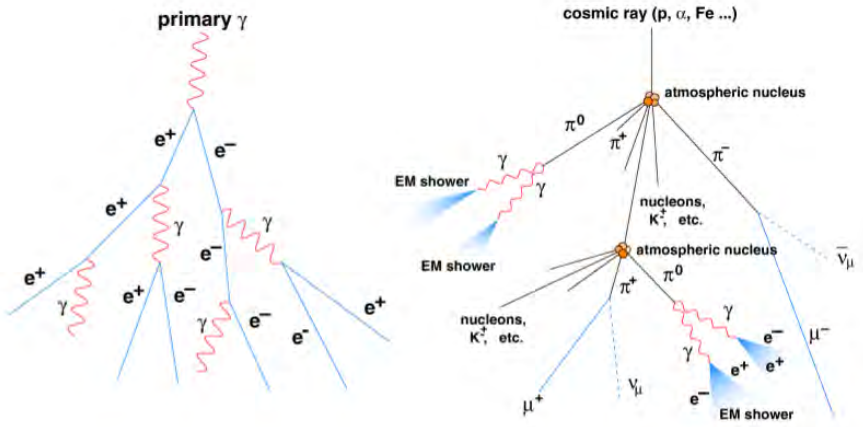

Figure 2.12: Schematic representation of two atmospheric showers initiated by a photon (left) and by a proton (right).

The longitudinal development of typical photon-induced extensive air showers is shown in Figure 2.13 for different values of the primary energies.

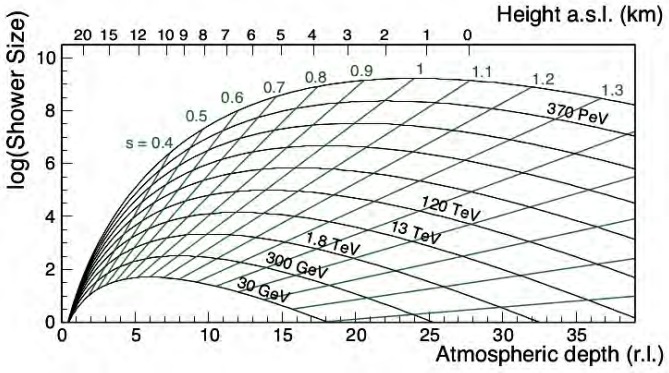

Figure 2.13: Longitudinal shower development from a photon-initiated cascade. The parameter s describes the shower age.

The maximum shower size occurs approximately at $ln(E/\epsilon_0)$ radiation lengths, where the radiation length for air is about 37 g/cm^2 (approximately 300 meters at sea level and NTP). The critical energy ϵ_0 , the energy below which the ionization energy loss starts to dominate the energy loss by bremsstrahlung, is about 80 MeV in air. The hadronic interaction length in air is about 61 g/cm^2 for protons (500 meters for air at NTP), being shorter for heavier nuclei. The dependence of the cross section on the mass number A is approximately $A^{2/3}$. The transverse profile of hadronic showers is in general wider than for electromagnetic showers, and fluctuations are larger. Particles release energy in the atmosphere, which acts like a calorimeter, through different mechanisms, which give rise to a measurable signal, mainly fluorescence and Cherenkov radiation.

Extensive air showers (EAS) produced by high energy cosmic rays are detected using three different techniques:

- **Surface Detectors:** the measurement of a fraction of the EAS particles arriving at the Earth surface through an array of surface detectors (SD);
- **Fluorescence Detectors:** the measurement in moonless nights of the fluorescence light emitted mainly by the excitation of the atmosphere nitrogen molecules by the shower low energetic electrons through an array of ultra-violet fluorescence detectors (FD) placed on the Earth surface or even in satellites;
- **Imaging Atmosphere Cherenkov Telescopes:** the measurement of the Cherenkov light emitted by the ultra-relativistic air shower particles in a narrow cone around the shower axis, through dedicated telescopes as the Imaging Atmosphere Cherenkov Telescopes (IACTs).

Surface Detectors

Surface detectors measure at specific space locations the time of arrival of individual particles. The most widely used surface detectors are scintillation counters and water Cherenkov counters. The arrival direction of an air shower is determined from the arrival time at the different surface detectors of the shower front, which, in a first approximation, can be described by a thin disk that propagates with the speed of light. The impact point of the air shower axis at the Earth surface (the air shower core) is defined as the point of maximum particle density and is determined from the measured densities at the different surface detectors. The measured densities are usually parameterized by empirical or phenomenological inspired formulae, which depend also on the shower age (the level of development of the shower in the moment when it arrive at the Earth surface). Such functions allow for a better determination of the shower core and for the extrapolation of the particle density to a reference distance of the core which is then used as an estimator of the shower size and thus of the shower energy. The exact function as well as the reference distance depends on the particular experiment setup.

Fluorescence Detectors

The fluorescence telescopes record the intensity and arrival time of the light emitted in the atmosphere in specific solid angle regions and thus are able to reconstruct the shower axis geometry and the shower longitudinal profile. In Figure 2.14 the image of a shower in the focal plane of one of the Pierre Auger fluorescence telescope (see later) is shown. The third dimension, time, is represented in a color code. The geometry of the shower is then reconstructed in two steps: first the shower detector plane (SDP) is found by minimizing the direction of the SDP normal to the mean directions of the triggered pixels, and then the shower axis parameters within the SDP are found from the measured arrival time of the light in each pixel assuming that the shower develops along a line at the speed of light. The simultaneous observation of the shower by two (stereo) or more fluorescence detectors or by a surface detector array (hybrid detection) provides further geometric constrains which improve considerably the resolution of the shower geometric reconstruction.

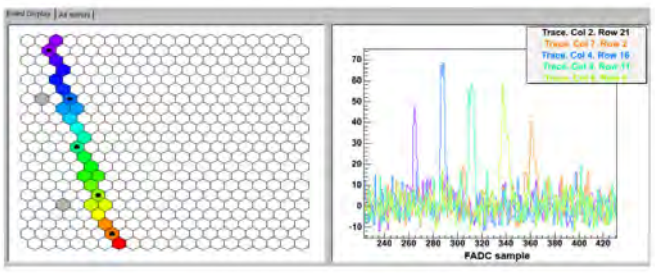

Figure 2.14: Display of one shower in the focal plane of one of the Pierre Auger fluorescence telescopes. Left: Pattern of the pixels with signal; right: response (signal versus time, with a time bin of 100 ns) of the selected pixels (marked with a black dot in the left panel). The development of the shower in the atmosphere can be qualitatively pictured. From www.auger.org.

Imaging Atmosphere Cherenkov Telescopes

Many secondary particles in the EAS are superluminal, and thus they give rise to the emission of Cherenkov light that can be used for the detection. The properties of the Cherenkov emission will be discussed in Section 4.1.1. At 8 km, the value of the Cherenkov angle Θ_C in air for $\beta = 1$ is about 1°. Half of the emission occurs within 20 m of the shower axis (about 70 m for a proton shower). The observational technique used by the IACTs is to project the Cherenkov light collected in a large optical reflecting surface onto a camera which is basicaly an array of photomultipliers, with typical quantum efficiency of about 30%, in the focal plane of the reflector (see Figure 2.15). The camera has a typical diameter of about 1 m, and covers a FoV of $5° \times 5°$. The signal collected by the camera is analogically transmitted to trigger systems, similar to the ones used in high-energy physics. The events which pass the trigger levels are sent to the data acquisition system, which typically operates at a frequency of a few hundreds Hz. The typical resolution on the arrival time of a signal on a photomultiplier is better than 1 ns. The shower has a duration of a few ns (about 2 to 3) at ground; this duration can be maintained by an isochronous (parabolic) reflector.

In the following, different experiments for the detection of UHECRs are described.

- The Pierre Auger Observatory in Malargue, Argentina, is the largest cosmic ray detector ever built. It covers a surface of about 3000 square kilometers with 1600 surface detector stations (Cherenkov water tanks) arranged in a triangular grid of 1.5 km side complemented by 24 fluorescence telescopes, grouped into four locations to cover the atmosphere above the detector area (Figure 2.16). Each water tank is a cylinder of 10 m^2 base by 1.5 m height filled with 12 tons of water (Figure 4.44). The inner walls of the tank are covered with a high reflectivity material. The Cherenkov light, produced by the charged particles crossing the tank, is collected by three PMT placed on the top of the tank. Each tank is autonomous being the time given by a GPS unit and the power provided by a solar panel; it communicates via radio with the central data acquisition system. Each fluorescence detector is a Schmidt telescope with a field of

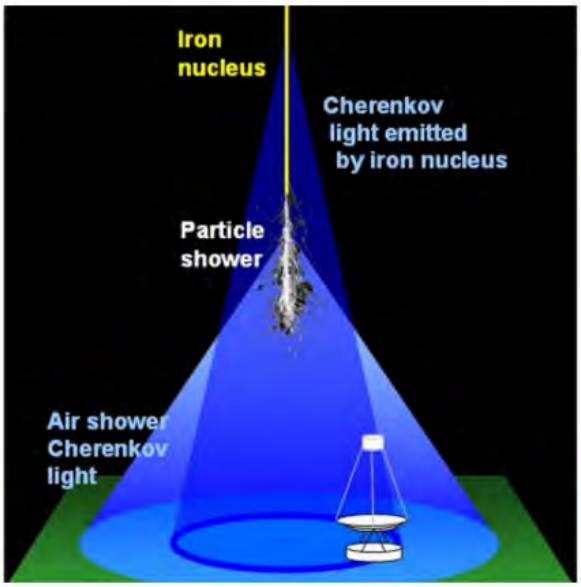

Figure 2.15: The observational technique adopted by Cherenkov telescopes.

view of 30° in azimuth and 29° in elevation (2.17). The light enters the telescope through an ultra-violet filter installed over the telescope circular diaphragm cross and is collected in a 3.5 m diameter spherical mirror which focus it in a 440 PMT camera.

- The largest cosmic ray detector in the northern hemisphere is the Telescope Array (TA) in Utah, USA. Similar to Auger, it is also an hybrid detector composed by a surface array of 507 scintillator detectors, each 3 m in size, located on a 1.2 km square grid, plus three fluorescence stations each one with a dozen of telescopes each instrumented with a 256 PMT camera covering 3 to 33 degrees in elevation. The total surface covered is about 800 square kilometers.

- HAWC is a very high-energy gamma-ray observatory located in Mexico at an altitude of 4100 m. It consists of 300 steel tanks of 7.3 m diameter and 4.5 m deep, covering an instrumented area of about 22 000 m^2 . Each tank is filled with purified water and contains three PMT of 20 cm diameter, which observe the Cherenkov light emitted in water by superluminal particles in atmospheric air showers. Photons traveling through the water typically undergo Compton scattering or produce an electron-positron pair, also resulting in Cherenkov light emission. This is an advantage of the water Cherenkov technique, as photons constitute a large fraction of the electromagnetic component of an air shower at ground.

- There are three large operating IACTs: H.E.S.S., MAGIC and VERITAS,

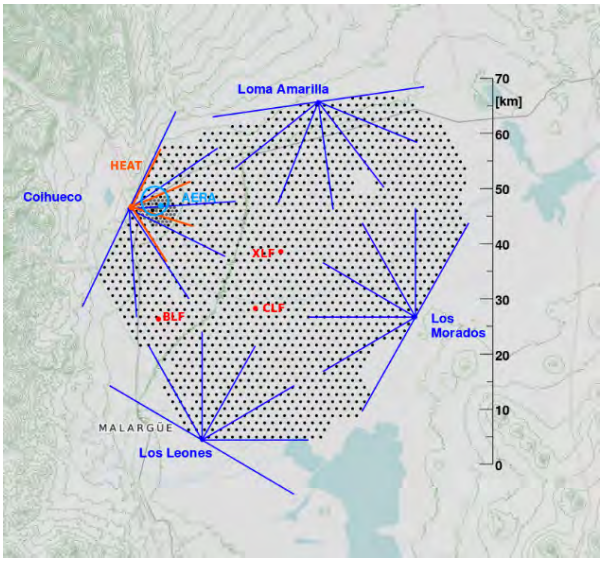

Figure 2.16: The Pierre Auger Observatory near Malargue, Argentina. The radial lines point to the fluorescence detectors (FD, $4 \times 6 = 24$). The black dots are the 1600 ground stations (SD).

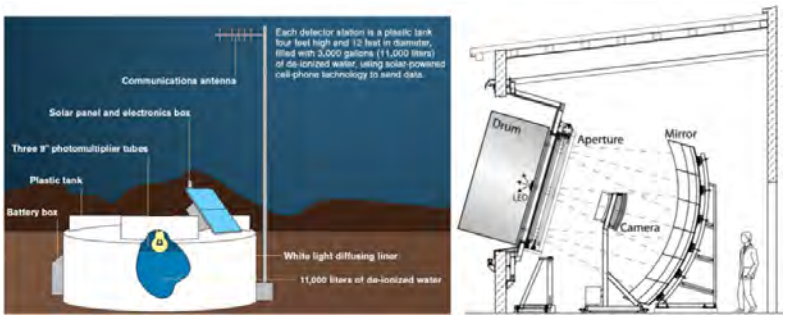

Figure 2.17: Sketch of one of the Pierre Auger surface detectors (left); a fluorescence telescope (right). From www.auger.org.

the first located in the southern hemisphere, and the last two in the northern hemisphere. The H.E.S.S. observatory in Namibia is composed by four telescopes with a diameter of 12 m each, working since early 2003. A fifth large telescope, a surface of about 600 m^2 , is located in the centre; it has been inaugurated in 2012. The MAGIC observatory in the Canary Island of La Palma is a twin telescope system; each parabola has a diameter of 17 m and a reflecting surface of 236 m^2 , and it is the largest single-dish Cherenkov telescope in operation. VERITAS is constituted by an array of four telescopes with a diameter of 12 m and is located near Tucson, Arizona. It is operational since April 2007.

2.6.2 γ-rays and neutrinos

In the surroundings of the CRs acceleration sites, high-energy photons can be produced by the interaction of high-energy charged particles (for example electrons, protons, ions accelerated by the shock waves of remnants of gravitational collapses) with nuclear targets such as molecular clouds or radiation fields (magnetic fields, photon fields). Alternatively, they could be the produced via the decay of heavy particles. Here comes the distinction between purely leptonic mechanisms of production and models in which photons are secondary products of hadronic interactions.

- Leptonic Model: the basic interpretation for the production of high-energy photons in the astrophysical leptonic model is the so-called Self-Synchrotron Compton (SSC) mechanism. Synchrotron emission from electrons moving in a magnetic field generates photons with an energy spectrum peaked in a region ranging from the infrared to X-rays. Such photons in turn constitute a target for their own parent electron population. The process in which low-energy photons gain energy by collisions with high-energy electrons is the inverse Compton (IC) scattering. This mechanism has the effect of increasing the photon energy, and is important in regions where accelerated electrons coexist with a high energy density of soft-photons.

- Hadronic Model: a direct signature of the presence in astrophysical environments of accelerated protons is provided by the presence of neutrinos and of $\gamma-$rays. They are mainly generated in the decay of charged and neutral pions, respectively; these mesons can be produced in two ways: proton-proton collisions via $p + p \rightarrow \pi^{\pm}, \pi^0, K^{\pm}, K^0, p, n$ with the presence of higher mass mesons and baryons, or high-energy protons interacting with low-energy photons in the surroundings of sources. The process (also called photoproduction) is similar to that discussed in Sect 2.1 for CR protons interacting on CMB photons. Under these conditions, the mechanisms that produce CRs produce also neutrinos and high-energy photons.

Fig. 2.18 shows the expected photons spectra according to different acceleration processes: leptonic models give rise to the Synchrotron and IC spectra while the hadronic models produce the so called beam-dump spectrum due to the π^0 decay.

$\gamma-$ray and neutrinos flux measurements allow to descriminate between the two models. The measurements of both $\gamma-$rays and neutrinos can give crucial information on primary CRs.

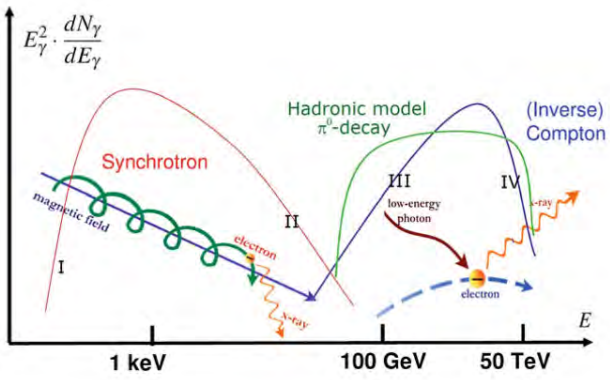

Figure 2.18: Spectral energy distribution of photons produced in leptonic/hadronic models. Synchrotron radiation is caused by relativistic electrons accelerated in a magnetic field. Photons from synchrotron emission represent also the target for inverse Compton scattering of the parent electrons. When hadrons interact with matter or ambient photons, a distribution of $\gamma-$rays from π^0 decays as indicated by the green curve could be obtained. Superimposition of $\gamma-$rays from both leptonic and hadronic mechanisms is assumed in case of mixed models. [11]

Chapter 3

Anisotropy

The arrival direction of charged cosmic rays is basically isotropic, when the low-energy particles affected by the Sun are neglected. This fact can be explained as the effect of the galactic magnetic field which efficiently isotropizes the trajectories of cosmic rays before their arrival at Earth. However, experiments like Milagro, IceCube, ARGO and the Tibet air shower array have observed small anisotropies (at the level of about one part per mille) in cosmic rays with energies above a few TeV.

3.1 Galactic Magnetic Field

Precise information on the galactic magnetic field comes from radio astronomy: radio telescopes can measure the Faraday rotation angle and the extent of dispersion of the radiation emitted by pulsars [16] . The Faraday rotation effect is based on the fact that the plane of polarization of linearly polarized electromagnetic waves rotates when they propagate in the presence of a magnetic field B in a medium with electron density N_e [m^{-3}]. The rotation depends on the square of the wavelength λ, and on the parallel component of the magnetic field B along the line of sight to the source:

$$RM = 8.12 \times 10^3 \int_0^L N_e B_{||}\, dl \quad , \quad RM = \frac{\theta}{\lambda^2} \tag{3.1}$$

where

- θ [rad] is the angle between the direction of wave propagation and the magnetic field direction;
- λ [m] is the wavelength;
- L [pc] is the distance traveled by the radiation;
- $B_{||}$ [T] is the component of B parallel to the line of sight;
- N_e [m^{-3}] is the electron density.

Therefore, by measuring the variation of the angle of polarization θ as a function of the wavelength λ from radio pulsars characherized by linearly polarized radio emission, the *rotation measure* RM can be estimated and gives

information about the integral of $N_e B_{||}$ along the line of sight. Observations of the Faraday rotation can then be combined with measurements of pulsars dispersion measures defined as the integral along the line of sight of the electron density N_e. This quantity can be estimated by measuring the arrival time of the pulse T_a as a function of frequency since the following relation holds:

$$T_a = 4.15 \times 10^9 \frac{1}{\nu^2} \int_0^L N_e \, dl \quad \text{s} \tag{3.2}$$

where

- ν [Hz] is the frequency;
- L [pc] is the distance traveled by the radiation;
- N_e [m^{-3}] is the electron density.

Therefore, it is possible to obtain a weighted estimate of the strength of the magnetic field along the line of sight:

$$\langle B_{||} \rangle \propto \frac{\text{rotation measure}}{\text{dispersion measure}} \propto \frac{\int N_e B_{||} \, dl}{\int N_e \, dl} \tag{3.3}$$

Different estimates exist on the average intensity of the regular galactic magnetic field, which depends on the distance from the galactic center; a mean value of $B \simeq 4\mu$G can be assumed. Its orientation is mainly parallel to the galactic plane, with a small vertical component along the z-axis ($B_z \sim 0.2$-0.3 μG in the vicinity of the Sun). Models of the large-scale structure of the galactic magnetic field exist and provide a regular distribution of the field lines that follows the distribution of matter: a spiral shape [16]. Figure 3.1 shows the direction and strength of the regular magnetic field in the galactic plane. The motion of charged particles with an energy lower than $E \sim 10^{18}$ eV (see section 2.1) is strongly influenced by the large-scale structure of the galactic magnetic field as can be seen in fig. 3.2 so that the trajectories of cosmic rays are expected to be efficiently isotropized.

3.2 Anisotropies due to the Diffusion

Even if the CR flux on Earth is consistent with isotropy, small anisotropies are expected due to several factors:

- the global leakage of CRs from the Galaxy;
- the possible contribution of individual sources;
- the motion of the solar system in the Galaxy.

It is possible to estimate the level of anisotropy of the CRs flux by estimating their net streaming velocity V because of the presence of the diffusion effect [11]. Let us consider the diffusion-loss equation [16], that is a partial differential equation that describes the energy spectrum and particle density at different points in the interstellar medium in the presence of continuous energy losses

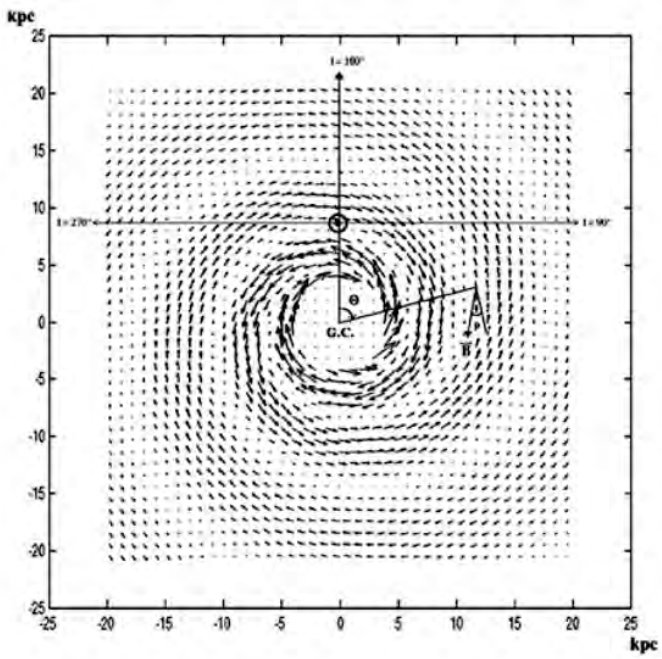

Figure 3.1: The direction and strength of the regular magnetic field in the Galactic plane is represented by the length and direction of the arrows. The intensity of the field inside the circle of radius 4 kpc representing the bulge is assumed to be 6.4 μG ([39]).

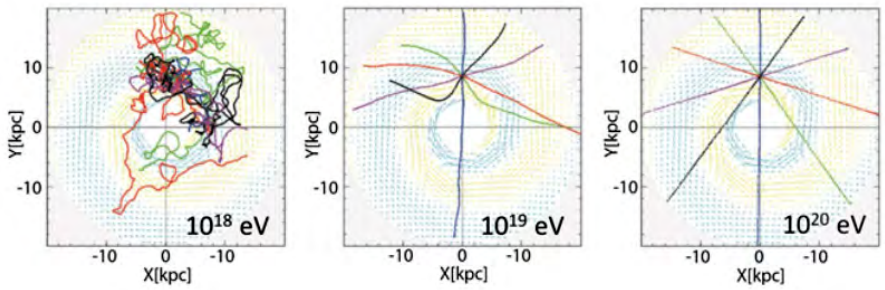

Figure 3.2: Simulated trajectory of charged particles in the galactic magnetic field. Low-energy charged particles are bent and wound by magnetic fields, but those above 10^{20} eV travel along almost straight trajectories with little influence from magnetic fields, thereby retaining the original directional information. (http://www.asi.riken.jp/en/laboratories/chieflabs/astro/index.html)

and with continuous supply of particles from the sources, in the case in which only the diffusion term is present (no sources and no energy gains or losses):

$$\frac{dN(E)}{dt} = D\nabla^2 N(E) \tag{3.4}$$

where D is a scalar diffusion coeffient (for the derivation of the formula see [16]). An order of magnitude for D can be determined from 3.4 by dimensional arguments. If we replace the spatial derivative with a division by the characteristic length scale L (the thickness of the galactic disk) and the time derivative with a division for a characteristic time τ (the escape time):

$$\frac{DN}{L^2} \sim \frac{N}{\tau} \quad \longrightarrow D \simeq \frac{L^2}{\tau_{esc}} = 3 \times 10^{27} \mathrm{cm}^2 \mathrm{s}^{-1} \tag{3.5}$$

Similarly, eq. 3.4 gives the streaming velocity:

$$\frac{N}{T} = D\frac{N}{L^2} \quad \longrightarrow \frac{L}{T} \equiv V = \frac{D}{L} \sim 10^{-4} \tag{3.6}$$

where the value $L = 300$ pc, equal to the galactic disk height, has been assumed. The presence of a cosmic ray anisotropy is strictly correlated with the streaming velocity V of the CR particles. It can be demonstrated ([40]) that, for a flux of particles (such as the cosmic rays) with differential energy spectrum $\Phi(E) \propto E^{-\alpha}$, the streaming speed and the anisotropy amplitude δ are correlated through the spectral index α by:

$$V = \left[\frac{\delta}{(\alpha+2)}\right] c \quad , \quad \delta = \frac{I_{max} - I_{min}}{I_{max} + I_{min}} \tag{3.7}$$

where c is the speed of light and I_{max} and I_{min} represent the maximum and the minimum intensity of CRs from a given direction. Since the CR escape probability increases with energy, we expect that the diffusion coefficient D is energy dependent as well. This means that the greater is the energy, the higher is the streaming velocity V, according to Eq. 3.7. Therefore the amplitude δ of the anisotropy is expected to increase with energy as well. Accurate calculations show that values as large as $\delta \sim 10^{-1}$ can be obtained, depending on particle energy and on the strength and structure of the galactic magnetic field. In partucular, predictions for an anisotropy amplitude of a dipole type (in the equatorial coordinate system), due to the difference in the arrival intensity of particles from opposite directions and usually attributed to the motion of the observer relative to the source, have been made for different energies (fig. 3.3). The amplitude of the anisotropy expected from diffusion should be in the 10^{-3} to 10^{-2} range.

The results of some experiments measuring CRs at different energies are reported in Fig. 3.3 as well. In the energy region $10^{14} - 10^{15}$ eV few evidences on large-scale anisotropies were reported from extensive air shower experiments in the last two decades, while at high energy (when the asymmetry is larger), the CR flux is so low that it can be measured only by the largest shower array detectors. The fact that an anisotropy in the arrival direction of UHECRs has not been observed is the main motivation for the hypothesis of their extragalactic origin.

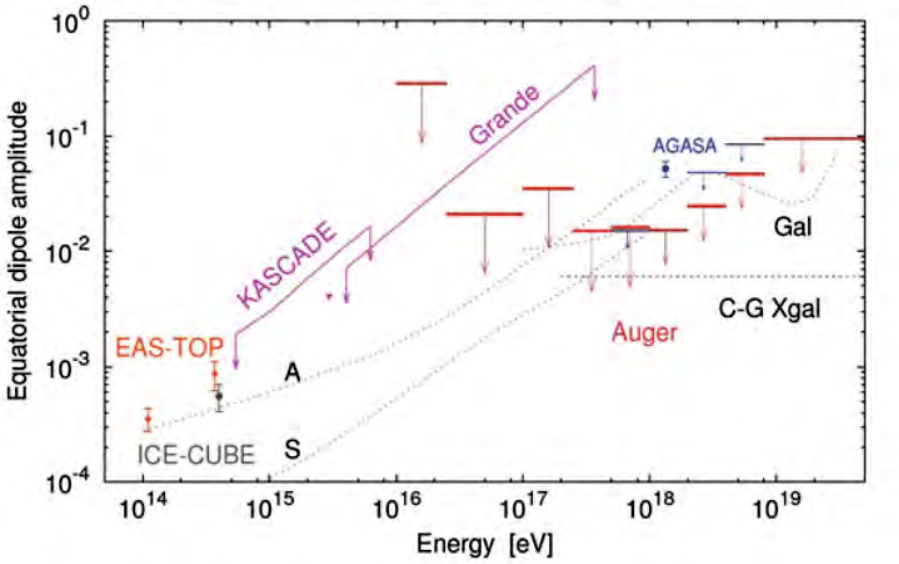

Figure 3.3: The anisotropy amplitude as a function of energy. In red are the limits obtained by the Auger Observatory over the full energy range as reported at the ICRC in 2013 ([41]). The lines denoted as A and S up to 10^{18} eV refer to predictions for two different galactic magnetic field models. (Gal) and (C-GXgal) represent the predictions for a purely galactic origin of ultra-high energy cosmic rays (UHECRs) and the expectations from the Compton-Getting effect for an extragalactic component of CRs respectively.

3.2.1 The Compton - Getting Effect

The motion of the observer on Earth relative to the frame in which CRs have no bulk motion (the galactic disk) is also expected to cause a small anisotropy. This effect, proposed in 1935 by Compton & Getting [42], predicts that the anisotropy should appear as a dipolar structure with its maximum pointed in the direction of motion of the Sun (and consequently of the Earth) within the Galaxy. Considering a value for the speed of the Sun of $V_\odot \sim 220$ km/s, the expected anisotropy amplitude due to the Compton-Getting effect can be estimated using eq. 3.7:

$$\delta_{CG} = \frac{V_\odot}{c}(\alpha + 2) \sim 10^{-3} \tag{3.8}$$

Several ground-based extensive air shower detectors and underground experiments detecting cosmic-ray muons have observed that CRs in the energy range up to 100 TeV show a large-scale anisotropy with an amplitude $\delta_{CG} \sim 0.1$ %. These observations seem to be related to the motion of the Earth in the Galaxy since the experimental values of δ are very close to the predicted one. Results of experiment like EAS -TOP ([43]) and IceCube ([44]) are shown in fig. 3.3 for energies below 10^{15} eV.

Moreover, a similar anisotropy, which may be called the Solar Compton-Getting effect, or solar dipole, is expected due to the rotation of the Earth

around the Sun. The orbital velocity of the Earth is ~ 30 km/s, which should produce a dipole with an amplitude of $\sim 10^{-4}$ with an orientation of the dipole parallel to the Earth's velocity vector. This effect has been routinely observed with cosmic-ray detectors.

3.3 Experimental Measurements of the Large Scale Anisotropy

Since the distribution of arrival directions of cosmic rays is a function defined on the celestial sphere, it can be fully characterized by a list of spherical harmonic coefficients (see Appendix B). The role of an observatory, infact, should be to map the sky and make results available in a form which is readily usable without knowledge of the detector properties and which is independent of any theoretical hypothesis. Low-order multipoles (or spherical harmonic coefficients) can summarize the large-scale information. Variations on an angular scale of θ on the sphere are related to the multipole expansion terms characterized by:

$$l = \frac{180^\circ}{\theta} \tag{3.9}$$

For cosmic ray anisotropy, in principle the analysis could look for $l = 1$ (dipole term) up to $l \sim 60$, higher order terms being irrelevant because the detector will smear out any true variations on scales that are smaller than its angular resolution. For charged cosmic rays, magnetic dispersion will presumably smear out any point source more than the detector's resolution function. Even at the highest observed particle energies, there is unlikely to be any structure in the pattern of arrival directions over angles smaller than 3° ($l > 20$). In particular, terms up to the quadrupole ($l = 2$) are of special interest since they can give relevant information:

- Monopole. It is simply the sky integral of the cosmic ray intensity. A pure monopole intensity distribution is equivalent to isotropy. The strength of other multipoles relative to the monopole is a measure of anisotropy.
- Dipole. A pure dipole distribution is not possible because the cosmic ray intensity cannot be negative in half of the sky. A "pure dipole deviation from isotropy" means a superposition of monopole and dipole. A predominantly dipole deviation from isotropy might be expected if the sources are distributed in a halo around our Galaxy. In this case, there is a definite prediction that the dipole vector should point toward the galactic center. An approximate dipole deviation from isotropy could be caused by a single strong source if magnetic diffusion or dispersion distributes those arrival directions over much of the sky. In general, a single source would produce higher-order moments as well. A dipole moment is also the expected consequence of the Compton-Getting effect (3.2.1).
- Quadrupole. An equatorial excess in galactic coordinates would show up as a prominent quadrupole moment. A measurable quadrupole is expected in many scenarios of cosmic ray origins, and is perhaps to be regarded as the most likely result of a sensitive anisotropy search.

The most commonly used technique to search for large scale anisotropies is the analysis in right ascension only, through harmonic analysis of the event counting rate, referred to as the *Rayleigh formalism* [52]. It gives the amplitude A (that can be identified with the δ given in Eq. 3.7) and phase ϕ of the first harmonic, and additionally the probability P for detecting a spurious amplitude due to fluctuations from a sample of n events which are drawn from a uniform distribution.Two quantities can be obtained from the dataset, with the sum includes n right ascension values RA_i :

$$S = \frac{2}{n}\sum_{i=1}^{n} sin(RA_i) \quad , \quad C = \frac{2}{n}\sum_{i=1}^{n} cos(RA_i) \tag{3.10}$$

If the CR arrival directions are completely random, clearly S = C = 0. In the presence of anisotropy, the amplitude A and the phase ϕ of the first harmonic are given by:

$$A = \sqrt{C^2 + S^2} \quad , \quad \phi = arctan\frac{S}{C} \tag{3.11}$$

Other analysis methods are Farward-Backward, East-West and Equi-Zenith (see Appendix C).

3.3.1 Anisotropy of TeV Cosmic Rays

One of the first important claim was published in 1998 [45] based on data from underground muon telescopes located in Japan: a significant sidereal anisotropy was detected at energies of a few hundred GeV. Such result was described as a superposition of two effects: a large-scale Galactic anisotropy with its maximum oriented towards the equatorial coordinates $\alpha = 0°$, $\delta = -20°$ and an excess flux from a cone with a half opening angle of $\sim 68°$ pointed in the direction $\alpha = 90°$, $\delta = -24°$. This excess region is usually referred to as the"tail-in" anisotropy since the excess points close to the expected direction of the magnetic tail created by motion of the heliosphere through the interstellar medium and though it is of solar origin. Moreover, the heliospheric origin of this feature is also confirmed by the observation of seasonal variation of the anisotropy: it is maximal in December when the Earth is closest to the tail and reaches a minimum in June. However, no Compton-Getting anisotropy associated with the motion of the Sun in the galaxy was observed. A wide deficit region in the direction ($\alpha = 180°$, $\delta = 20°$) was also observed and it is usually referred to as the "loss cone".

At higher energies (between 4 and 300 TeV), the analysis conducted by the Tibet-ASγ collaboration [46] showed a dipolar anisotropy in the distribution of cosmic ray arrival directions with respect to the position of the Sun with a relative amplitude of the order of 10^{-4}, compatible with the solar Compton-Getting effect (fig. 3.4).

The arrival direction distribution in the equatorial coordinate frame also showed a significant large-scale anisotropy which could be described as a dipole at the TeV energies. The location of the strongest excess region and the wide deficit in the Tibet sky map (Fig. 3.5) roughly match the "tail-in" and "loss cone" regions already mentioned. The analysis has been performed using the equi-zenith method.

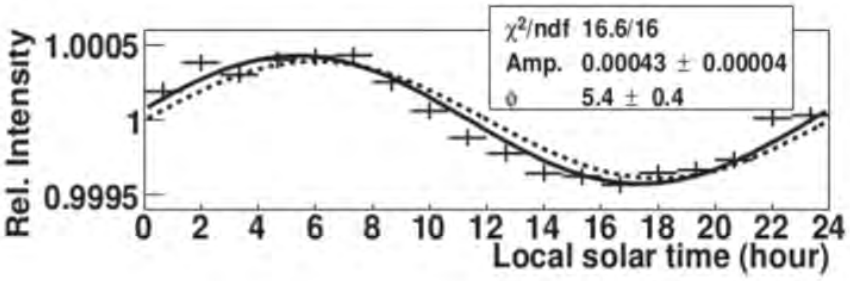

Figure 3.4: Projection of the anisotropy intensity map along the right ascension as a function of the local sideral time for the Tibet ASγ data taken from 2001-2005. The fitting function is in the form of $Amp \times cos[2\pi(T-\phi)/24]$ where the local solar time T and ϕ are in unit of hour and Amp is the amplitude. The dashed lines are from the expected CG effect, while the solid lines are the best harmonic fits, which agree very well with the prediction.

Other experiments in the Northern hemisphere, such as Super-Kamiokande [47], Milagro [48] and ARGO-YBJ [49], have observed a large-scale anisotropy compatible with that observed by Tibet-ASγ at energies of a few TeV.

- Super - Kamiokande [50]: SK-I is a 50 kiloton underground imaging water Cherenkov detector in Kamioka, Japan at an altitude of 370 m above sea level and with a vertical overburden of about 2700 meters water equivalent. The detector's design was optimized for the detection of neutrinos and nucleon decay. The overburden shields all charged cosmic ray secondaries except muons with energy above 0.8 TeV. The portion of the detector sensitive to muons is a cylinder of diameter 33.8 m and height 36.2 m, giving a target area between 1000 m^2 and 1200 m^2 depending on the zenith angle.

  The relative sidereal variation in the arrival direction of primary cosmic ray nuclei of median energy 10 TeV was measured using downward, through-going muons. Figure 3.6 shows the observed anisotropy maps in the celestial sphere. The right ascension projection of this map has a first harmonic amplitude and phase of (6.64 $\pm$ 0.98 (stat.) $\pm$ 0.55 (syst.)) $\times 10^{-4}$ and (33.2°$\pm$ 8.2 ° (stat.) $\pm$5.1° (syst.)),which are in good agreement with results from other experiments.

- Milagro: The Milagro observatory ([51]) is a water Cherenkov detector which is used to monitor extensive air showers produced by TeV gamma-rays and hadrons hitting the Earth's atmosphere. Milagro is located in New Mexico at an altitude of 2630 m above sea level. The detector is composed of an 80m $\times$ 60m $\times$ 8m pond filled with $\sim$ 23 million liters of purified water and protected by a light-tight cover. The central pond is instrumented with two layers of PMTs: a top layer with 450 PMTs under

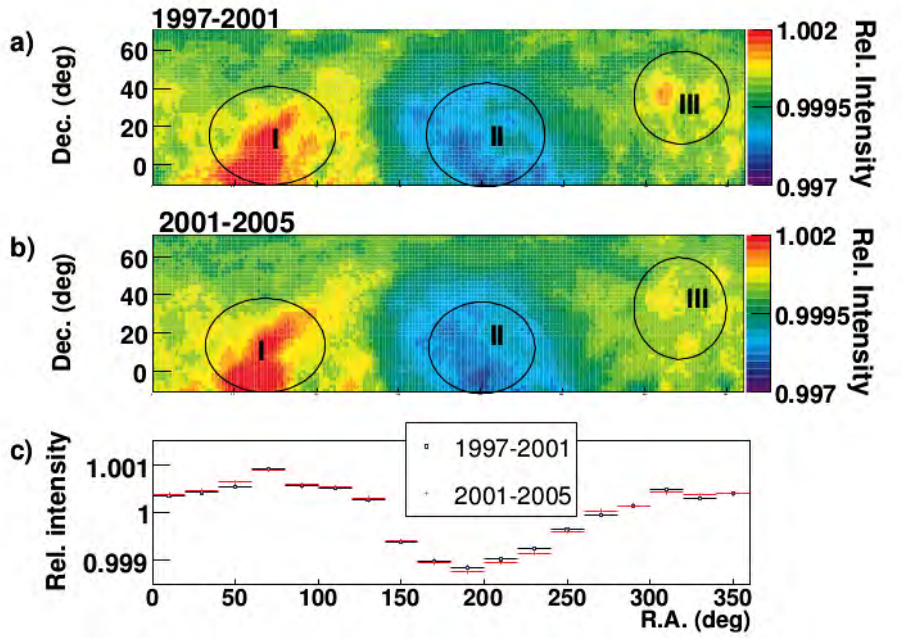

Figure 3.5: Anisotropy skymap produced by the Tibet-ASγ Collaboration ([46]) showing the so-called "tail-in" excess (I), the "loss cone" deficit (II), and a wide excess that is claimed to be associated with the Cygnus Galactic region (III). The anisotropy pattern appears to be stable in time (a) and (b). A one-dimensional projection of the anisotropy is shown in (c).

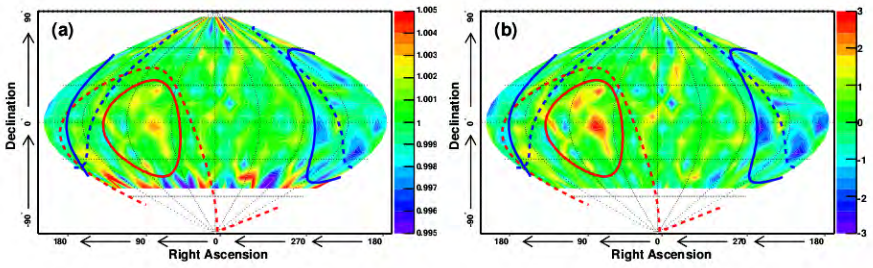

Figure 3.6: Sky map of the anisotropy in equatorial coordinates. The sky is divided into $10^\circ \times 10^\circ$ cells. Declinations less than -53.58° (white region) always lie below the horizon and are thus invisible to the detector. In (a), the color code in each cell shows the fractional variation from the isotropic flux, while in (b) it shows the standard deviation of this variation. The solid red and blue curves show the excess and deficit cones obtained using a clustering algorithm applied to the data. The dashed curves in (a,b) show excess and deficit cones from the NFJ model by combining data from several different experiments in the northern and southern hemispheres ([47])

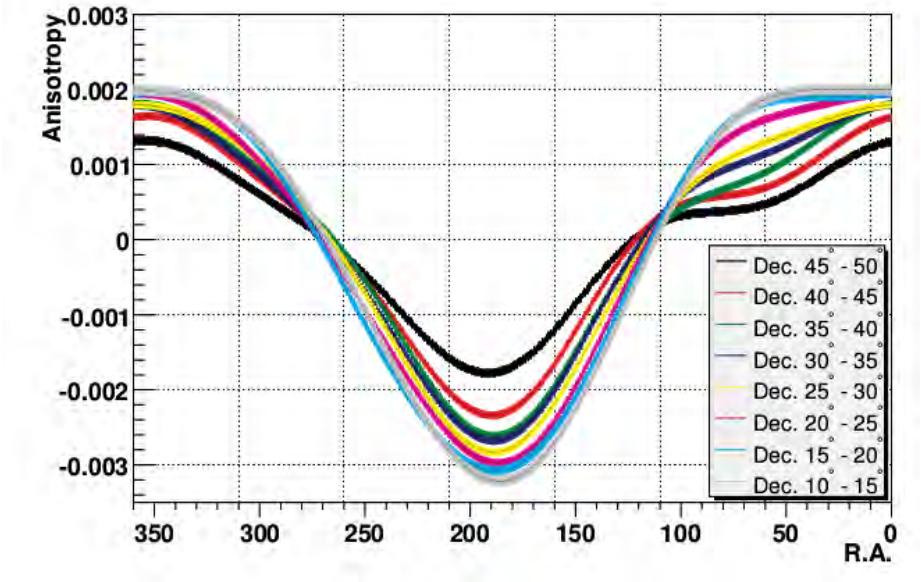

Figure 3.7: Profiles in right ascension for individual 5° declination bands from 10° to 50°. The width of the lines reflects the statistical error.

1.4m of water which detects Cherenkov light from air shower electrons, electrons Compton scattered by gamma-rays, and gamma-rays that have converted to electron-positron pairs in the water; and a bottom layer with 273 PMTs 6m under the surface used for gamma-hadron separation. The direction of an air shower is reconstructed using the relative timing of the PMTs hit in the top layer of the pond with an angular resolution of $< 1°$. This pond is surrounded by a 200m $\times$ 200m array of 175 "outrigger" tanks. Each "outrigger" is a cylindrical, polyethylene tank with a diameter of 2.4 m and a height of 1 m. The outrigger tanks contain $\sim$ 4000 liters of water and are instrumented with a single downward facing PMT located at the top of the tank.

The analysis has been performed using the forward-backward method. Because this method measures the modulation in the direction of the Earth's rotation, it yields no information about the modulation in the declination direction. The results will so be the projection of the anisotropy in the right ascension direction rather than the full 2-D anisotropy of the sky. Such a projection can be created for any visible declination band. Fig. 3.7 shows the obtained anisotropy projection along the right ascension for different declination bands. The dominant feature is a prominent valley or deficit region extending from 150° to 225° in r.a., and clearly visible in all dec. bands between $-10°$ and 45° .

- ARGO-YBJ: The Argo-YBJ experiment is an Extensive Air Shower (EAS) array, located at the Yangbajing Cosmic Ray Laboratory (Tibet, P.R.China) at an altitude of 4300 m a.s.l. The detector consists of a single layer of Resistive Plate Chambers (RPCs) operating in streamer mode and of a

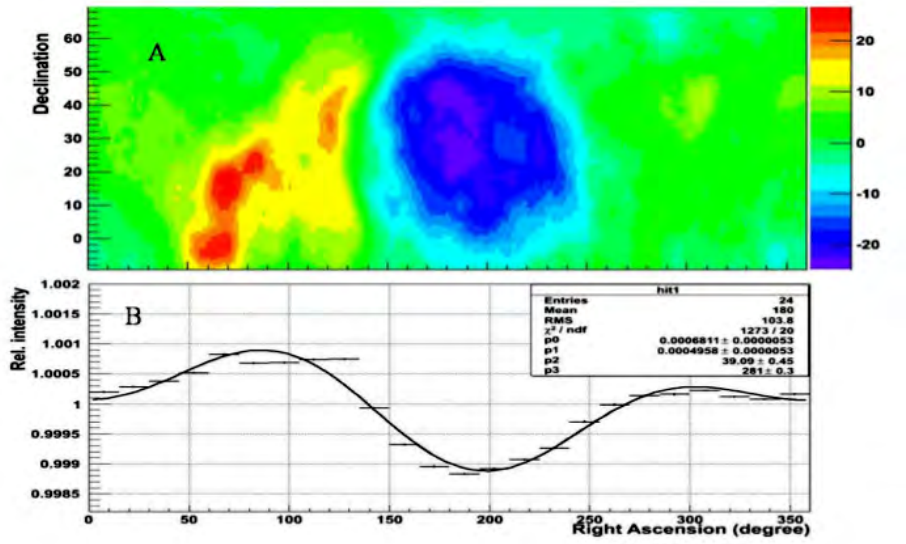

Figure 3.8: (A)Significance skymap in number of stardard deviations from the isotropic distribution of CRs in equatorial coordinate system with the data collected from January 2008 to December 2009 by ARGO-YBJ experiment. The different colors represent different significance value marked on the right of figure. (B)Relative intensity of CRs distribute as a function of Right Ascension. The smooth fitting line is the second-order cosine harmonics function $1 + P_0 cos(2\pi(x - P_2)/360) + P_1 cos(2\pi(x - P_3)/180)$.

modular structure, with the basic module being the Cluster (5.7 × 7.6 m^2), made up of 12 RPCs (2.850 × 1.225 m^2). The central area like a carpet (about 74× 78 m^2) is fully covered by 130 clusters, which is surrounded by 23 sampling guard ring clusters with a detection area of 6700 m^2 and about 93% of active area.

The analysis has been performed using the equi-zenith method. Fig. 3.8 shows the obtained significance maps in equatorial coordinates.

The large scale anisotropy is usually characterized as either a simple dipole, or the combination of dipole and quadrupole components with their respective amplitudes A and phases ϕ. A fit of this kind to the anisotropy profile δI as a function of right ascension α was applied to ARGO-YBJ data using the first two components of a harmonic expansion:

$$\delta I(\alpha) = A_1 cos(\alpha - \phi_1) + A_2 cos(2(\alpha - \phi_2)) \tag{3.12}$$

The best fit amplitudes and phases are $A_1 = 6.8 \times 10^{-4}$, $A_2 = 4.9 \times 10^{-4}$ and $\phi_1 = 39.1^\circ$, $\phi_2 = 281^\circ$ which are compatible with results from Tibet.

3.3.2 Anisotropy of PeV Cosmic Rays

Above a certain energy, it is expected that particle paths are no longer compatible with random walks in the galaxy since at high energies the effect of the

Galactic magnetic field should be less noticeable on the trajectories of cosmic rays. Even if the energy where this transition occurs is not known due to the uncertainties in the Galactic magnetic field and in the composition of the particles, it is likely that it may happen somewhere in the PeV to EeV energy range. The first claim of observation of cosmic ray anisotropy at energies above a few hundred TeV was presented by the EAS-TOP collaboration [43] in 2009. The EAS-TOP Extensive Air Shower array was located at Campo Imperatore (2005 m a.s.l., INFN Gran Sasso National Laboratory). The electromagnetic detector consisted of 35 modules of scintillator counters, 10 m^2 each, distributed over an area of about 10^5 m^2.

The analysis has been performed using the East-West method. One-dimensional projections of the anisotropy profiles in right ascension were reported for two energy bins with median energies of 110 and 370 TeV. The amplitude and phase of the observed anisotropy were parametrized by fitting first and second harmonic functions. High stability data obtained from long time observations (8 years) from the EAS-TOP array confirm the amplitude and phase of the cosmic ray anisotropy already reported at 10^{14} eV. The result is supported by the observation of the Compton-Getting effect due to the revolution of the Earth around the Sun. At higher energies the observed anisotropy shows a larger amplitude, and a different phase. The dependence of the anisotropy amplitude over primary energy deduced from the two measurements is compatible with that of the diffusion coefficient. On another side, the sharp increase of the anisotropy above 10^{14} eV may be indicative of a sharp evolution of the propagation properties, and so of the diffusion coefficient just approaching the steepening of the primary spectrum. This opens the problems of obtaining an improved theoretical and experimental description of the whole evolution of the diffusion processes vs primary energy, and understanding how such evolution could affect the energy spectra at the "knee".

3.3.3 Anisotropy Studies in the Southern Hemisphere

The first report of significant anisotropy in the southern sky at TeV energies was presented by IceCube in [19]. The IceCube Observatory, completed in December 2010, is currently the only km^3 scale neutrino telescope collecting data. The detector consists of an array of 5,160 digital optical sensors arranged along 86 strings (IC89) between 1,450 and 2,450 meters below the geographic South Pole, where the deep Antarctic ice is particularly transparent. IceCube also includes a surface shower array, IceTop, and a dense instrumented core with a lower energy threshold, DeepCore. Although designed to detect high energy extra-solar neutrino, IceCube can be used to indirectly study cosmic rays via the high energy muons produced in the interaction of cosmic rays with Earth's atmosphere. The method of reconstruction of both the direction and the energy of the muon is similar to the one used for the ANTARES telescope and will be described in the next section.

A significant large angular scale anisotropy was reported by Icecube ([19]) using a data set of 4.3 billion events recorded with the IC22 (22 strings) configuration. A map of relative intensities is shown in Fig. 3.9 where the large scale structure in the southern sky is quantified by the color code. The one-dimensional projection of the anisotropy sky map in the right ascension coordinate was parametrized using the first two components of a harmonic expansion

(eq. 3.12). The anisotropy is similar in amplitude, angular size, and orientation as that observed by experiments in the northern emisphere.

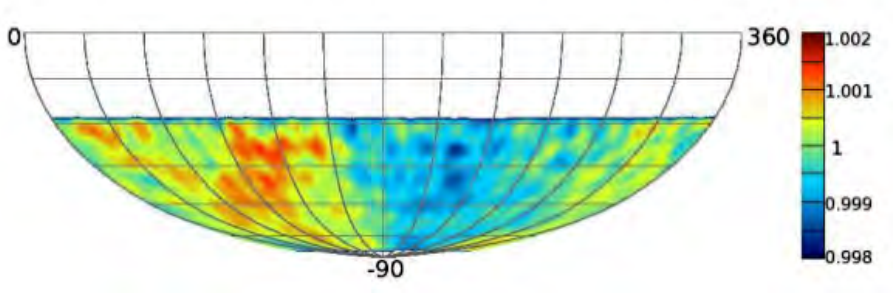

Figure 3.9: The relative intensity quantified by the color code of the cosmic ray flux in equatorial coordinates.

3.3.4 Neutrino - Cosmic Rays connection in the Galaxy

It has recently been investigated ([54]) the neutrino - cosmic ray connection for sources in the Galaxy in terms of two observables: the shape of the energy spectrum and the distribution of arrival directions. To quantify the spectral features characteristic of Galactic CR models the "leaky box" picture has been adopted: CRs propagate freely in the Galaxy, contained by the magnetic field but with some probability to escape which is constant in time. The local energy density is given by

$$n_{CR}(E) \approx Q(E)\tau(E/Z) \tag{3.13}$$

where $Q(E) \propto E^{-\alpha}$ is the generation rate of primary CRs and $\tau(E/Z) \propto E^{-\delta}$ is the rigidity-dependent confinement time. Fits to the energy dependence of secondary to primary ratios yield $\delta = 0.6$ (2.2.1). Even if, for a source index $\alpha \sim 2.07$, which is close to the prediction of Fermi shock acceleration, inclusion of propagation effects reproduces the observed spectrum, $\delta = 0.6$ results in an excessively large anisotropy which is inconsistent with the current upper limits. Consistency with anisotropy can instead be achieved by adopting an index, $\delta = 1/3$ that can be justified through small variations of the energy dependence of the spallation cross sections, or variation in the matter distribution in the Galaxy, but this implies a steeper source spectrum, $\alpha \sim 2.34$. Therefore, in the hypothesis of hadronic and optically thin CR sources in the Galaxy, one would expect a flux of neutrinos with a spectrum $\propto E^{-2.34}$ and with energies up to 2 to 3 PeV (following from the Hillas criterion). Quite recently the IceCube Collaboration has reported a preliminary observation of 26 neutrino candidates [53] which, in addition to the two $\sim$ 1 PeV neutrinos reported earlier in 2013, constitute a 4.1σ excess compared to expectations from background. However, if one makes the common assumption of an unbroken E_ν^{-2} neutrino energy spectrum, then one expects to observe about 8-9 events with energies higher than the two highest energy events observed so far. The IceCube observations seem to be compatible with the hypothesis of an unbroken power-law spectrum arising from optically thin Galactic neutrino sources, finding a cosmic neutrino flux

per flavor, averaged over all three flavors consistent with the data reported so far [55]. Finally in [54] the consistency between the arrival direction distribution of the IceCube excess and the hypothesis that the sources are nearby was commented. Fourteen of the 26 reported neutrino events arrive from within about 15° of the Galactic plane, including one of the two highest energy events, which coincides with the Galactic center (within errors). The highest energy event is outside of this angular window, but does correspond with a possible hotspot in the IceCube photon search. This could reflect emission of neutrinos and high energy γrays from a common, nearby source, as γ rays do not survive a propagation further than ~ 10 kpc. The recently discovered large reservoir of ionized gas extending over a large region around the Milky Way is suggested as the target material required for neutrino production outside the Galactic disk in models in which proton diffusion extends to the Galactic halo. However, given the current statistics and the uncertainties in the knowledge of the atmospheric (in particular the prompt neutrino) background, they conclude that the arrival direction distribution neither favors nor disfavors a Galactic origin.

Chapter 4

The ANTARES neutrino telescope

The existence of hadronic CRs sources could be demonstrated only by observing high-energy neutrinos, in addition to $\gamma - rays$ since detailed modeling of the morphology and spectra of $\gamma - rays$ sources seems to indicate a preference for their production through the leptonic mechanism. Here comes the astronomy based on neutrinos: thanks to their unique properties (small interaction cross-section and neutral charge), it is expected to be decisive in the quest of CR souces. The idea of the cosmic neutrinos detection based on the use of a large volume experiment exploiting the secondary particles produced in neutrino inteactions was first formulated in the 1960s by M. Markov [20]. He proposed: *"to install detectors deep in a lake or in the sea and to determine the direction of the charged particles with the help of Cherenkov radiation"*. At present a km^3 detector (IceCube) is operating in the ice of the South Pole and another smaller underwater telescope (ANTARES) is running in the Mediterranean Sea, waiting for the Mediterranean km^3 telescope (KM3NeT). All of them use the Markov idea and are made by a grid of optical sensors (photomultipliers, PMTs) inside the so-called instrumented volume. The results presented in this work are based on data collected using the ANTARES detector.

4.1 Neutrino Detection Principle

High energy neutrinos interact with a nucleon N (or better with quarks) of the nucleus, via either charged current (CC) weak interaction

$$\nu_l + N \rightarrow l + X \qquad (l = e, \mu, \tau) \tag{4.1}$$

or neutral current (NC) weak interactions

$$\nu_l + N \rightarrow \nu_l + X \qquad (l = e, \mu, \tau) \tag{4.2}$$

In fig. 4.1 we show the evolution, with the energy, of neutrino - nucleon interaction cross-section.

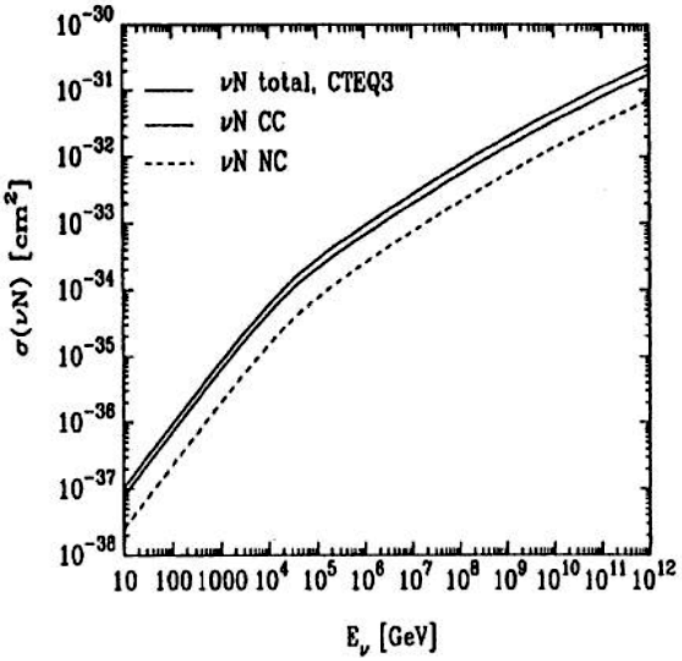

Figure 4.1: Neutrino - nucleon interaction cross-section [58]

The trasparent medium, such as ice or water, in which the detector is placed, at great depths, offers a large volume of free target nucleons for neutrino interactions. Moreover, it acts as a shield against secondary particles produced by CRs in the atmosphere and allows the propagation of Cherenkov photons. Indeed, the detection principle is based on the collection of the optical photons produced by the Cherenkov effect of relativistic particles [21], whose light is measured by a three-dimensional array of photomultiplier tubes (PMTs). The neutrino flavor, direction and energy are then inferred on the base of number of photons detected and arrival times.

4.1.1 Cherenkov Radiation

When a relativistic charged particle enters a refractive medium, Cherenkov radiation is emitted if the velocity v of the charged particle is larger than the speed of light in the medium. The speed of light in a medium is given by c/n where c is the speed of light in vacuum and n is the index of refraction of the medium, which implies that the condition for Cherenkov emission is $v > c/n$. The constructive interference of electromagnetic waves creates a cone-shaped wavefront that is characteristic of Cherenkov light. The opening angle of the cone θ_c is given by

$$cos\theta_C = \frac{1}{\beta n} \tag{4.3}$$

with $\beta = v/c$. The process is shown schematically in Fig. 4.2 for a highly relativistic particle ($\beta \sim 1$). As an example, a relativistic muon traveling through

water ($n \sim 1.364$) would produce a light cone with an angle of $\theta \sim 43°$.

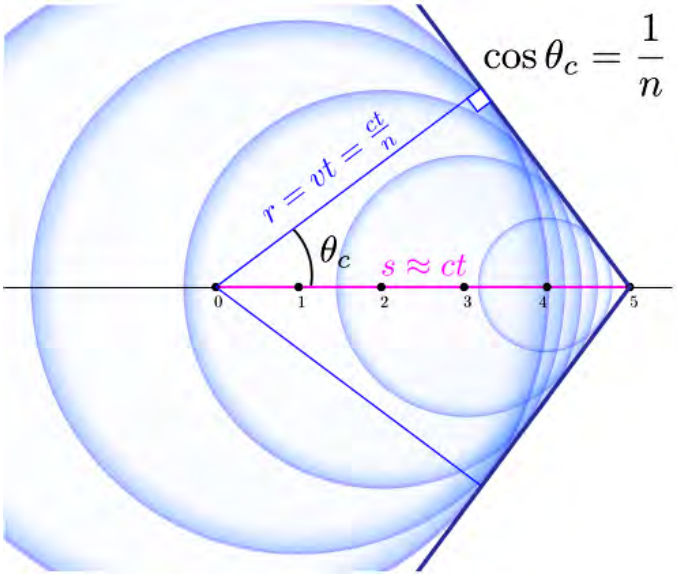

Figure 4.2: Illustration of Cherenkov radiation emission by a highly relativistic particle ($\beta \sim 1$) as it moves through a medium with refractive index n. Waves emitted at the numbered positions along the particle path add constructively to form a conic wavefront with opening angle θ_C .

The number of Cherenkov photons, N_C, emitted per unit wavelenght interval $d\lambda$ and unit distance travelled, dx, by a charged particle of charge e is given by

$$\frac{d^2N_C}{dxd\lambda} = \frac{2\pi}{137\lambda^2}(1 - \frac{1}{n^2\beta^2}) \tag{4.4}$$

where λ is the wavelenth of the radiation. Shorter wavelengths contribute more significantly to Cherenkov radiation but light absorption by water/ice will strongly suppress photons with wavelenghts below 300 nm (fig. 4.3 left). The PMT quantum efficiency (fig. 4.3 right) is large in the wavelength range $300 - 600$ nm, matching well the region in which ice and water are transparent to light.

4.1.2 Event Topology

Two main event classes can be distinguished in a large volume neutrino telescope: events with a long track due to a passing muon, and events with a shower, without the presence of a muon. Fig. 4.4 shows schematic views of ν_e, ν_μ and ν_τ CC events and of a NC event.

For the detection of track and shower events different strategies are used.

- Muon neutrinos: a muon crossing the detector gives a clean experimental signal in respect to the shower case since the path length of a muon in water exceeds that of a shower by more than 3 order of magnitude for energies above 2 TeV (fig. 4.5). This allows an accurate reconstruction

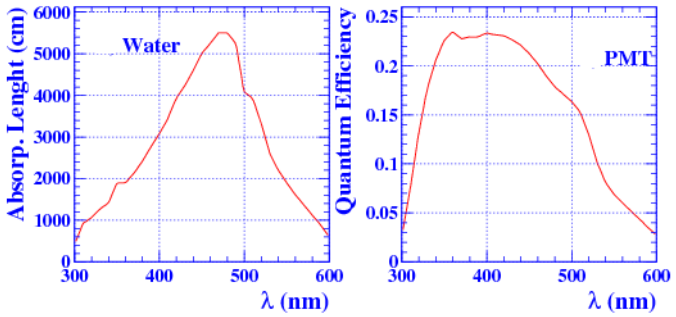

Figure 4.3: Left: Absorption length of sea water as a function of wavelength. Right: quantum efficiency for a bialkali (Hamamatsu) photomultiplier tube.

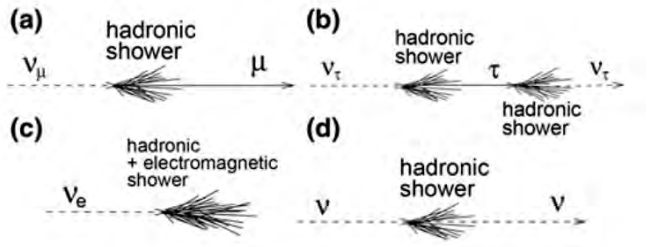

Figure 4.4: Some event signature topologies for different neutrino flavors and interactions: a CC interaction of a ν_μ produces a muon and a hadronic shower; b CC interaction of a ν_τ produces a τ that decays into a ν_τ , tracing the double bang event signature. c CC interaction of ν_e produces both an EM and a hadronic shower; d a NC interaction produces a hadronic shower. Particles and anti-particles cannot be distinguished in large volume neutrino detectors

of muon direction, closely correlated with the neutrino direction and thus with the neutrino source since neutrinos are not deflected by magnetic fields.

The muon direction (and, optionally, muon energy) is determined by maximizing a likelihood which compares the time and position of fired PMTs with the expectation from the Cherenkov signal of a muon track. Fig. 4.6 shows the angular resolution estimated as the difference between the reconstructed and the true muon direction ($\bar{\theta}_{\mu_\tau\mu}$) as a function of the neutrino energy. The angular resolution estimated as the difference between the reconstructed muon and the true neutrino direction ($\bar{\theta}_{\mu_\tau\nu}$) is reported as well. The best achievable angular resolution is of the order of $\sim 0.2^\circ$.

- Electron neutrinos: when a high-energy electron is produced in a charged current ν_e interaction, it radiates a photon via bremsstrahlung after few tens of cm of water/ice (the radiation length in water is 36 cm), process that leads to the development of an electromagnetic (EM) cascade. A typical 10 TeV electron induces a shower of length of $\sim$ 8 m. Such a length is short compared to the spacing of the PMTs in any existing or proposed high-energy neutrino detector, thus EM showers represent nearly

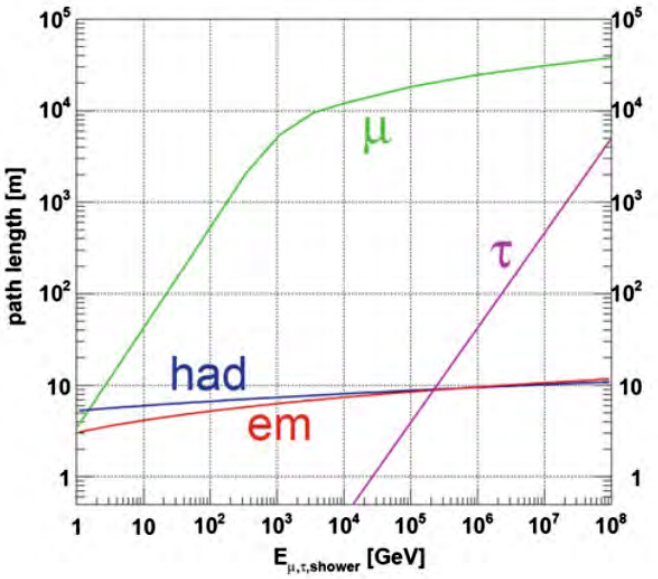

Figure 4.5: Path length of particles produced by neutrino interactions in water: muons, taus, electromagnetic (em) and hadronic (had) showers, versus their respective energy.

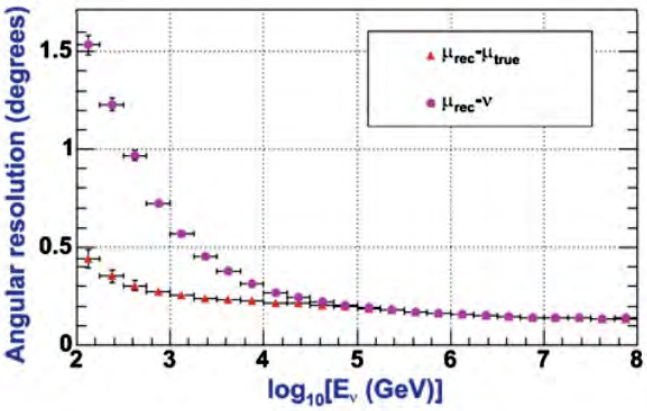

Figure 4.6: Angular resolution (evaluated with a Monte Carlo simulation) as a function of event energy for the underwater ANTARES detector. It is shown here the average differences between the true and reconstructed muon direction as well as the difference with respect to the neutrino direction

a point source of Cherenkov photons that are emitted almost isotropically along the shower axis. Pointing accuracy for showering events is thus much inferior to that achieved in the ν_μ channel.

- Tau neutrinos: the produced τ -lepton travels some distance (depending on its energy) before decaying and producing a second shower. The

Cherenkov light emitted by the charged particles in the showers can be detected if both the ν_τ interaction and the τ decay occur inside the instrumented volume of the detector. Below 1 PeV, also the ν_τ CC channels (except for the case where the τ produces a muon) belong to the class of showering events, because the τ track cannot be resolved. For energies greater than 1 PeV, the expected signature for the ν_τ CC event is the so-called double bang event: a shower, plus a track, followed by a second shower.

- NC and hadronic showers: The NC channel gives the same signature for all neutrino flavors. A fraction of the interaction energy is always carried away unobserved by the outgoing neutrino increasing the error on the reconstructed energy of the primary neutrino. The ν_e CC and the ν_x NC channels are not distinguishable in large volume neutrino detectors.

4.1.3 Atmospheric Background

The main background in a large volume neutrino detector is due to both atmospheric muons and neutrinos produced by CRs interacting with atmospheric nuclei. Up to $\sim$ 100 TeV, muons and neutrinos are produced mainly by decays of charged pions and kaons in the cascade and their spectra are related by the kinematics of the $\pi \to \mu\nu$ and $K \to \mu\nu$ decays. Additional lower energy neutrinos are produced by muon decays.

- The atmospheric neutrino flux from charged pion and kaon decays that is dominated by ν_μ and it is usually referred to as the conventional atmospheric neutrino flux. At energies above 1 TeV and up to $\sim$ 100 TeV, the conventional atmospheric neutrino intensity can be expressed with a simple power-law spectrum:

$$\frac{d\Phi_\nu(E)}{dE} \propto E^{-\alpha} \tag{4.5}$$

  where $\alpha \sim 3.7$. Interactions of primary CRs with atmospheric nuclei produce also charmed mesons. Their immediate decay yields a harder neutrino energy spectrum ($\alpha \sim 2.7$), known as prompt neutrino flux, which is expected to exceed that of conventional neutrinos above $\sim$ 10-100 TeV. Atmospheric neutrinos represent an irreducible background in experiments aiming at the detection of cosmic neutrinos. However, since the atmospheric neutrinos spectrum decreases more rapidly with respect to a possible astrophysical neutrino flux ($\alpha \sim 2$), the observation of an energy distribution in logarithmic scale with a smaller slope would indicate events associated to (extra)galactic neutrinos.

- The atmospheric muons can penetrate the atmosphere and up to several kilometers of ice/water and represent the bulk of reconstructed events in any large volume neutrino detector. Neutrino detectors must be located deeply under a large amount of shielding in order to reduce the background. The flux of downgoing atmospheric muons exceeds the flux of muons induced by atmospheric neutrino interactions by many orders of

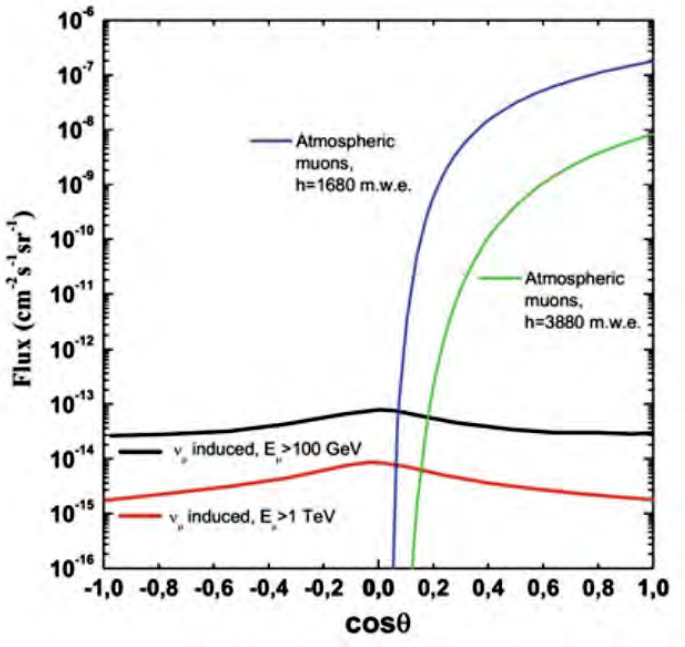

Figure 4.7: Flux as a function of the cosine of the zenith angle of: (i) atmospheric muons for two different depths; (ii) muons induced by CC interactions of atmospheric ν_μ, for two different muon energy thresholds E_μ . Upgoing (downgoing) events have $cos\theta < 0 (> 0)$

magnitude, decreasing with increasing amount of matter crossed as shown in Fig. 4.7.

The events due to the flux of down-going atmospheric muons can be rejected using the Earth as a filter, i.e. observing only up-going tracks since they are necessarily associated to neutrinos having traversed the Earth. Atmospheric muons can be used for a real-time monitoring of the detector status and for detector calibration. However, they represent a major background source: downward going particles wrongly reconstructed as upward going and simultaneous muons produced by different CR primaries could mimic high-energy neutrino interactions.

The use of up-going tracks in order to remove the atmospheric muon background can be performed up to $E \sim 1 \div 10$ PeV since for greater energies the Earth becomes opaque to neutrinos. As shown in fig. 4.1 , the neutrino - nucleon interaction cross-section increases with energy. The probability of a neutrino not being absorbed as it passes through the Earth depends on the density of matter along its path and the neutrino interaction cross-section [59]:

$$P_{Earth}(E_\nu) = exp\left(-N_A \sigma_\nu(E_\nu) \int \rho(\theta, l)\, dl\right) \tag{4.6}$$

where N_A is the Avogadro number, $\sigma_\nu(E_\nu)$ is the cross-section and $\rho(\theta, l)$

is the density profile of the Earth, function both of the neutrino direction (θ) and of the travelled distance inside the Earth (l). As shown in fig. 4.8, the Earth becomes opaque to neutrinos for $E \sim 1 \div 10$ PeV. Therefore, it is possible to observe such energetic neutrinos only if they are down-going, focusing on almost horizontal tracks in order to remove the atmospheric muon background.

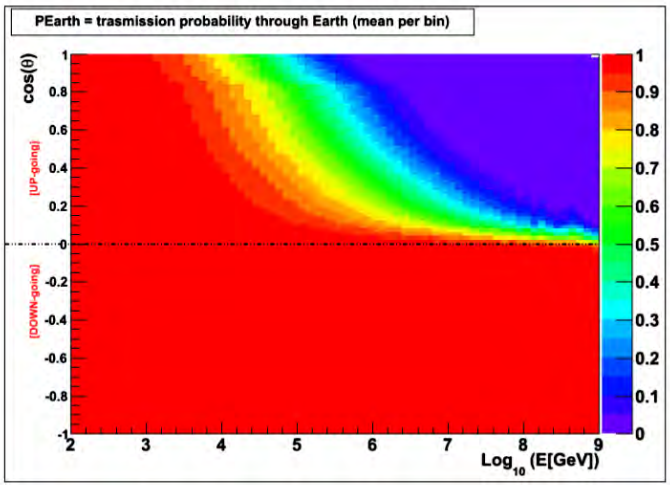

Figure 4.8: Probability (indicated by the color code) for both an up-going and a down-going neutrino not being absorbed as it passes through the Earth as a function of energy and direction.

4.2 Medium Properties

The two main effects of the medium (water or ice) on light propagation are absorption, that reduces the amplitude of the Cherenkov wavefront, i.e., the total amount of light arriving on PMTs, and scattering of photons, which changes the direction of the Cherenkov photons and consequently delays their arrival time on the PMTs; this degrades the measurement of the direction of the incoming neutrino.

The propagation of light in a transparent medium is quantified for a given wavelength λ, by the medium inherent optical properties: absorption $a(\lambda)$, scattering $b(\lambda)$ and attenuation $c(\lambda) = a(\lambda) + b(\lambda)$ coefficients, or, alternately, absorption $L_a(\lambda) = a(\lambda)^{-1}$, scattering $L_b(\lambda) = b(\lambda)^{-1}$ and attenuation $L_c(\lambda) = c(\lambda)^{-1}$ lengths. Each of these lengths represents the path after which a beam on initial intensity I_0 at wavelength λ is reduced in intensity by a factor of $1/e$ through absorption and scattering, according to the following relation:

$$I_i(x, \lambda) = I_0(\lambda) e^{-x/L_i(\lambda)} \qquad i = a, b, c \tag{4.7}$$

where x (in meters) is the optical path traversed by the light.

$L_a \sim 70$m for clear ocean waters, while it is ~ 100m in deep polar ice in the blue-UV region. This means that the same instrumented volume of ice corresponds to a larger effective volume with respect to seawater. On the other

hand, the effective scattering length for ice is smaller than water due to impurities trapped in the ice. Nevertheless, the ice is almost background-free from radioactivity. The background in seawater has two main natural contributions: the decay of radioactive elements dissolved in water, and the luminescence produced by organisms, the so-called bioluminescence. The ^{40}K is by far the dominant of all radioactive isotopes present in natural seawater. The beta-decay of ^{40}K is above the threshold for Cherenkov light production. Bioluminescence is due to two main phenomena in deep sea: steady glow of bacteria and flashes produced by animals. These can give rise to an optical background which occasionally can reach a level of several orders of magnitude larger than that due to ^{40}K.

4.3 Track Reconstruction

The muon trajectory can be completely described by the direction $\vec{d} \equiv (d_x, d_y, d_z)$ and the position $\vec{p} \equiv (p_x, p_y, p_z)$ of the muon at some fixed time t_0 since, at energies above the detection thresholdd (10 GeV), the muon is relativistic, hence, the speed of the muon is taken to be equal to the speed of light in vacuum and the trajectory to a straight line . The direction can be parameterised in terms of the azimuth and zenith angles θ and ϕ: $\hat{d} = (sin\theta cos\phi, sin\phi sin\theta, cos\theta)$ (fig. 4.9).

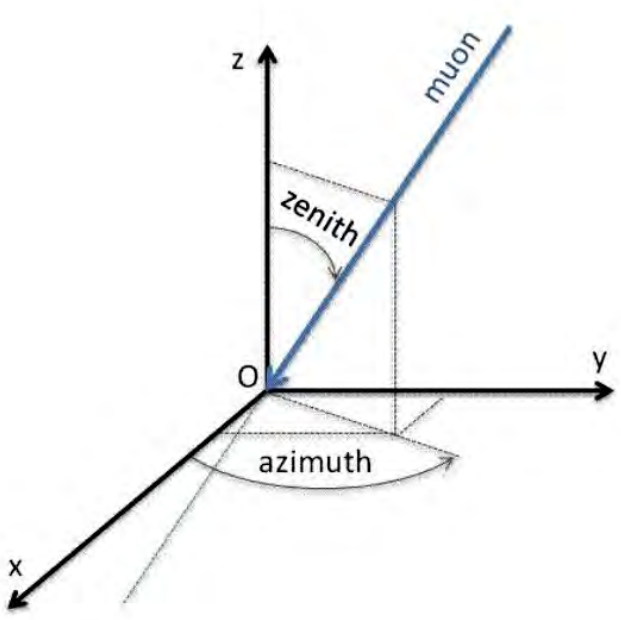

Figure 4.9: Definition of zenith (θ) and azimuth (ϕ) angles of the track.

There are thus five independent parameters that have to be estimated by the reconstruction algorithm $(p_x, p_y, p_z, \theta, \phi)$ and that univocally identify the muon track. For a given track (i.e. a given set of the five parameters), and an OM at position $\vec{q}$, the expected (theoretical) arrival time (t^{th}) of the Cherenkov

photon, emitted at an angle Θ_C with respect to the muon direction, is:

$$t^{th} = t_0 + t_1 + t_2 \tag{4.8}$$

where $t_1 = |\vec{OA}| \times \frac{1}{c}$ is the time it takes for the muon to reach the point in which the Cherenkov photon is emitted (A in fig. 4.10) and $t_2 = |\vec{AB}| \times \frac{n}{c}$ is the time it takes for the photon to reach the OM (B in fig. 4.10).

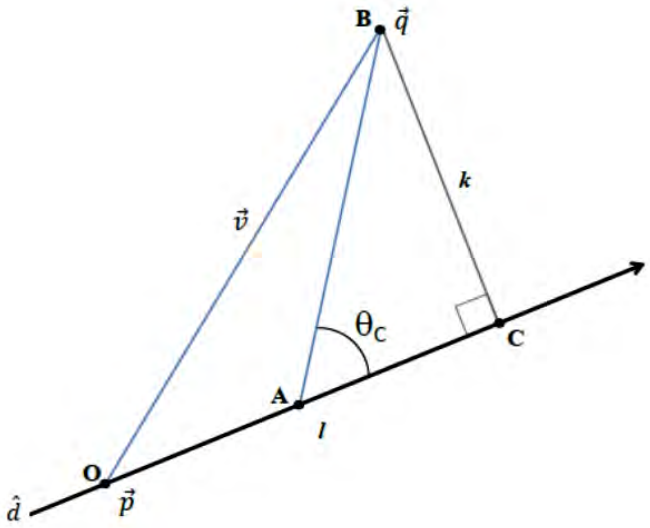

Figure 4.10: Track reconstruction scheme.

If we define

$$\vec{v} = \vec{q} - \vec{p} = \vec{OB} \tag{4.9}$$

we obtain

$$|\vec{l}| = \vec{v} \cdot \hat{d} = |\vec{OC}| \tag{4.10}$$

thus

$$k = \sqrt{|\vec{v}|^2 - |\vec{l}|^2} \tag{4.11}$$

which represents the minimum distance between the track and the OM. The arrival time of the photon to the OM is then:

$$t^{th} = t_0 + \frac{1}{c}\Big(l - \frac{k}{tan\Theta_C}\Big) + \frac{1}{v_g}\frac{k}{sin\Theta_C} \tag{4.12}$$

where $v_g = \frac{c}{n}$ is the group velocity of light in water.

The relation 4.12, for any quintuple $(p_x, p_y, p_z, \theta, \phi)$, gives the expected arrival time of the Cherenkov photons on the PMTs of the apparatus.

The ANTARES collaboration has implemented several algorithms for the muon trajectory reconstruction which make use of recorded information such as the arrival times of the photons on the PMTs (hits), the PMTs position and the deposited charge. The two most used algorithms are **AAFit** and **BBFit**.

4.3.1 BBFit

The BBFit algorithm [25] is based on the minimization of a χ^2 function defined as the squared error between theoretical (t_{th}) and measured (t_i) arrival times of the hits on the PMTs (eq. 4.13).

$$\chi^2(t_i, t_{th}) = \sqrt{\frac{(t_i - t_{th})^2}{\sigma_i^2}} \tag{4.13}$$

Since t_{th} is a function of the quintuple $(p_x, p_y, p_z, \theta, \phi)$, the minimization procedure gives the best set of parameters describing the track associated with the hits. This algorithm reconstructs with high efficiency the muon direction with an angular resolution of the order of 1°. Fig. 4.11 shows the χ^2 distribution for both data and simulated events; data are well discribed by MonteCarlo events.

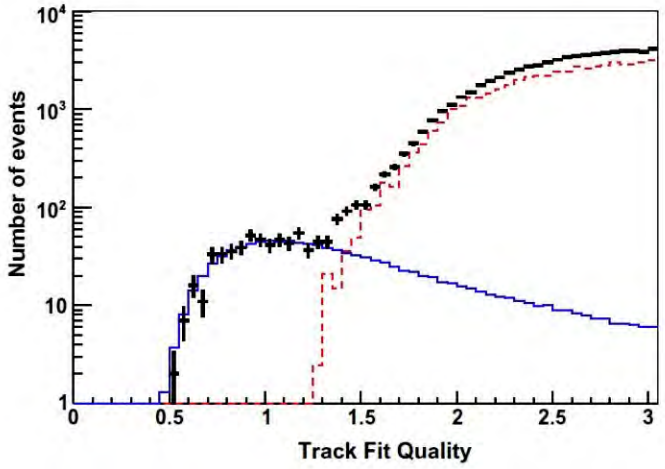

Figure 4.11: χ^2 distribution for data collected in 2008 (black), simulated downgoing atmospheric muons (red) and simulated atmospheric neutrinos (blue) ([25]).

4.3.2 AAFit

The AAFit algorithm [26] is based on a maximum likelihood method in which the best set of parameters describing the track is estimated by means of a recursive fit procedure used to maximise the likelihood of the times of the observed hits. The parameter that gives the reconstruction quality is:

$$\Lambda \equiv \frac{logL}{N_{DOF}} + 0.1(N_{comp} - 1) \tag{4.14}$$

where N_{DOF} is the number of degrees of freedom of the track $(N_{hit} - 1)$, N_{comp} is the number of compatible solutions and $\log L$ is the likelihood logarithm. The likelihood function is the pdf of time residuals r defined as the difference between theoretical (t_{th}) and measured (t_i) arrival times of the hits

on the PMTs. The error on the direction of the reconstructed muon can be estimated as:

$$\beta = \sqrt{sin^2(\theta_{rec})\sigma_\phi^2 + \sigma_\theta^2} \tag{4.15}$$

where σ_θ and σ_ϕ are the estimated errors on the track zenith and azimuth. More than 50% of events are reconstructed with $\beta < 0.46°$ [27]. Fig. 4.12 shows the Λ distribution for both data and simulated events reconstructed by AAFit as up-going with $\beta < 1°$.

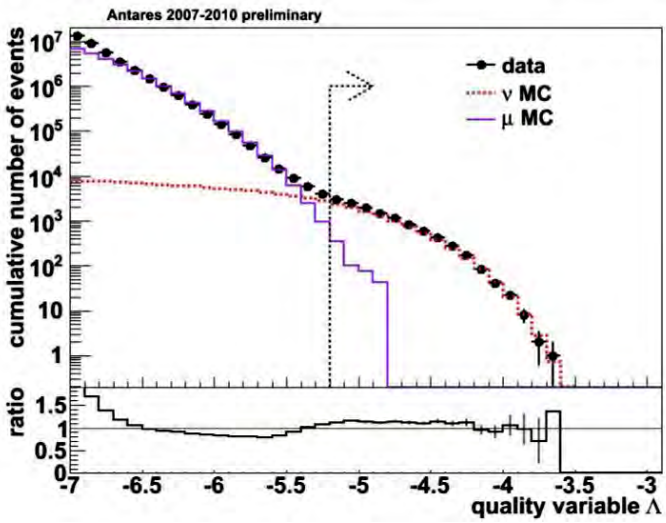

Figure 4.12: Λ distribution for data collected between 2007 and 2010 (black), simulated down-going atmospheric muons (magenta) and simulated atmospheric neutrinos (red). The bottom panel shows the ratio between observed and simulated events. The arrow shows the position of the applied cut ([27]).

4.4 Detector response

The determination of the direction and of the energy of the incoming neutrino is affected by instrumental uncertainties due both to the physical processes that involve neutrinos and muons and to systematic errors in the detection and reconstruction of tracks methods.

4.4.1 Angular uncertainty

The estimation of the angular uncertainty on the neutrino arrival direction is of great importance, in particular in point-sources analysis. Its determination depends on three main factors: the muon emission angle with rispect to the incoming neutrino direction, the muon deviation in water due to multiple scattering and the detector resolution in determining the muon track. Fig. 4.13 shows the overall effect due to the first two factors. For energies grater than 1 TeV, the mean angle between the muon and the neutrino directions is 0.7° and decreases for increasing energies.

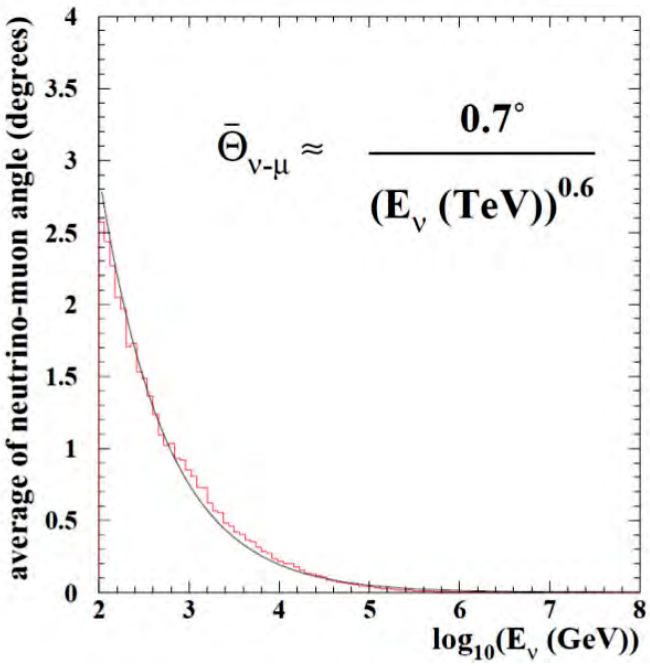

Figure 4.13: Angle between the muon and the neutrino reconstructed directions as a function of the neutrino energy. The shown function (black line) reproduces the dependence on energy.

The detector resolution depends on the quality of the alignment of the detector components, on the PMTs temporal resolution, on the global time of the readout system and on the quality of the reconstruction of muon tracks. The presence of Cherenkov light emitted by secondary particles (propagating through different directions with respect to those of muons) and diffuse light make harder the reconstruction of the muon track. MonteCarlo simulations show that for $E \geq 10$ TeV it is possible to obtain an angular resolution of 0.2°. Above 100 TeV the total angular resolution is dominated by effects due to the detector while under 10 TeV it depends on the kinematic of neutrino interactions. Simulations show that, for point-sources with a neutrino spectrum $\propto E^{-2}$, the reconstructed direction of half of the events differs from the source position by less than 2°. Over 10 TeV, the angular resolution does not depend on the $\Theta_{\nu-\mu}$ angle anymore but only on the track reconstruction uncertainty (fig 4.14).

4.4.2 Neutrino reconstruction energy

As for the angular resolution, the energy determination is affected by uncertainties on the physical processes that characterize the neutrino interactions and on instrumental uncertainties. The detector response to the neutrino energy is related to the fraction of energy transferred to the muon, the energy lost by the muon outside the detector volume and the energy resolution of the detector. The method used for its determination is different for different energy ranges.

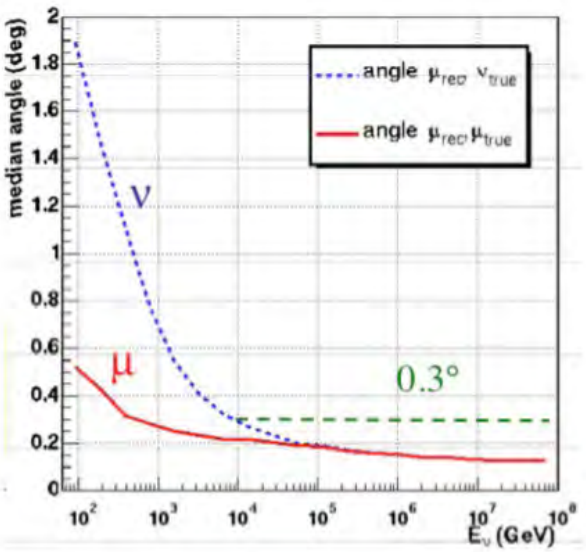

Figure 4.14: Detector angular resolution as a function of the neutrino energy. The red line shows the angle in spece between the reconstructed muon track and that generated with MonteCarlo simulations. The blue line shows the angle between the neutrino and the produced muon.

Below 100 GeV, muons behave like minimum ionizing particles (they lose ~ 2 MeV cm^{-1} in water) and the energy of totally contained events (starting and final points of the track inside the detector volume) can be estimated from the particle range. The threshold for this method is about 5±10 GeV for vertical tracks, depending on the vertical distance between optical modules, and about 15 GeV for more isotropic events, depending on the distance between orizontal lines. Over 100 GeV, the finite detector dimensions prevent from using the previous method. However, it is still possible to estimate the minimum energy by means of a measure of the contained range, useful for partially contained events. For energies greater than 1 TeV, due to stochastic processes like bremstrahlung, couple production or dominant δ rays, the muon energy losses become proportional to the energy itself. The muon range increases logarithmically with energy (fig. 4.15).

On the other hand, the detection efficiency increases with energy due to the additional energy loss. Above 1 PeV, the Earth becomes opaque to up-going vertical neutrinos. Nevertheless, neutrinos with such a high energy or more, can be detected if they come from a small angle above the horizon. High energy τ neutrinos can be observed since the produced τ leptons decay before being absorbed, giving rise to low energy ν_τ which proceed in the same direction of the original ν_τ. In this way, the interacting probability reduces, causing an increase in the number of events at the maximum detectable energies.

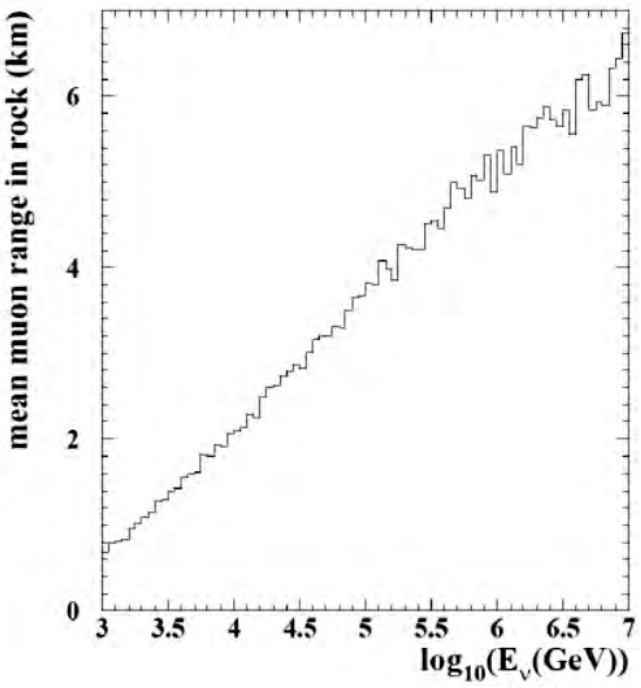

Figure 4.15: Muon range in rock as a function of the neutrino energy.

4.5 Detector

ANTARES is at present the largest neutrino observatory in the Northern hemisphere, which provides a privileged sight of the most interesting areas of the sky like the galactic centre, where many neutrino source candidates are expected. It is located in the Mediterranean Sea, 40 km off the Touolon coast (South France), at a depth of 2400 m. Thanks to the rotation of the Earth, this location (42° 50'N, 6° 10'E) has an efficient sky coverage of about 3.5π sr. To detect the Cherenkov light, the neutrino telescope comprises a matrix of light detectors, in the form of photomultipliers contained in glass spheres, called Optical Modules (OM), positioned on flexible lines anchored to the seabed. The muon track is reconstructed using the measurements of the arrival times of the Cherenkov photons on the OMs of known positions. In the following, a description of the detector is reported. For further deltails see [24].

4.5.1 Layout

The basic detection element is the optical module (OM) housing a photomultiplier tube (PMT). The nodes of the three-dimensional telescope matrix are called storeys. Each storey is the assembly of a mechanical structure, the Optical Module Frame (OMF), which supports three OMs, looking down-wards at 45° , and a titanium container, the Local Control Module (LCM), housing the offshore electronics and embedded processors. In its nominal configuration, a detector line is formed by a chain of 25 OMFs linked with Electro-Mechanical

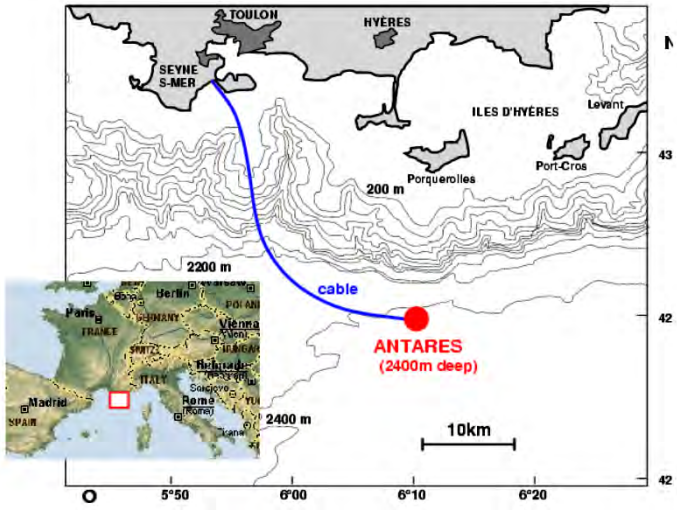

Figure 4.16: ANTARES site in the Mediterranean Sea. On the vertical (horizontal) axis the terrestrial latitude (longitude) is shown.

Cable segments (EMC). The distance is 14.5 m between storeys and 100m from the seabed to the first storey. The line is anchored on the seabed with the Bottom String Socket (BSS) and is held vertical by a buoy at the top. The full neutrino telescope comprises 12 lines, 11 with the nominal configuration, the twelfth line being equipped with 20 storeys and completed by devices dedicated to acoustic detection. Thus, the total number of the OMs installed in the detector is 885. The lines are arranged on the seabed in an octagonal configuration and is illustrated in Fig. 4.17. It is completed by the Instrumentation Line (IL07) which supports the instruments used to perform environmental measurements. The data communication and the power distribution to the lines are done via an infrastructure on the seabed which consists of Inter Link cables (IL), the Junction Box (JB) and the Main Electro-Optical Cable (MEOC).

4.5.2 Line Structure

A line is the assembly of an anchor sitting on the seabed, 25 storeys and a top buoy linked by electro-optical mechanical cables. A storey consists of three optical modules, the metal structure that supports them and provides interfaces with the EMCs, the electronics container and additional instrumentation. In order to limit the number of single point failures for a full line, a line is divided in 5 sectors of 5 successive storeys each. The sectors are independent for the power distribution and the data transmission. The distribution of power and routing of clock and acquisition signals toward each sector are performed in electronics containers fixed on the BSS.

Optical modules

The optical module, the basic sensor element of the telescope, is the assembly of a pressure resistant glass sphere housing a photomultiplier tube, its base and

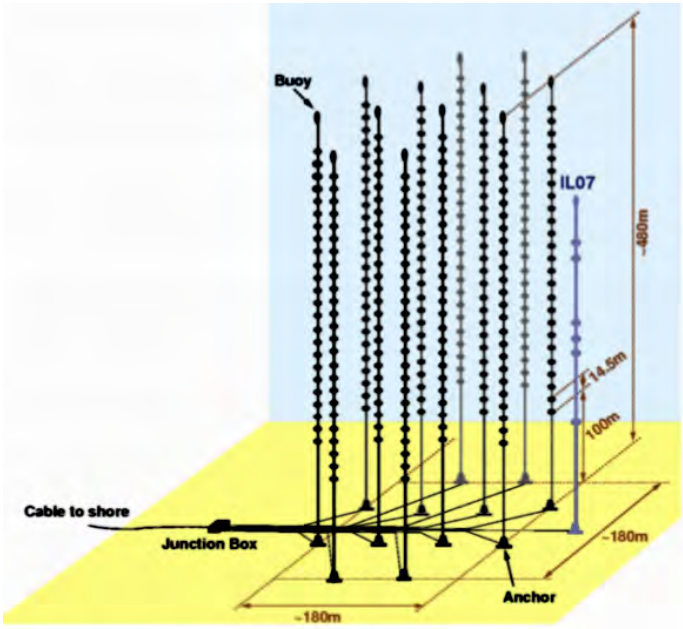

Figure 4.17: Schematic view of the ANTARES detector.

other components. A detailed description of the ANTARES OM can be found in [22]. The search for a highly sensitive light detector led to the choice of photomultiplier tubes with a photocathode area as large as possible combined with a large angular acceptance. Regarding these criteria, the best candidates are large hemispherical tubes. However, the PMT size is limited by some characteristics which increase with the photocathode area: the transit time spread (TTS) which has to be small enough to ensure the required time resolution and the dark count rate which must be negligible compared to photon background rate. Fig. 4.18 shows a schematic view of an optical module with its main components. The following sections describe the different components.

Photomultiplier tube An extensive series of tests were performed on several commercially available models of large hemispherical photomultipliers. A summary of this study is presented in [23]. The R7081-20, a 10" hemispherical tube from Hamamatsu 12 [1] , was chosen. The full sample of delivered PMTs has been tested with a dedicated test bench in order to calibrate the sensors and to check the compliance with the specifications. The number of rejected tubes was small (17, their peak/valley ratio being too low), these tubes were replaced by the manufacturer. During the testing process, the working point of each PMT, i.e. the high voltage needed to obtain a gain of $5 \times 10^7 \pm 10$ %, was determined by measuring the value of the SPE pulse height. The results of these measurements are illustrated in fig. 4.19.

Glass Sphere The protective envelope of the PMT is a glass sphere of a type routinely used by sea scientists for buoyancy and for instrument housing. These

[1] Hamamatsu Photonics, Electron tube division, http://www.hamamatsu.com

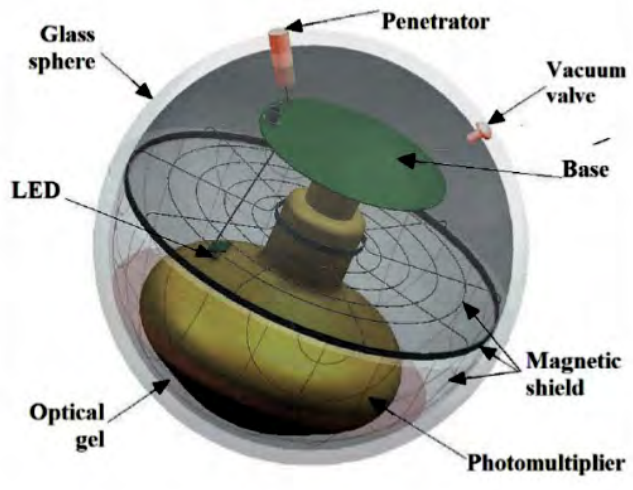

Figure 4.18: Schematic view of an ANTARES optical module

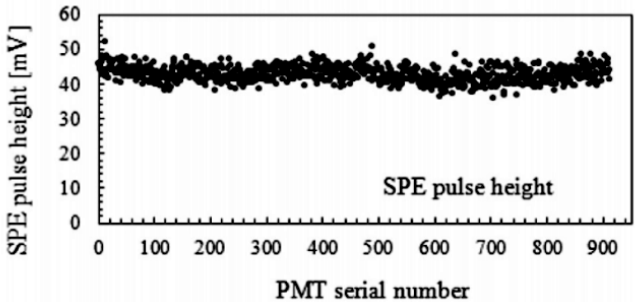

Figure 4.19: Measured mean pulse height of single photoelectrons for each PMT at nominal gain

spheres, because of their mechanical resistance to a compressive stress and of their transparency, provide a convenient housing for the photodetectors.The sphere is provided as two hemispheres: one, referred to as "back hemisphere" is painted black on its internal surface and the other, "front hemisphere" is transparent. The front hemisphere houses the PMT and the magnetic shielding held in place by the optical gel. The back hemisphere has two drilled holes to accommodate the electrical connection via a penetrator and a vacuum port. Around both holes a flat surface is machined on the outside of the sphere for the contact of the single O-ring ensuring water tightness. The back hemisphere is also equipped with a manometer readable from the outside. The two glass halves have precisely machined flat equatorial surfaces in direct contact (glass/glass) without any gasket or interface.

Optical Gel The optical coupling between the glass sphere and the PMT is achieved with optical gel. The chosen gel is a two-component silicon rubber.

The optical gel has an elastic consistency soft enough to absorb the sphere diameter reduction by the deep sea pressure (1.2 mm) and stiff enough to hold the PMT in position in the sphere. The optical properties of the gel have been measured in the laboratory: the absorption length is 60 cm and the refractive index is 1.404 for wavelengths in the blue domain.

Magnetic shield At the ANTARES site, the Earth's magnetic field has a magnitude of approximately 46 μT and points downward at 31.5° from the vertical. Un-corrected, the effect of this field would be a significant degradation of the transit time spread (TTS), of the collection efficiency and of the charge amplification of the PMT. A magnetic shield is implemented by surrounding the bulb of the PMT with a hemispherical grid made of wires of $\mu-$metal [2] closed by a flat grid on the rear of the bulb. This provides a magnetic shielding for the collection space and for the first stages of the amplification cascade. The efficiency of the screening becomes larger as the size of the mesh is reduced and/or the wire diameter is increased, however the drawback is a shadowing effect on the photocathode. The compromise adopted by the ANTARES Collaboration, a mesh of 68×68 mm^2 and wire diameter of 1.08 mm, results in a shadowing of less than 4 % of the photocathode area while reducing the magnetic field by a factor of three. Measurements performed in the laboratory show that this shielding provides a reduction of 0.5 ns on the TTS and a 7 % increase on the collected charge with respect to a naked, uniformly illuminated PMT.

HV power supply To limit the power consumption the PMT power supply has two independent high-voltage chains. The first chain produces a constant focusing voltage (800 V) to be applied between photocathode and first dynode. The second chain gives the amplification voltage, which can be adjusted from 400 V to 1600 V by an external DC voltage. The HV generator is powered by a 48 V DC power supply and has a typical consumption of 300 mW.

Internal LED On the rear part of the bulb of the PMT, a blue LED is glued in such a way to illuminate the pole of the photocathode through the aluminium coating, which acts as a filter of large optical density (optical density ~ 5). This LED is excited by an externally driven pulser circuit and is used to monitor the internal timing of the OM.

Link with the electronics container The electrical connection of the OM to the electronics container is made with a penetrator [3]. The associated cable contains shielded twisted pairs for the transmission of power, the control of the LED pulser and the setting and monitoring of the DC command voltage of the PMT base.

Storey

The OMs are grouped in triplets to form a storey or floor (fig. 4.20). They are mounted at equidistant angles around a titanium Optical Module Frame (OMF), and point downwards at 45° with respect to the vertical. The OMs are

[2] Sprint Metal, Ugitech, http://www.ugitech.com
[3] EurOc'eanique S.A., http://www.macartney.com part

connected to the Local Control Module (LCM): the titanium cylinder at the center of the OMF that houses the data transmission electronics of the OMs, as well as various instrumentsfor calibration and monitoring. A storey may also contain extra instruments that are mounted on the OMF, such as a LED beacon or an acoustic hydrophone. Storeys are serially connected with Electro-Mechanical Cables (EMCs), which contain electrical wires for power distribution and optical fibres for data transmission. The distance between adjacent storeys is 14.5 m. Five storeys linked together constitute a sector: an individual unit in terms of power supply and data transmission. In each sector, one of the five LCMs is a Master LCM (MLCM). The data distribution between all LCMs in the sector and the String Control Module is handled by the MLCM. Five sectors linked together form an individual detector line. Each line is anchored to the seabed by a Bottom String Socket (BSS) and kept vertical by a buoy at the top of the line and by the buoyancy of the individual OMs. A string is 480 m long, since roughly 100 m from the seabed are left empty to allow for the development of the Cherenkov cone for upward going particles. The BSS contains a String Control Module (SCM), a String Power Module (SPM), calibration instruments and an acoustic release system. The acoustic release allows for the recovery of the complete detector line including BSS except for a dead-weight. The SPM houses the individual power supplies for all five sectors in the line. The SCM contains data transmission electronics to distribute data between each sector and the onshore control room. The average horizontal distance between lines is approximately 60 m. The BSS of each line is connected to the Junction Box (JB), which is the distribution point of power and data between the detector lines and the 40 km long Main Electro-Optical Cable (MEOC) to the onshore control room in La Seyne-sur-Mer.

4.5.3 Data Acquisition System

The main purpose of the data acquisition (DAQ) [28] system is to convert the analogue signals from the PMTs into a format suitable for the physics analysis. To achieve this, the DAQ system has the task to prepare the detector for data taking, convert the analogue signals from the PMTs into digital data, transport the data to shore, filter the different physics signals from the background, store the filtered data on disk, and archive the run settings.

4.5.4 Signal Digitization

When a photon hits the photo-cathode of a PMT, an electron can be liberated with a probability to induce an electric signal on the anode of the PMT given by the PMT's quantum efficiency. The electron, referred to as a photo-electron (p.e.), induces an amplified electrical signal on the anode of the PMT. If the amplitude of this analogue signal crosses a certain voltage threshold, the signal is digitised by a front-end chip called analogue ring sampler (ARS) [29] that is located in the LCM. The threshold allows to exclude small signals due to the dark current in the PMT. Its value is typically the equivalence of 1/3 of the analogue signal collected on the anode for a single p.e. arriving at the first dinode (L0 hits). When the threshold is crossed, the ARS chip assigns a time stamp to the PMT signal. Timing information is provided by a local clock system in the LCM that is synchronised with a 20 MHz master clock situated on shore.

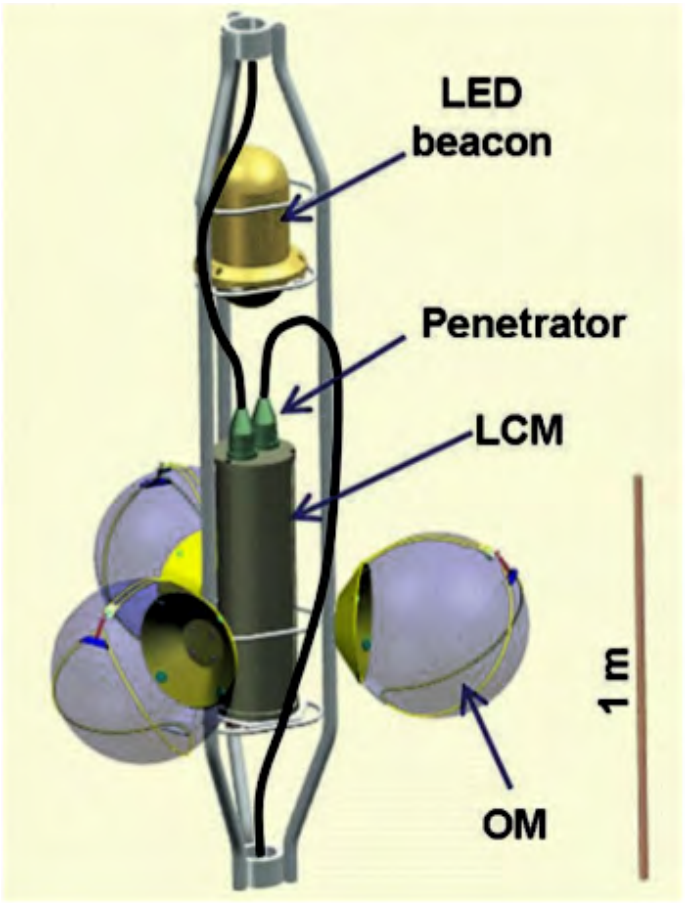

Figure 4.20: OMF equipped with the 3 OMs, the LCM and an LED beacon. The mechanical parts used for fixing cables toward the upper and the lower storeys are omitted.

The ARS counts the number of clock pulses for a rather coarse timing (units of 25 ns), and uses a time-to-voltage converter (TVC) to interpolate between two subsequent clock pulses to achieve a more precise timing with an accuracy of about 0.2 ns. The ARS measures the charge contained in the PMT signal by integrating the anode current over a certain time interval, which is typically 25 ns. The integrated charge is related to the amount of photo-electrons in the signal, and so a measure for the intensity of the instantaneous radiation on the PMT. After digitisation of a signal, the ARS is inactive for a period of approximately 250 ns. In order to reduce the effect of this dead time on the data taking, each PMT is read out by two ARS chips which alternately process the PMT signals. The combined digital information on the time and charge of a PMT signal is referred to as a "*hit*". The read-out of the ARS chips is then performed by a field programmable gate array (FPGA). The FPGA arranges the *hits* from each ARS in the LCM into so-called *data frames* each of whom contains all the hits produced by a specific ARS within a predefined time

interval of typically 13 ms. Data frames are then organized in 64 MB buffers (SDRAM, *Synchronous Dynamic Random Access Memory*) and sent as separate data packages to shore via the MLCM (Master LCM).

4.5.5 Data Transmission

Each LCM contains a Central Processing Unit (CPU) which is connected to the onshore computer system. Each CPU runs two programs that manage the data transfer to shore: the *DaqHarness* and the *ScHarness*. The latter handles the transfer of dataframes from the SDRAM to the onshore control room; the former handles the transfer of calibration and monitoring data, referred to as slow control data. Communication between all offshore CPUs and the onshore control room is done via optical fibers using the Transmission Control Protocol and Internet Protocol (TCP/IP). Each LCM CPU in a sector is connected via a bi-directional Fast Ethernet link (100 Mb/s) and an electro-optical converter to the MLCM. In the MLCM, these links are electro-optically converted and passed to an electronic data router (switch). The switch merges the 5 bi-directional Fast Ethernet links (4 LCM and 1 MLCM CPU) into two uni-directional Gigabit Ethernet links (1 Gb/s), one for incoming control signals and one for outgoing data. The gigabit signals are electro-optically converted using an optical wavelength which is unique for each MLCM in a detector line. The incoming and outgoing optical links of the 5 MLCMs in a detector line are routed to the String Control Module, where they are (de)multiplexed into a single optical fiber using Dense Wavelength-Division Multiplexing (DWDM). The optical fiber from each String Control Module runs through the Junction Box and the Main Electro-Optical Cable to the onshore control room, where they are (de)multiplexed into separate MLCM channels using the same wavelengths as in a detector line. The unidirectional optical MLCM channels from all demultiplexers are linked to an onshore switch via electro-optical converters. Finally, the switch is connected to a computer farm which accommodates the detector control and the data processing systems. Fig. 4.21 shows an illustration of the data flux along a single instrumented line.

4.5.6 Data filtering and storage

The DAQ system is designed according to the so-called All-Data-To-Shore concept that means that no offshore signal selection is done except for the ARS threshold criterion, and all detected hits are transferred to shore. However, the vast majority of detected signals is due to the optical background in the detector. Therefore, the data are filtered in the onshore computing farm to reduce the data storage demands. This is obtained by sending all dataframes that belong to the same time window to a common processor in the onshore computer farm. The complete set of dataframes from all ARS chips in the detector that correspond to the same time window, referred to as a timeslice, contains all hits that were detected in the same time window. Each timeslice is handled by a different processor, each of which accommodates a *dfilter* program. The *dfilter* program collects all dataframes corresponding to the same timeslice, and applies a trigger algorithm to search for signals that can be attributed to a charged particle which traversed the detector (see below). The trigger algorithm [30] searches for hits which are causally connected and/or have a sufficiently large amplitude

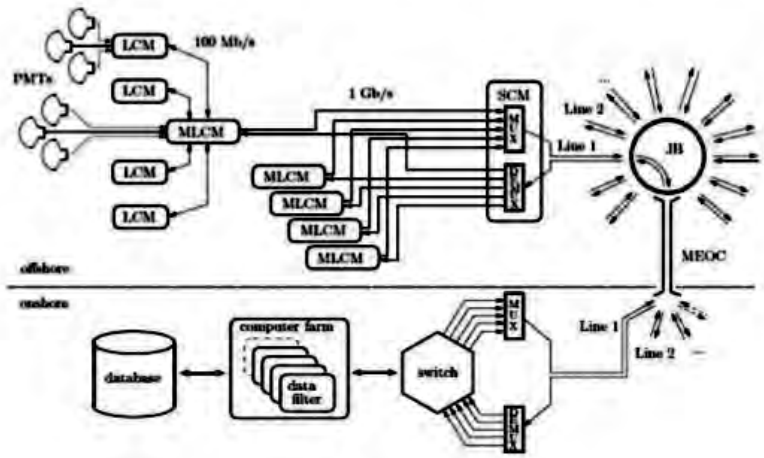

Figure 4.21: Data flux along a single instrumented line.

(see 4.5.7). When the trigger conditions are fulfilled, a so-called physics event is built. Using software rather than hardware to filter data has advantages in terms of flexibility and detection sensitivity. Different trigger algorithms can be applied in parallel to search for specific signatures. The output from every datafilter is passed to the *dwriter* program that formats the data using the ROOT software package (http://root.cern.ch) and stores them in a database for offline analysis. Similarly, the slow control data are collected and processed by the *scDataPolling* program, and written to the database by the *dbwriter* program.

4.5.7 Triggers

The trigger conditions define a L0 hit as a hit with amplitude larger than 0.3 p.e. An L1 hit is defined either as 2 L0 hits in coincidence within 20 ns in two OMs of the same storey or as a single L0 hit with an amplitude larger than 3 p.e. The most common applied selection criteria are referred to as 3D-SCAN Trigger (shortened as 3N) and/or 2T3 Trigger (shortened as T3). The 3N Trigger requires at least 5 causally connected L1 hits. A 1T3 cluster is defined as 2 L1 hits in adjacent or next-to-adjacent storeys, in coincidence within 100 ns or 200 ns, respectively. The T3 trigger seeks for time coincidence between two 1T3 clusters, in the whole detector, within 2.2 μs. These two 1T3 clusters can be located on the same detector line or on different lines. In the former case, 3 L1 hits on three adjacent storeys can lead to a triggered event. An offline code (TriggerEfficiency [31]) is dedicated to the treatment of MonteCarlo events. It adds the background hits due to 40 K and bioluminescence (4.2) and applies the same trigger criteria defined in the online trigger, to select candidate events in the MonteCarlo samples. The background added to MonteCarlo samples is taken from data to reproduce the real acquisition conditions such as the

number of active OMs, low efficiency PMTs, baseline rate and bursts due to bioluminescence. The MonteCarlo simulation tools will be described in details in sec. 4.5.9.

4.5.8 Detector Calibration

Since the precision with which the direction and energy of charged particles which traverse the detector can be determined, depends on the accuracy with which the photon arrival times at the PMTs and the location of those PMTs are measured, the ANTARES detector comprises several independent calibration systems that are able to measure and monitor the absolute and relative timing of PMT signals and the location of all PMTs.

- Time Calibration: a calibration signal, sent by the onshore master clock, is echoed back along the same optical path by each LCM, to measure the relative offset of each LCM with an accuracy of 0.1 ns. Moreover, a second calibration system based on a blue (470 nm) LED inside each OM is used to calibrate the time offset between the PMT photo-cathode up to the read-out electronics.

- Position Calibration: a real time positioning of each line is needed due to the sea current and the flexibility of the Electro-Mechanical Cables that make the radial displacement of a detector line considerable. This is achieved through two independent systems: an acoustic positioning system and a tiltmeter-compass system. The former consists of a three-dimensional array of acoustic emitters, capable of sending high frequency (40 – 60 kHz) acoustic signals, located on the BSS of each line, and receivers (hydrophones). Five hydrophones are located on Storeys 1, 8, 14, 20 and 25 of each detector line. Dedicated acoustic runs are performed every 2 minutes, during which the transit times between each emitter and the receivers are recorded. The distances between emitters and receivers are calculated using the sound velocity which is monitored by several sound velocity profilers located throughout the detector. The calculated distances are then used to triangulate the position of each acoustic receiver relative to the acoustic emitters with an accuracy of 10 cm [38]. The tiltmeter-compass system comprises a tiltmeter and a compass in each LCM. The two perpendicular tilt angles of a storey, the pitch and roll angles along the North-South and East-West axes, are monitored by a tiltmeter with an accuracy of 0.2° . The heading angle of a storey with respect to the North-South axis is monitored with a compass with an accuracy of 1°. The tiltmeter-compass data are also read out every 2 minutes.

4.5.9 MonteCarlo simulation

In the following an overview of the simulation chain and the software packages used to generate the neutrino and muon events in the detector is presented. The standard ANTARES simulation tools are used for the generation of muons and neutrinos, the propagation of muons and other secondary particles towards and through the detector along with photon emission and propagation, and finally the simulation of the optical modules' response. The simulation corresponds to

the best available description of the true data taking conditions since information about the rates, the condition of the optical modules and the run duration from the corresponding data runs are used in order to achieve a realistic run-by-run simulation of the physics and data taking process [32].

- The first step in the simulation chain is to generate a flux of neutrino events in the vicinity of the detector, that have a chance of producing a detectable muon signal by means of the GENHEN package ([33]). Neutrino events are generated isotropically inside a large cylinder around the detector, whose size is determined in such a way so that all neutrinos that are able to produce a detectable muon inside the detector will be simulated, and it is based on the maximum range that a muon can travel. A muon can be detected if it reaches the can, defined as the area surrounding the ANTARES instrumented volume extending typically up to $2-3$ light attenuation lengths away. Muons outside the can are too far away to produce detectable light, so only the propagation of particles from their generation point to the can is simulated and not the photon emission and development of electromagnetic and hadronic showers.

- The propagation of the muon from the neutrino interaction vertex to the can is simulated with the MUSIC package ([34]). The energy losses of the muon as well as the changes on its direction due to multiple Coulomb scattering are included in the simulation.

- The charged current neutrino interactions are simulated with the LEPTO package ([37]).

- The atmospheric muon background is simulated with the HEMAS code which generates the isotropic flux of primary cosmic rays and the evolution of the showers in the atmosphere. The MUPAGE ([35]) package takes as input the HEMAS output and simulates the propagation of the muons produced after the interaction of cosmic rays in the atmosphere. Only for those events which arrive at the sea level with an energy greater than 500 GeV, the propagation up to the can is simulated with MUSIC.

- The muon propagation inside the can and the light that reaches the optical modules is simulated with the KM3 package ([36]).

- Finally, the simulation of the electronics response such as the charge integration and the dead time is performed with the TriggerEfficiency program ([31]). In this step optical background hits are added and the online triggers used in real data are simulated. Optical background hits are generated according to a Poisson distribution based on real measured rates in order to reproduce the specific run's data taking conditions. Signal as well as background hits are generated after simulating the electronics response such as the charge threshold, time integration and dead time. The trigger logics that were used during the corresponding data run are finally applied.

Chapter 5

Analysis

As shown in section 3.3, several experiments have observed a large scale anisotropy with an amplitude of the order of $\sim 10^{-3}$ in the arrival direction of primary cosmic rays in the energy range between 1 and 100 TeV. The aim of this work is to search for such an anisotropy by analysing three years of data collected by the ANTARES neutrino telescope. As argued before, although ANTARES is optimized for upward-going particle detection, the most abundant data sample is due to the atmospheric down-going muons produced in air showers induced by interactions of primary cosmic-rays in the Earth's atmosphere. These muons represent a high statistic data set that can provide information about primary cosmic rays incoming direction at energies above few TeV. Indeed, supposing that high energy muons preserve the arrival direction of the primary CRs, the observation of an anisotropy in the muons flux would indicate the same anisotropy in the cosmic rays distributions.

In this section each step of the analysis will be described: the analysed sample, the selection criteria applied to runs and events, and the comparison between data and Montecarlo.

The analysis method is based on data and MC distributions separately corrected for spacial and temporal asymmetries caused by the strings configuration and the uneven sky coverage. Moreover, the result of a study of a possible correlation between the muon flux and the atmospheric temperature which may cause an apparent anisotropy is presented. After the applied corrections, the obtained distributions are reported together with the study of the anisotropy profiles for data and MC, which are finally compared.

5.1 Run Selection

The data used for this analysis were collected during the period January 2009 to December 2011 with a 12-line detector configuration. There are various quantities that characterize the quality of the data taking conditions, such as the percentage of active optical modules during a run or the hit rates. The quality of data in ANTARES experiment can be affected, from time to time, by the "bioluminescence" produced by microorganisms in the sea water. This bioluminescence is registered by the PMTs as an "optical background". In ANTARES this background can increase the average rate of the PMTs and

also produce bursts of hits. The "baseline" of a run is defined as the mean of a gaussian fit on the L0 rate (4.5.7) of each PMT, averaged over all PMTs. The percentage of TimeSlices with a rate higher than the baseline plus 20%, averaged over all PMTs, gives the burst fraction. The mean rate is the average rate over all ARS's that measured more than 10 kHz. Quality Basic (QB) is a flag that characterizes the quality of the data taking conditions, based on optical background and detector state information. It is defined as follows:

- QB = 1 : Basic selection of runs available for physics analyses;
- QB = 2 : At least 80% of the OMs that are expected to work are active;
- QB = 3 : Baseline $\leq$ 120 kHz and burst fraction $\leq$ 0.4;
- QB = 4 : Baseline $\leq$ 120 kHz and burst fraction $\leq$ 0.2.

These run sets are cumulative, i.e. runs that satisfy QB=3, satisfy QB=2 as well. All runs from the database with **QB** $\geq$ **1** have been chosen for the final data sample. Additionally, calibration runs and runs that were used for tests have been excluded from the analysis by means of the cut **SCAN Flag** $\neq$ **1** which select only Physics runs. Fig. 5.1 shows a part of the list of runs collected on January 1, 2010. Only runs labelled with SETUP "Line 1-12 Physics..." represent Physics runs and can be used for the analysis.

RUN	SETUP	DATE	DURATION	COMMENT
45539	IL-07-Amadeus Test: G10 DS2 R0 noStatstimer	1-1-2010 00:53:58	2h 0m 6s	RunControl started new run automatically
45540	Line 1-12 Physics Trigger 3N+2T3+GC+T2+TQ+K40 2009V3.1	1-1-2010 02:25:51	2h 25m 31s	RunControl started new run automatically
45541	IL-07-Amadeus Test: G10 DS2 R0 noStatstimer	1-1-2010 02:55:18	3h 0m 47s	RunControl started new run automatically
45542	Line 1-12 Physics Trigger 3N+2T3+GC+T2+TQ+K40 2009V3.1	1-1-2010 04:52:18	2h 36m 0s	RunControl started new run automatically
45543	IL-07-Amadeus Test: G10 DS2 R0 noStatstimer	1-1-2010 05:56:40	3h 1m 39s	RunControl started new run automatically
45544	Line 1-12 Physics Trigger 3N+2T3+GC+T2+TQ+K40 2009V3.1	1-1-2010 07:29:26	2h 37m 18s	RunControl started new run automatically
45545	IL-07-Amadeus Test: G10 DS2 R0 noStatstimer	1-1-2010 08:58:55	3h 1m 3s	RunControl started new run automatically
45546	Line 1-12 Physics Trigger 3N+2T3+GC+T2+TQ+K40 2009V3.1	1-1-2010 10:07:55	2h 34m 12s	RunControl started new run automatically
45547	IL-07-Amadeus Test: G10 DS2 R0 noStatstimer	1-1-2010 12:01:07	3h 0m 52s	RunControl started new run automatically
45548	Line 1-12 Physics Trigger 3N+2T3+GC+T2+TQ+K40 2009V3.1	1-1-2010 12:43:14	2h 30m 34s	RunControl started new run automatically
45549	IL-07-Amadeus Test: G10 DS2 R0 noStatstimer	1-1-2010 15:02:41	0m 45s	RunControl started new run automatically
45550	IL-07-Amadeus Test: G10 DS2 R0 noStatstimer	1-1-2010 15:04:37	3h 0m 45s	recovered clock

Figure 5.1: Partial list of runs collected on January 1, 2010. Only runs labelled with SETUP "Line 1-12 Physics..." represent Physics runs.

5.2 Event Selection

The goal of the event selection is to obtain a muon candidate sample with the following characteristics:

- well reconstructed tracks;
- efficiency as large as possible in order to keep statistics high.

The first choice was satisfied by reconstructing the tracks with the **AA-Fit strategy** (4.3.2). This choice is justified by the better angular resolution that characterizes the AA-Fit algorithm compared to BB-Fit. Moreover, the following cuts have been applied in order to keep only events that are *suitable* for the analysis:

- **3D_SCAN** and **T3** triggers present (4.5.7);
- $\boldsymbol{\theta < 78°}$: this cut on the zenith angle ensures that only down-going events are kept. At first a less stringent cut was applied ($\theta \leq 85°$) where the value of the maximum zenith angle was chosen in order to have a good agreement with Montecarlo events since they are generated with $\theta \leq 85°$. The value was then changed in order to ensure that the muon angular distributions were not affected by the presence of the coast in the nearby of the detector. Indeed, muons coming from the Zenith angular range $80° \lesssim \theta \lesssim 90°$ (see fig. 5.2) in the Azimuth range $60° \lesssim \phi \lesssim 132°$ could have a non isotropic distribution due to the presence of the coast on one side.

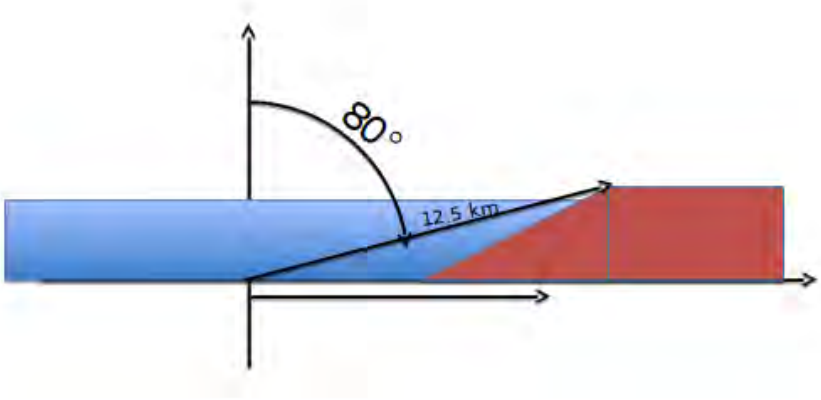

Figure 5.2: Illustration of the position of the coast with respect to the ANTARES detector. The mountain occupies a Zenith range between 80° and 90°.

- **number of lines > 1**: only events reconstructed with more than one line have been kept since the cylindrical simmetry of the line prevents from obtaining a good reconstruction on the azimuth angle for the *single-line* events;
- **E>1 TeV**: this cut on the reconstructed energy rejects low energy events which are more likely to have a worst reconstructed track and thus direction and retains events in the energy range in which the anisotropy has been observed (3.3).

5.3 Data - Montecarlo comparison

The MonteCarlo sample of events used in this analysis has been obtained with a run-by-run simulation: using the measured optical background rates, OM conditions and run duration, a realistic simulation of the physics and data taking process for each run is obtained (4.5.9). The comparison between data and simulations is an important step for this analysis. A good agreement between data and MC not only represents a hint of good understanding of the physics processes and detector response of the experiment, but also it constitutes a necessary condition to investigate the presence of a possible anisotropy in the arrival distribution of data events compared to those isotropically simulated. Therefore, the first aim of the analysis is to identify the necessary cuts which provide a good agreement between data and MC distributions.

Fig. 5.3 shows the distribution of the two quality parameters of the AA-Fit strategy, Λ and β, after applying the previous cuts, for both data (red) end MonteCarlo (blue) events. The MC distributions have been weighted with a constant value $w = 3$ since the number of simulated atmospheric muons is one third of the data events.

The excess of data compared to the MonteCarlo at the lowest value of Λ is due to the non-simulated contribution of events consisting of solely optical background. This configuration of hits, that can fulfill the online trigger, is not simulated in the MC. The overall lack of MC events compared to the number of data (the MC sample is $\sim 81\%$ of the data sample) is due to the fact that the characteristics of the detector undergo seasonal and weekly variations which directly affect the run-by-run production of simulated events. Therefore, the common weight $w = 3$ has to be substituted with a new weight derived from weekly distributions, as described later in this section.

The following conditions on Λ and β have been imposed:

- $\boldsymbol{\Lambda > -6.2}$
- $\beta < \mathbf{1}^\circ$

For the sample of events selected by these cuts, the agreement between data and simulations is good. Both cuts are aimed at the rejection of the worst reconstructed tracks but ensuring not to reduce excessively the final data sample: in this way, $\sim 34\%$ of data and $\sim 37\%$ of MC events are kept. A more stringent condition on the β angle is not necessary since we are looking for large scale anisotropy and an angular resolution better than 1° is not required.

After those cuts have been applied, it is possibile to proceed with the comparison of data and MC for both the reconstructed azimuth and zenith angles. Fig. 5.4 shows the obtained distributions.

The first evident feature is that neither the azimuth distribution nor the $\cos(\theta)$ one is uniform as they are expected to be at the entrance of the atmosphere if the flux is isotropic. This effect is due to the non-symmetrical form of the detector and has to be corrected as it will be described in the next section. Neither of the two distributions shows a good agreement between data and MC. This is partially due to a not correct weight associated to the MC events, as argued before. The cuts on Λ and β have reduced the difference between the amount of real and simulated events showing that it was in part caused by the presence of more misreconstructed data events compared to the

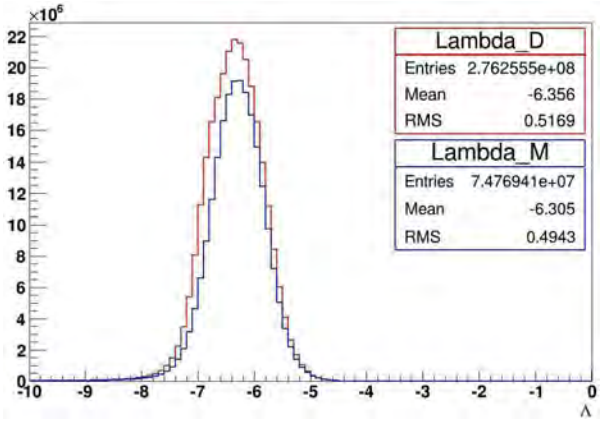

(a)

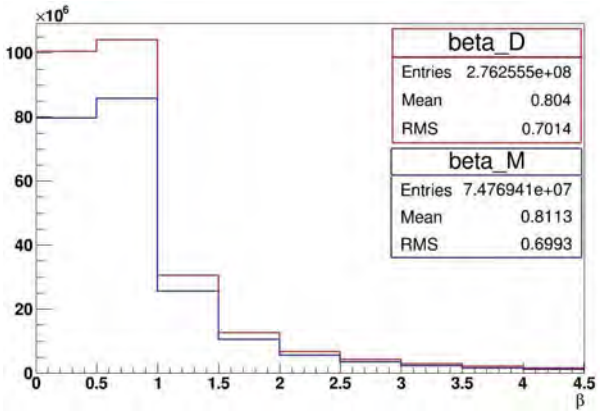

(b)

Figure 5.3: Λ (a) and β (b) distributions for data (red) and Montecarlo (blue) events.

MC ones. However, there is still a striking difference in the total number of events: the MC sample is $\sim$ 87 % of the data sample. Moreover, even if the azimuth distributions for data and MC show the same trend for different values of ϕ, the zenith distributions for data and MC are in good agreement only for values of $\theta \gtrsim 45°$, while a larger number of vertical data events compared to MC is present, suggesting that the not correct weight is not the only effect that has to be considered.

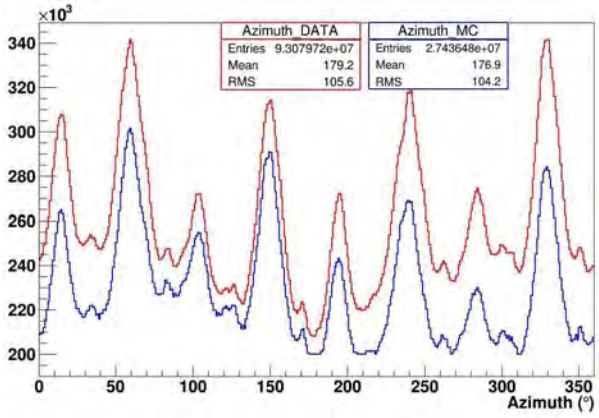

(a)

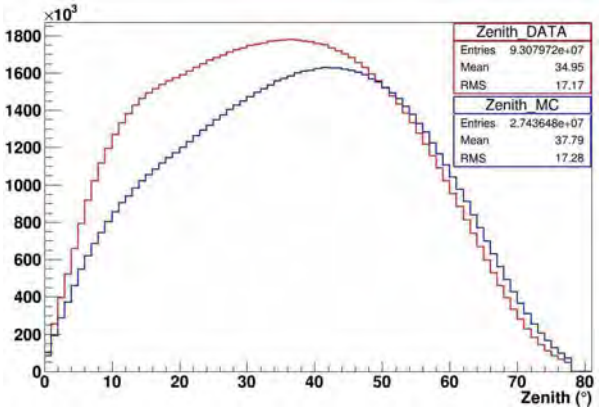

(b)

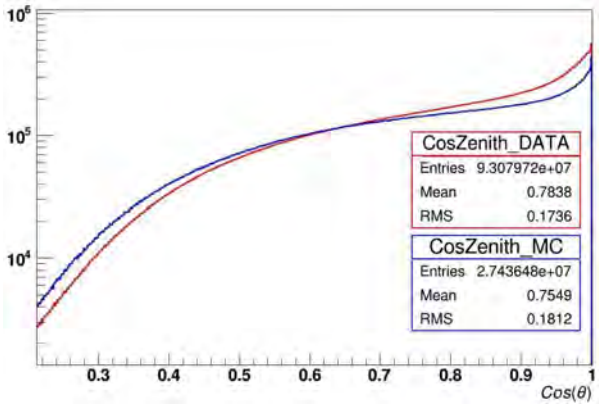

(c)

Figure 5.4: Azimuth ϕ (a), Zenith θ (b) and Cos(θ) (c) distributions for data (red) and Montecarlo (blue) events.

We found a correlation between the discrepancies in the zenith distribution of MC and data sample and the "distance of minimum approach" of the muons to the detector axis. Events characterized by a track which, at the moment of minimum approach to the can, is still far from its vertical axis, can be detected as well but a limited number of PMTs contribuites to its recostruction. Fig 5.5 shows the distribution of two variables:

- $\sqrt{(x_a - x_c)^2 + (y_a - y_c)^2}$, where x_a and y_a are the coordinates of the minimum approach point to the axis of the detector on the $x - y$ plane, while x_c and y_c are the coordinates of the center of the detector.
- $z_a - z_c$, that is the vertical distance from the center, of the point of minimum approach between the track and the vertical axis.

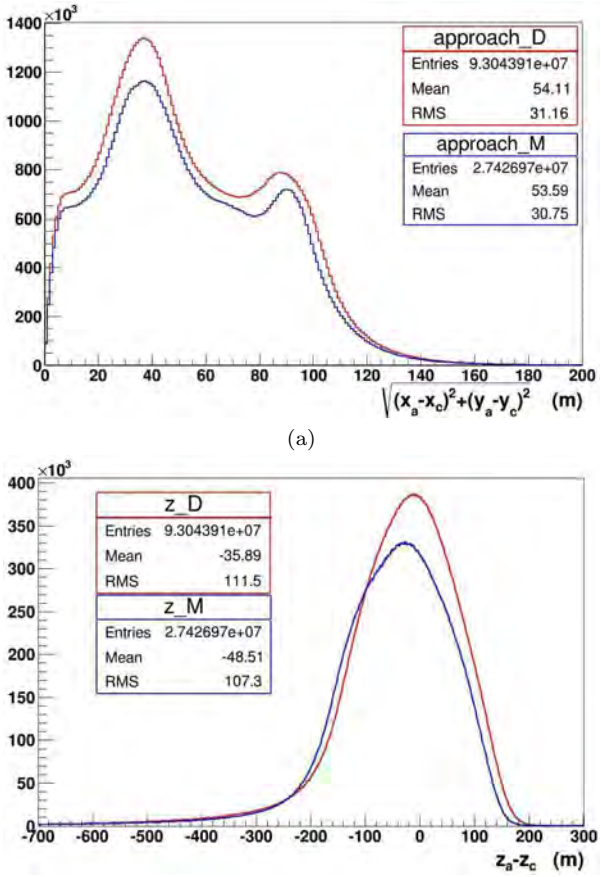

(a)

(b)

Figure 5.5: $\sqrt{(x_a - x_c)^2 + (y_a - y_c)^2}$ (a) and $z_a - z_c$ (b) distributions for data (red) and Montecarlo (blue) events.

The double-peak distribution on the $x - y$ plane can be explained by the spatial arrangement of the lines of the detector. As shown in fig. 5.6 there are two set of lines: four lines at $\sim$ 40m from the center and eight lines at $\sim$ 90m

from the center. The closer the track approaches to one of the two groups of lines, the greater is the detection probability.

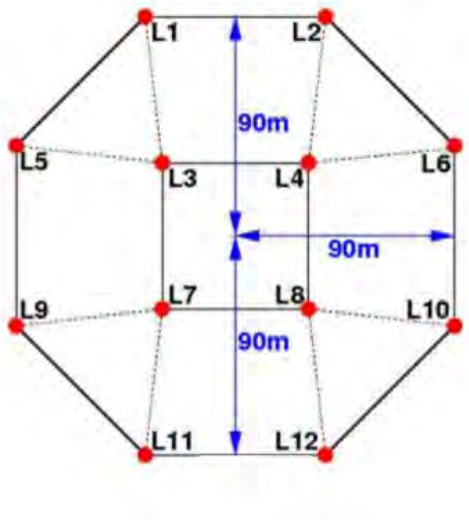

Figure 5.6: Lines arrangement in the detector.

The $z_a - z_c$ distribution is chacterized by roughly the total amount of events with a minimum approach point closer than $\sim$ 200m from the center of the detector. However, a long tail toward negative values is present.

In order to reject those events whose track closest approach to the detector is still too far, the following cuts have been applied:

- $\sqrt{(\mathbf{x_a} - \mathbf{x_c})^2 + (\mathbf{y_a} - \mathbf{y_c})^2} < \mathbf{50\ m}$
- $|\mathbf{z_a} - \mathbf{z_c}| \leq \mathbf{200\ m}$

Fig. 5.7 shows the distributions of the azimuth and zenith angles obtained after the cuts.

The agreement between data and MC is improved for both the distributions, with a difference between the two samples of the order of 10 %. However, even if the excess of data events for low zenith angles has decreased, a shift of the MC events towards horizontal zenith angles is always present. On the other hand, the azimuth curves of the two samples show the same trend and their not perfect agreement can be justified by the not correct value of w assigned to the MC events.

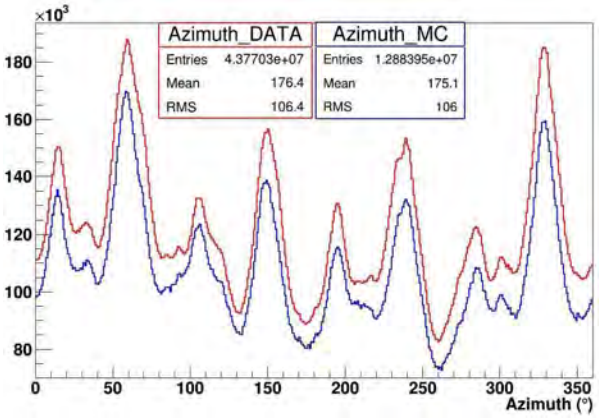

(a)

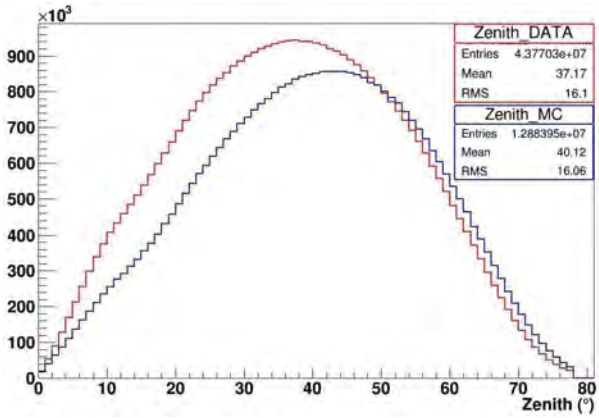

(b)

Figure 5.7: Azimuth ϕ (a) and Zenith θ (b) distributions for data (red) and Montecarlo (blue) events after the cuts on the minimum approach distances.

As an example, fig. 5.8 shows the distribution of the azimuth angle for two different weeks in the same year: (a) from 24/12/2011 to 31/12/2011 and (b) from 01/06/2011 to 08/06/2011.

It is evident that in both cases the MC trend is compatible with the data one; however, only for the first week, MC weighted with $w = 3$ give a good description of data. A new set of weights has then been found in the following way. The total sample of both data and MC has been splitted in 144 weeks. For each week, the mean value m of the distribution of the ratios between MC and data in each azimuth bin for that week has been used to define the new weight as:

$$w_{new} = \frac{3}{m} \tag{5.1}$$

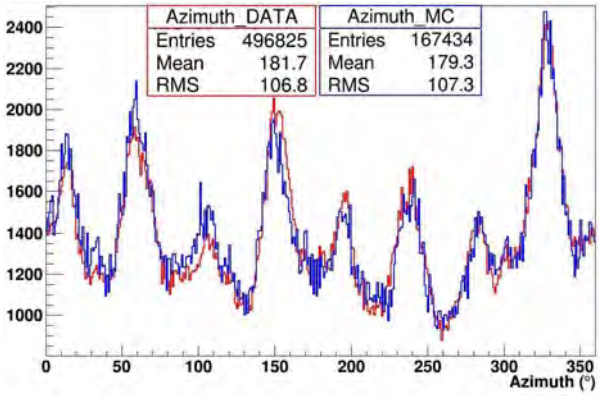

(a)

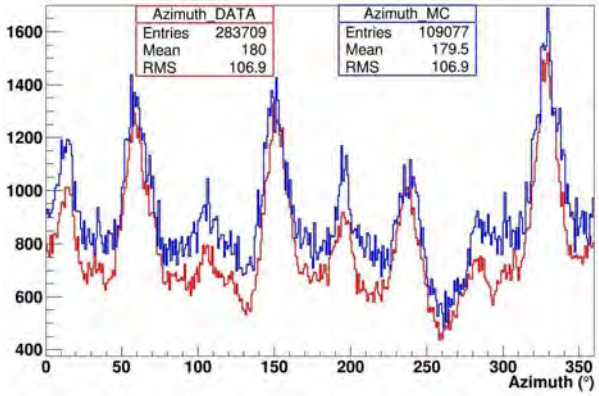

(b)

Figure 5.8: Azimuth ϕ distributions for the period 24/12/2011 - 31/12/2011 (a) and 01/06/2011 - 08/06/2011 (b) for data (red) and Montecarlo (blue) events after the cuts on the minimum approach distances.

Fig. 5.9 is an example of two distributions of ratios relative to the azimuth distributions shown in fig. 5.8.

For the two cases presented, the new weights are:

- $w^a_{new} = \frac{3}{m^a}$, $m^a = 1.015$
- $w^b_{new} = \frac{3}{m^b}$, $m^b = 1.165$

Fig. 5.10 shows the new Azimuth and Zenith distributions after the new weights have been applied to the MC events.

Both the azimuth and zenith distributions show an improved agreement between data and MC. In particular the choice of the new weights has completely solved the discrepancy in the azimuth distribution. However, even if the incongruity in the zenith distribution between data and MC has been clearly reduced, the two trends cannot be considered totally compatible. This result has influenced the further steps as explained in the following.

Due to the design and working principle of the ANTARES detector, the probability of detecting a cosmic-ray event is a strong function of its arrival

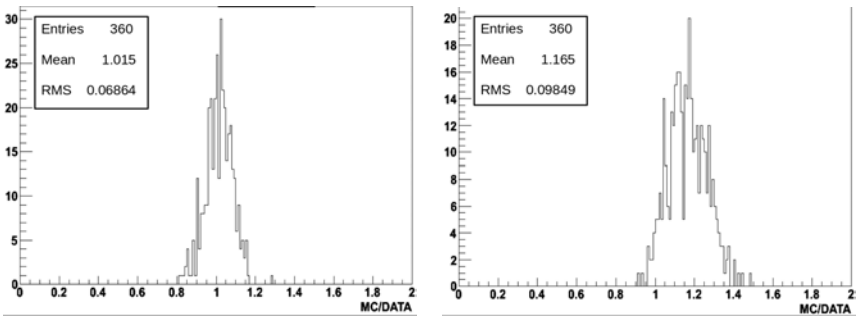

(a) (b)

Figure 5.9: Distributions of the ratios between number of MC and data events in each Azimuth bin for the period 24/12/2011 - 31/12/2011 (a) and 01/06/2011 - 08/06/2011 (b). The mean values used in eq. 5.1 are $m^a = 1.015$ and $m^b = 1.165$.

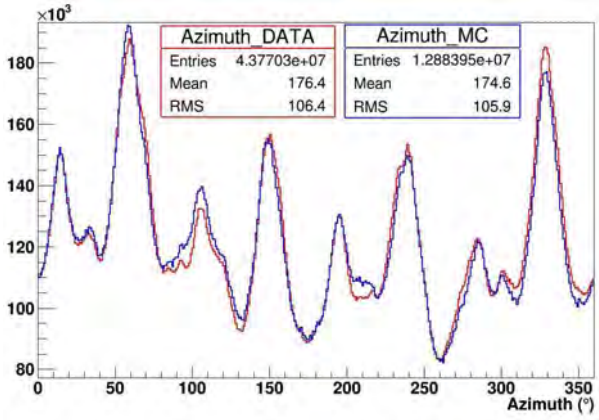

(a)

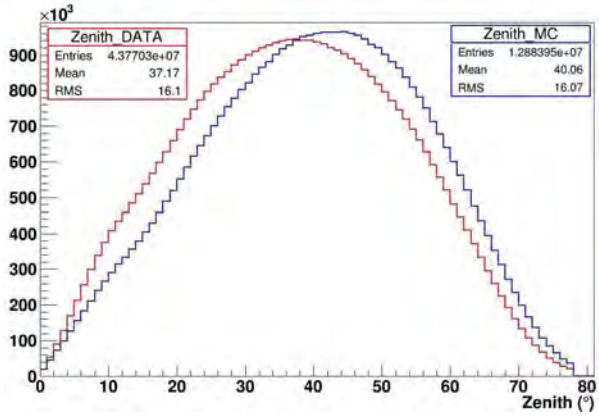

(b)

Figure 5.10: Azimuth ϕ (a) and Zenith θ (b) distributions for data (red) and Montecarlo (blue) events after the new weights have been applied.

direction. For instance, the regular arrangement of strings (fig. 5.6) creates lines of the detector along which events are preferentially detected, producing an uneven event rate as a function of local azimuth angle. Moreover, the depth of the detector also induces a strong dependence of the observed cosmic-ray rate on local zenith angle: primary vertical CRs have a bigger probability to be detected, by means of an atmospheric muon in the detector, than an horizontal CR. Therefore, it is important to find a method that would remove these detector effects and provide an unbiased estimation of the real cosmic-ray distribution in the sky. To accomplish this, an estimation of what the arrival distributions in detector coordinates would have been if the cosmic-ray flux was isotropic is desired. The response of a detector to an isotropic flux can be used as a reference to which we can compare the distribution of detected events. The ideal procedure to obtain this estimate would be to inject an isotropic flux of simulated air showers to a MonteCarlo model of the detector and then study the arrival distributions of events that pass the same trigger requirements as those in the real data. Those distributions in local coordinates would give an idea of how the design and working principle of the detector affect the isotropic flux and can be used to correct such effect. However, this is only feasible when anisotropies are large (i.e. $> 10\%$), since detector simulations are not precise at a level better than a few percent. For anisotropies with amplitudes in the $\sim 10^{-4} - 10^{-3}$ range such as those expected in the TeV-PeV energy range, this approach is not realistic due to the required level of agreement between data and simulation. Since MC and real data distributions cannot be considered totally compatible, in the analysis method used in this work, the MC distributions are not used to correct real data but the two samples are treated separately and then compared at the end of the analysis.

5.4 Corrections for Spatial Asymmetries

As argued before, the detector geometrical asymmetry results in a variable muon detection efficiency, as a function of the muon direction, since according to the azimuth angle, the number of strings encountered by the muon varies. As a consequence, an azimuthal asymmetry and consequently artificial anisotropy of the arrival direction of cosmic rays would be induced. This asymmetry is corrected for by normalizing the azimuthal distribution in order to obtain a uniform distribution in the following way. The azimuthal distribution is parameterized by N, n_i, and $\bar{n}$, where N is the total number of bins ($N = 360$), n_i is the number of events per bin and $\bar{n}$ is the average number of events:

$$\bar{n} = \frac{1}{N} \sum_{i=1}^{N} n_i \tag{5.2}$$

This parametrization is repeated for every weekly sample in which the total amount of data have been splitted, for both data and MC. This method allows to obtain weights that take into account the fact that the detector is subjected to enviromental conditions which vary over short periods. Fig. 5.11 shows an example of the azimuth distribution for the week 24/12/2011 - 31/12/2011 with the horizontal red line denoting $\bar{n}$ for that week.

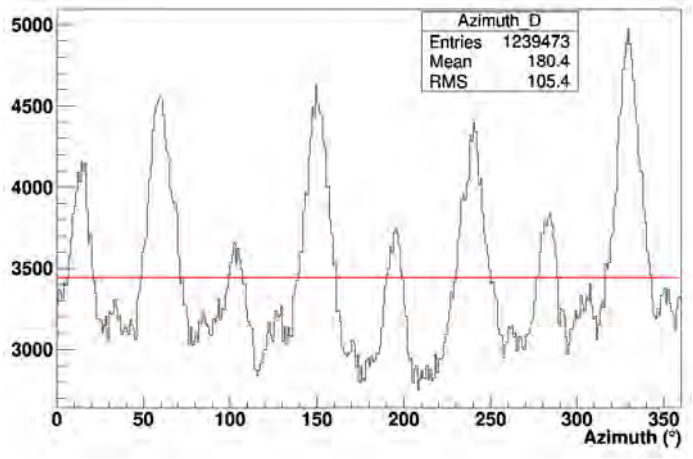

Figure 5.11: Azimuth distribution for the period 24/12/2011 - 31/12/2011. The red line shows the value of $\bar{n}$ for that week.

The corrected azimuthal distribution is obtained by weighting each real and MC event in that week by the relative $\frac{\bar{n}}{n_i}$.

In addition to the azimuthal asymmetry a non uniform $cos\theta$ distribution is observed. Fig. 5.12 shows the $cos\theta$ and zenith distributions for the whole sample after the corrections for the detector geometrical asymmetry have been applied. It is evident that more events arrive from $20° \leq \theta \leq 50°$ compared to those arriving from the zenith and the horizon. This is in contrast with the uniform distribution in $\cos\theta$ that is expected at the entrance of the atmosphere if the flux of CRs is isotropic. However, the events that give rise to the azimuth and zenith distributions shown in fig. 5.10 are tracks of muons which, after being produced in the interaction of primary cosmic rays in the atmosphere, propagate through the atmophere, the sea and the detector where they are observed. Thus, the obtained non-uniform distributions are the consequence of several effects:

- the energy of events: the greater the energy, the greater the probability to be detected; however, vertical events are usually characterized by higher energies since they have traversed a smaller amount of atmosphere compared to those coming from the horizon;
- the effective area seen by the arriving muon is a function of the zenith angle;
- the cut on the number of lines which have recostructed the track (> 1) rejects predominantly vertical events.

Since it is known that the primary CRs distribution in the upper atmosphere is uniform of $cos\theta$, the idea is to exploit the distribution of secondary muons as an estimate of the overall ANTARES efficiency in detecting CRs by means of downgoing atmospheric muons. The atmosphere acts as a filter since both the atmospheric depth at which the primary particle interacts and the distance travelled by the produced muons depends on the primary particle energy and on the atmospheric density. Once produced, only those muons which survive

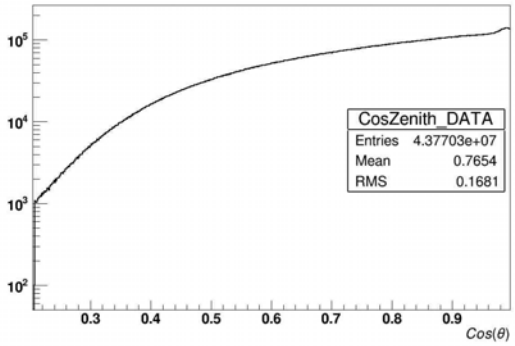

(a)

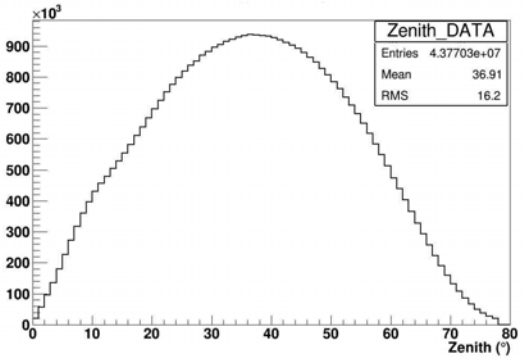

(b)

Figure 5.12: *Cosθ* (a) and Zenith θ (b) distribution for the period 01/01/2009 - 31/12/2011 after the corrections for the detector geometrical asymmetry have been applied.

the absorption due to both the atmosphere and the sea reach the detector, which has its own track reconstruction efficiency, and give rise to the observed *cosθ* distribution. By normalising such distribution to its maximum value, we determine what can be considered the detection efficiency as a function of *cosθ* (fig. 5.13).

The same procedure is used both for data and MC. From now on, each event i is weighted for the efficiency relative to its *cosθ*, $w_i = \frac{1}{eff(cos\theta_i)}$.

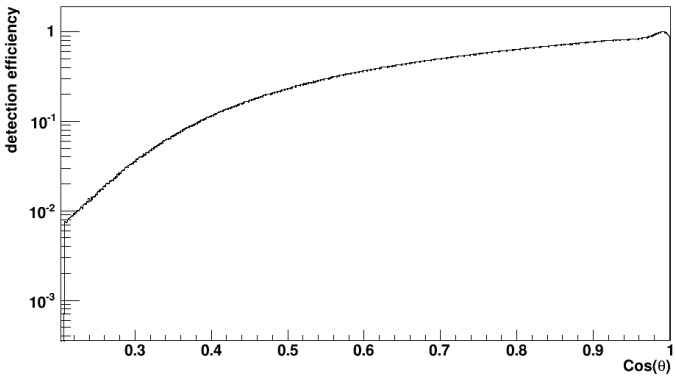

Figure 5.13: Detection efficiency as a function of $cos\theta$.

5.4.1 Check of the stability of spatial corrections

Since the enviromental conditions, the number of active PMTs and the trigger configuration vary with time, the overall detector efficiency, and then the event rates, are affected by these instable conditions with effects on the rate of detected events. This directly affects the azimuth and $cos\theta$ distributions of events and thus the corrections previously described. Therefore it is important to check whether the distributions, and thus the corrections, are stable over long periods or not. In the following it is described how the magnitude of the variations of the weekly distributions of both azimuth and $cos\theta$ for data and MC with respect to the mean monthly distribution is checked. First of all the total sample has been divided into 36 subsamples: one for each month. Each of the 36 subsamples has been in turn divided into 4 subsets, each of whom with a duration of 7 days. Then, the following quantities have been found:

- the percent deviation of the four weekly distributions with respect to the mean monthly distribution, as a function of the angular variable (ϕ or $cos\theta$);
- the distribution of the percent deviation.

In fig. 5.14 and 5.15, the top graphs show the distributions of the two angular variables for the four weekly samples (black, blue, magenta and green) and the mean monthly distribution (red) for data (left graphs) and MC (right graphs). The bottom graphs show the distribution of the percent deviations of the weekly distributions from the mean one.

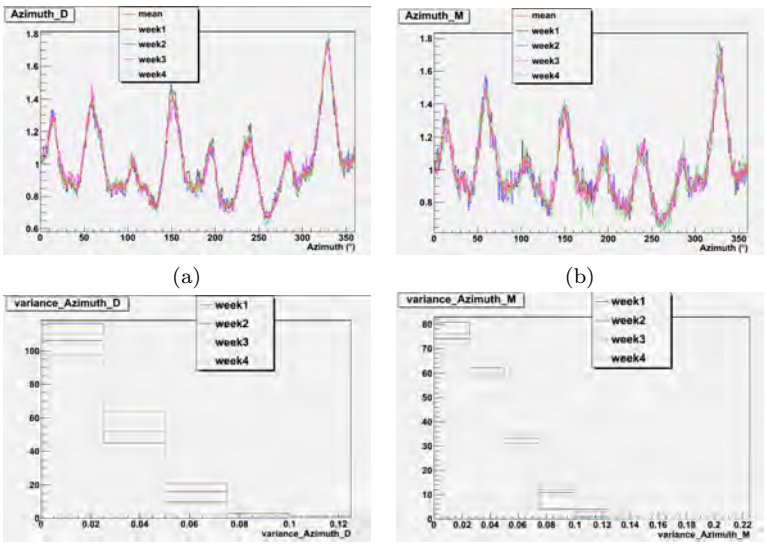

Figure 5.14: Top graphs: Azimuth distributions for the four weekly samples (black, blue, magenta and green) and the mean monthly distribution (red) for data (left graphs) and MC (right graphs). Bottom graphs: distribution of the percent deviation of the weekly distributions from the mean one as a function of the Azimuth angle.

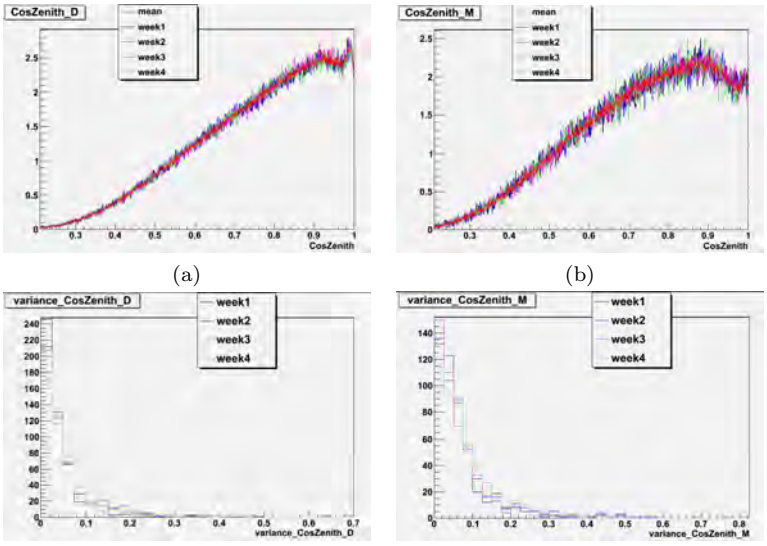

Figure 5.15: Top graphs: $Cos\theta$ distributions for the four weekly samples (black, blue, magenta and green) and the mean monthly distribution (red) for data (left graphs) and MC (right graphs). Bottom graphs: distribution of the percent deviation of the weekly distributions from the mean one as a function of $Cos\theta$.

5.5 Correction for Time Exposure

In this section it is described how the detector relative exposure in each direction on the sky has been estimated. Indeed, after having corrected for non-uniformity in space, we have to take into account any non uniformity in the exposure time, i.e. the amount of time in which each portion of the sky has been observed. A non-uniform exposure map can be caused by several effects: first of all, due to the detector position, not every part of the sky is always or sometimes observed; moreover, during calibration end test runs, the detector is not taking "physics" data implying that the portion of the sky that could be observed during those runs, is not observed at all.

In order to estimate the "coverage" map in equatorial coordinates (right ascension α and declination δ), the following procedure has been used. An angular bin on the celestial sphere is considered visible for the detector in a certain time if its local coordinates are in the range:

- $0^\circ \leq \phi \leq 360^\circ$
- $0^\circ \leq \theta \leq 78^\circ$

The duration of each run k in the selected period (01/01/2009 - 31/12/2011) has been divided in minutes and, for each minute, every couple of coordinates (ϕ_m,θ_n), in the visible range, have been converted in equatorial coordinates by means of the coordinates transformation formula (see Appendix A) that is also a function of the time of the event. The couple of equatorial coordinates (α_i,δ_j) has then be used to fill a 2-dim histogram $E^k_{i,j} = E^k(\alpha_i, \delta_j)$, with a $6^\circ \times 6^\circ$ binning.

The sum over the total amount of runs N of the exposition in each angular bin $\sum_{k=1}^{N} E^k_{i,j}$ gives the coverage map for every couple (α_i, δ_j). Normalising the obtained map to its maximum value provides a new set of weights, functions of the equatorial coordinates, defined as the fraction of the total live time of the detector during the three years in which each angular bin has been visible.

Fig. 5.16 shows the obtained exposure map.

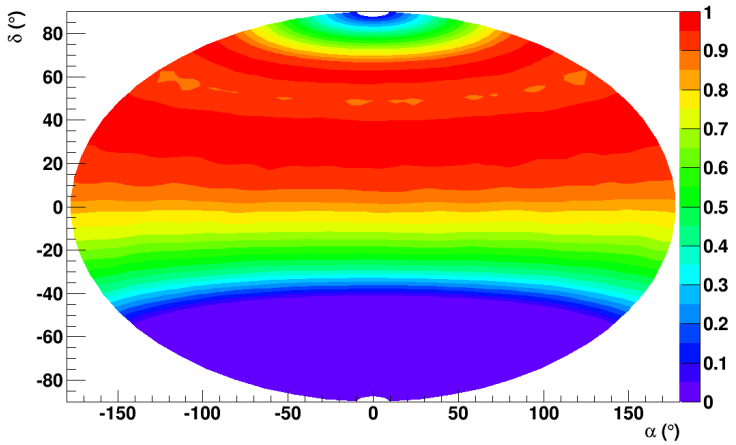

Figure 5.16: Exposure Map. The colour scale shows the fraction of total live-time in which each bin has been visible.

5.6 Study of the correlation between atmospheric temperature and number of observed muons

Another possible effect that can modify the observed muon flux, causing an apparent anisotropy, is the seasonal variation of the atmospheric temperature. This is due to the fact that the atmospheric temperature strictly affects the density of the atmosphere, which has direct effects on the interaction of primary cosmic rays and on the propagation of the shower in the atmosphere. Indeed, increases of the air temperature during summer lower the average gas density; the less dense medium allows a longer mean free path of the mesons and increases the fraction of them that decay to produce muons before their first interaction. Since the atmospheric temperature varies over seasonal periods, it is expected to observe a seasonal modulation in the muon flux as well. Such correlation between fluctuations in atmospheric temperature and variations in the muon intensity at ground level and underground have already been largely studied and observed by experiments like Macro [60], MINOS [61] and Borexino [62]. It is expected that such effect tends to be maximised by large depths. Indeed, at great depths muons tend to come from higher energy pion and kaon parents which are more likely to interact in the atmosphere then decay and the temperature effect we are seeking is due to differential variations in the atmospheric interaction rate of the parent mesons.

5.6.1 Atmospheric Model

Time variations of the atmospheric muon flux ca be related to variations of the atmospheric temperature: $\Delta I_\mu(t) = I_\mu(T(t)) - I^0_\mu$, where I^0_μ is the average value of the atmospheric muon flux. $\Delta I_\mu(t)$ can be related to variations from the average atmospheric temperature at a given altitude X, $\Delta T(X,t) = T(X,t) - T^0(X)$ (from [61]). Considering every altitude layer, the net effect can be written as:

$$\Delta I_\mu(t) = \int_0^\infty dX W(X) \Delta T(X,t) \tag{5.3}$$

with the integral extending over atmospheric depth from the altitude of muon production to the ground. In 5.3, $W(X)$ reflects the altitude dependence of the production of mesons in the atmosphere and their decay into muons that can be observed underground. It can be written as the sum $W_\pi + W_K$, representing the contribution of pions and kaons to the overall variation in muon intensity:

$$W^{\pi,K}(X) \simeq \frac{(1 - X/\Lambda^{'}_{\pi,K})^2 e^{-X/\Lambda_{\pi,K}} A^1_{\pi,K}}{\gamma + (\gamma+1) B^1_{\pi,K} K(X) (\langle E_{thr} cos\theta \rangle / \epsilon_{\pi,K})^2} \tag{5.4}$$

where

$$K(X) \equiv \frac{(1 - X/\Lambda^{'}_{\pi,K})^2}{(1 - e^{-X/\Lambda^{'}_{\pi,K}}) \Lambda^{'}_{\pi,K} / X} \tag{5.5}$$

The parameters $A^1_{\pi,K}$ include the amount of inclusive meson production in the forward fragmentation region, the masses of mesons and muons, and the muon spectral index γ. The parameters $B^1_{\pi,K}$ reflect the relative atmospheric attenuation of mesons; the threshold energy, E_{thr} , is the energy required for a muon to survive to a particular underground depth and θ is the angle between the muon and the vertical directions; the attenuation lengths for the cosmic ray primaries, pions and kaons are Λ_N , Λ_π and Λ_K respectively with $1/\Lambda_{\pi,K} = 1/\Lambda_N - 1/\Lambda_{\pi,K}$. The meson critical energy, $\epsilon_{\pi,K}$, is the meson energy for which decay and interaction have an equal probability. The value of $\langle E_{thr} cos\theta \rangle$ is the median of the distribution.

The atmosphere can be described by many layers with a continuos distribution of temperature and pressure. A possible parametrization considers the atmosphere as an isothermal body with an effective temperature, T_{eff} , obtained from a weighted average over atmospheric depth:

$$T_{eff} = \frac{\int_0^\infty dX T(X) W(X)}{\int_0^\infty dX W(X)} \simeq \frac{\sum_{n=0}^N \Delta X_n T(X_n) W(X_n)}{\sum_{n=0}^N \Delta X_n W(X_n)} \tag{5.6}$$

where the approximation may be done considering that the temperature is measured at discrete atmospheric levels, X_n . We may also define the "effective temperature coefficient", α_T , which quantifies the correlation effect.

$$\alpha_T = \frac{T^0_{eff}}{I^0_\mu} \int_0^\infty dX W(X) \tag{5.7}$$

such that eq. 5.3 may be written:

$$\frac{\Delta I_\mu}{I^0_\mu} = \alpha_T \frac{\Delta T_e f f}{T^0_{eff}} \tag{5.8}$$

Fig. 5.17 shows the measured values for α_T. This value has been predicted for different site depths following [61].

α_T asymptotically approaches unity with increasing site depth. This is because the air-density-independent contribution to the muon signal originating from mesons which have interacted before decaying is progressively left below

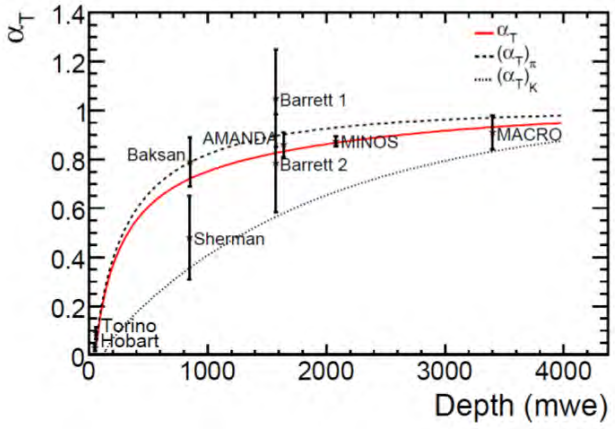

Figure 5.17: Measured values for the effective temperature coefficient, α_T , at varying site depths. The depth is expressed in "meters of equivalent water" in material. The results from different experiments are presented. The red line is the value predicted including muon production by pions and kaons. The dashed lines account for one production mechanism only ([62]).

threshold. At ANTARES depth (2500 m) α_t is expected to be ~ 0.9 (considering muon production from both pions and kaons).

5.6.2 Analysis of muons data

In order to proceed with a quantitative analysis of the relation 5.9, it has to be casted in a form that is suitable for the experimental determination of α_T. We define I_μ as ([60]):

$$I_\mu = \frac{N_i/t_i}{\epsilon A_{eff}\Omega} \tag{5.9}$$

where N_i is the number of observed muons during the live time t_i, ϵ is the efficiency for muon track reconstruction, A_{eff} is the detector effective area, and Ω is the total solid angle viewed by the detector. The fluctuations in the integral muon intensity are then:

$$\frac{\Delta I_\mu}{I_\mu} = \left[\frac{\Delta N_i/t_i}{\epsilon A_{eff}\Omega}\right] / \left[\frac{N_i/t_i}{\epsilon A_{eff}\Omega}\right] = [\Delta N_i/t_i]/[N_i/t_i] = \frac{\Delta R}{R} \approx \frac{(R_\mu - \bar{R_\mu})}{\bar{R_\mu}} \tag{5.10}$$

where $R_\mu = N_i/t_i$ is the muon rate observed by the detector at depths during live time t_i and $\bar{R_\mu} = \sum N_i / \sum t_i$ is the average muon rate over the total data-taking period $\sum t_i$.

However, this approximation is possible only if the conditions of the data-taking are stable over long periods, so that the term $\epsilon A_{eff}\Omega$ can be simplified in the previous equation. This is not the case of the ANTARES detector, since, as shown in the previous sections, it is subjected to rapid variations of the enviromental conditions. Fig. 5.18 shows the rate of observed muons (in s^{-1}),

averaged over 1 day, as a function of the Modified Julian Date (MJD) [1], from MJD = 54832.0 (01/01/2009) to MJD = 55926.0 (31/12/2011).

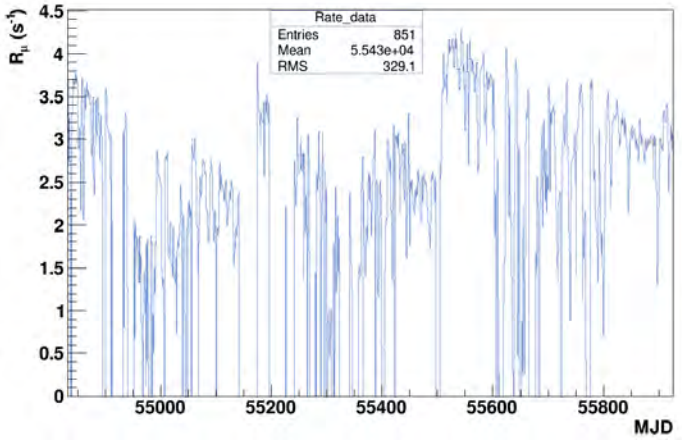

Figure 5.18: Number of observed muons as a function of the Modified Julian Date (MJD), from MJD = 54832.0 (01/01/2009) to MJD = 55926.0 (31/12/2011).

It is evident that $R_\mu = N_i/t_i$ cannot be used at our scope due to the large fluctuations present. However, since in the simulation of MC events, possible correlations with the atmospheric temperature are not taken into account, N_{data} can be replaced by the ratio between real and simulated events, $R = N_{data}/N_{MC}$, that includes all the possible known reasons of R varation due to the detector. Indeed, as shown in the previous sections, the $Run - by - Run$ (4.5.9) simulations ensure that the conditions of the detector are accurately reproduced. The term $\epsilon A_{eff}\Omega$ can then be considered equal for data and MC and so simplified.

The left side of eq. 5.9 may be rewritten as:

$$\frac{\Delta R}{R} \approx \frac{R - \bar{R}}{\bar{R}} \tag{5.11}$$

where R is the ratio between real and simulated events, $R = N_{data}/N_{MC}$, and $\bar{R}$ is the mean value of R during the all live time.

By comparing data and MC we can put in evidence all effects that cannot be attributed to known behaviourS of the detector since all known effects are included in the MC. In order to check any dependence of the muon rate with the atmospheric temperature we decided not to apply the weekly adjustment of the muon rate as described in 5.4. The azimuth correction is still applied but the mean rates are not normailised.

Fig. 5.19 (a) shows the obtained value of $R = N_{data}/N_{MC}$ as a function of time. The resulting behaviour can be explained by the decreasing gain of the PMTs. This is a known effect ($\sim$ 12% per year) that, in ANTARES, has been cured but it still present in the data. From time to time the PMTs HV is

[1] Julian dates are a continuous count of days and fractions since noon Universal Time on January 1,4713 BC. The MJD is related to the Julian date (JD) by the formula: $MJD = JD - 2400000.5$.

increased in order to compensate for the lowering gain. The $Run - by - Run$ MC takes into account this effect that is still present at the level of 25% in 3 years.

The obtained trend has been fitted with the equation of a line with negative slope (red line) and then the result of the fit has been subtracted in order to put in evidence any other effect not included in the MC (like the atmospheric temperature). In order to reduce fluctuatios, the values of R have been averaged over periods of 15 days. The percent variation of R with respect to the mean value $\bar{R}$ is shown in fig. 5.19(b).

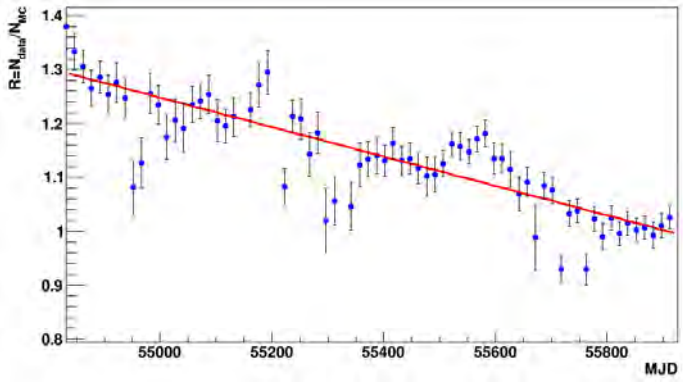

(a)

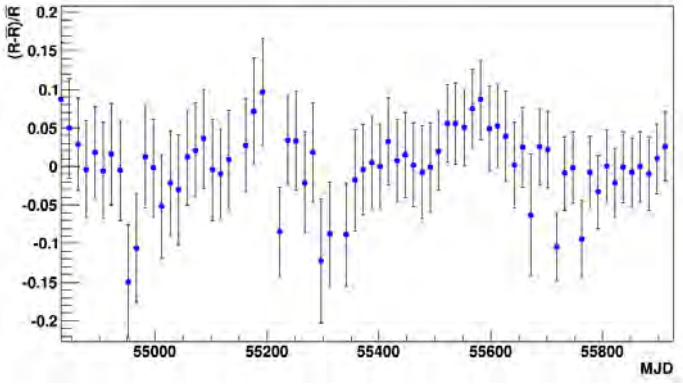

(b)

Figure 5.19: Ratio between real and simulated events as a function of the Modified Julian Date (MJD) (blue) and result of the linear fit (red) (a). Percent variation of R with respect to the mean value $\bar{R}$ in the same period (b).

5.6.3 Analysis of temperature data

The T_{eff} on the left side of eq. 5.9 can be rewritten sobstituting the expression of $W(X)$ (eq. 5.4) in 5.6 and simplified considering only the contribution of π mesons:

$$T_{eff} \approx \frac{\sum_i dXT(X_i)/X_i[exp(-X_i/\Lambda_\pi) - exp(-X_i/\Lambda_N)]}{\sum_i dX/X_i[exp(-X_i/\Lambda_\pi) - exp(-X_i/\Lambda_N)]} \tag{5.12}$$

where $\Lambda_\pi = 160$ g/cm^2 and $\Lambda_N = 120$ g/cm^2. The right side of eq. 5.9 may be rewritten as:

$$\alpha_T \frac{T_{eff}}{T^0_{eff}} \approx \alpha_T \frac{T_{eff} - \bar{T}_{eff}}{\bar{T}_{eff}} \tag{5.13}$$

where T_{eff} is the effective temperature defined in eq. 5.12 and $\bar{T}_{eff}$ is the mean value of T_{eff} over the entire live time. Finally eq. 5.9 can be expressed as:

$$\frac{R - \bar{R}}{\bar{R}} = \alpha_T \frac{T_{eff} - \bar{T}_{eff}}{\bar{T}_{eff}} \tag{5.14}$$

In order to estimate the right side of eq. 5.14, the values of the atmospheric temperature over the ANTARES detector for different preassure levels are needed. The temperature data have been obtained from the European Center for Medium-range Weather Forecasts (ECMWF) [63] which exploits different types of observations (e.g. surface, satellite, and upper air sounding) at many locations around the planet, and uses a global atmospheric model to interpolate the required values to a particular location. In our case, the precise coordinates of the ANTARES detector have been used: $(42°50'N, 6°10'E)$. Atmospheric temperature is provided by the model at 37 discrete pressure levels in the (1-1000) hPa range (1 hPa =1.019 g/cm^2), four times a day at 00.00 h, 06.00 h, 12.00 h, and 18.00 h, in a grid of $2° \times 2°$ centered at the ANTARES location with a 0.5° step, for a total of 25 values of temperature per pressure level, per time interval. The mean temperature among the 25 values in the grid and the 4 times in a day gives the final value of the temperature for each preassure level, in each day in the period 01/01/2009 to 31/12/2011. Fig. 5.20 shows the mean daily temperature as a function of the day, from day=0 (01/01/2009) to day=1095 (31/12/2011) for each of the 37 different preassure levels.

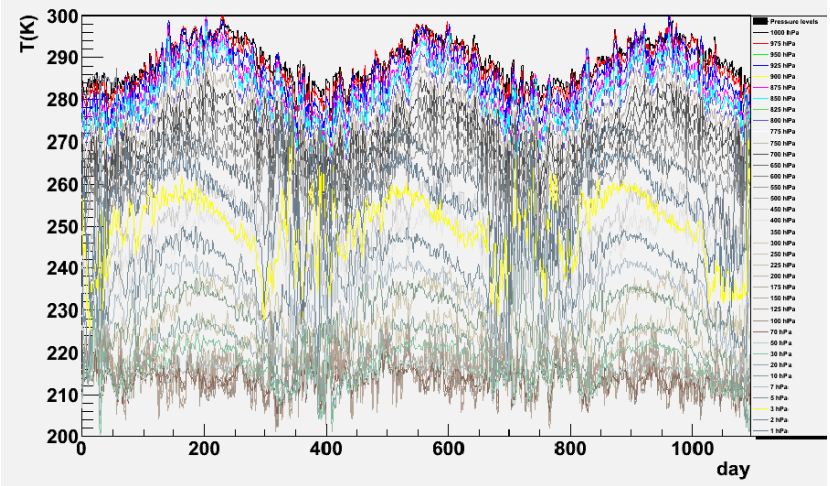

Figure 5.20: Mean daily temperature as a function of the day, from day=0 (01/01/2009) to day=1095 (31/12/2011) for each of the 37 different preassure levels.

Based on this data set, T_{eff} was calculated using eq. 5.12. The graphs representing T_{eff} as a function of the time, for the period 01/01/2009 - 31/12/2011 and the percent variation of T_{eff} with respect to the mean value $\bar{T}_{eff}$ are presented in fig. 5.21 (a) and (b). The values of T_{eff} have been avaraged over periods of 15 days so that the percent variations of R and T_{eff} can be compared.

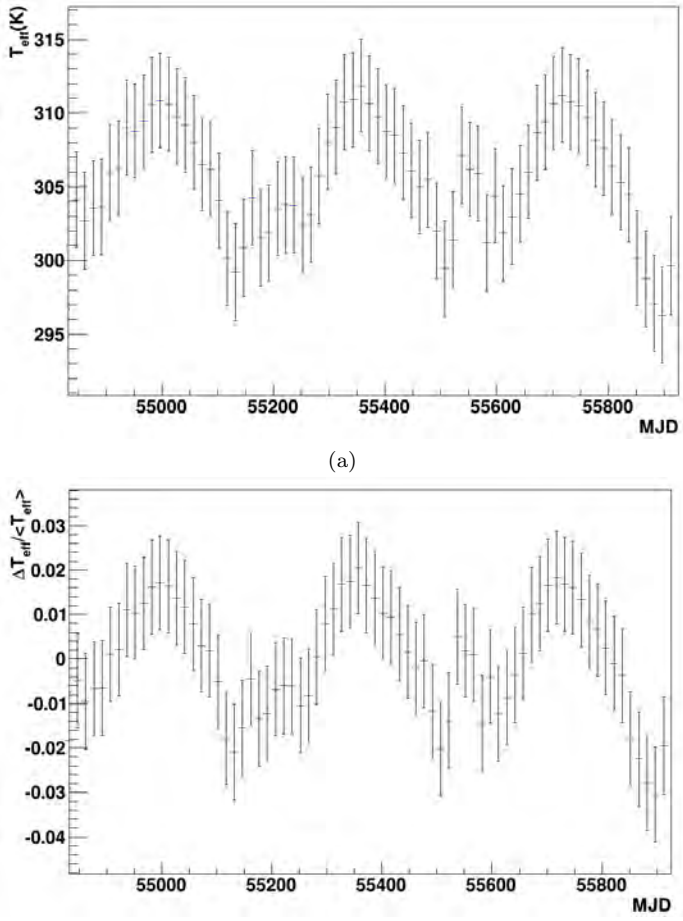

(a)

(b)

Figure 5.21: T_{eff} as a function of the Modified Julian Date (MJD) (a). Percent variation of T_{eff} with respect to the mean value $\bar{T}_{eff}$ in the same period (b).

5.6.4 Correlation between observed events and atmospheric temperature

The predicted linear relation 5.14 together with the known value of the coefficient α_T and of the percent fluctuation of T_{eff} allows to give an estimation of the expected percent variation of the R as a function of T_{eff}. In graph 5.21 (b) a fluctuation of the order of $\lesssim \pm 3\%$ can be observed. Since, according to fig. 5.17, a value of $\alpha_T \sim 0.95$ for the ANTARES detector depth and for a π-only

muon production is predicted, the expected fluctuation of R is:

$$\frac{R-\bar{R}}{\bar{R}} = \alpha_T \frac{T_{eff}-\bar{T}_{eff}}{\bar{T}_{eff}} \approx 0.95 \cdot 0.3 = 2.85\% \tag{5.15}$$

However, graph 5.19 shows pecent variations of the ratio between data and MC of the order of 10%. Moreover, the same sinusoidal trend observed for $\Delta T_{eff}/\bar{T}_{eff}$ should be present in the $\Delta R/\bar{R}$ behaviour if the two trends were correlated, but the $\Delta R/\bar{R}$ distribution, due also to the high statistical fluctuation, can be considered slightly uniform. This result is confirmed by the graph 5.22 which is a scatter plot of $\Delta R/\bar{R}$ versus $\Delta T_{eff}/\bar{T}_{eff}$.

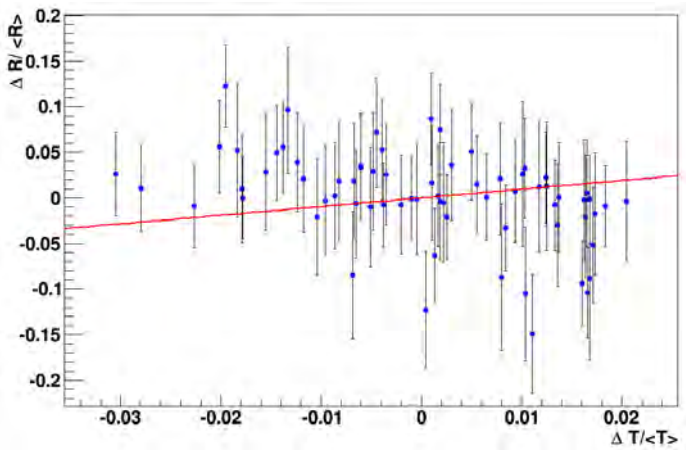

Figure 5.22: $\Delta R/\bar{R}$ versus $\Delta T_{eff}/\bar{T}_{eff}$ for the analysed period. The red line shows the expected linear trend.

If the correlation was of the type expected in 5.14, a linear trend of $\Delta R/\bar{R}$ versus $\Delta T_{eff}/\bar{T}_{eff}$ should be observed (red line in fig. 5.22). This is not visible due to statistical fluctuations. A possible cause of such a large fluctuation of R could be due to the MC simulation, not completely able to reproduce the enviromental conditions in which the detector operates.

To conclude, the used data sample with the applied cuts does not show a correlation with the atmospheric temperature. However, since such correlation is a well known effect already observed by several experiments, we have decided to apply the correction due to the atmospheric temperature to the number of observed muons. In particular, each event in a certain 15 days period p has been multiplied by a weight estimated from the averaged temperature in the same period:

$$w_p = \frac{1}{\alpha_T(\frac{\Delta T_{eff}}{T_{eff}})_p + 1} \tag{5.16}$$

5.7 Analysis of the Anisotropy

The corrections described in the previous sections have been adopted in order to obtain the map in equatorial coordinates of the number of observed events as a

function of their true arrival direction, so that a possible large scale anisotropy can be verified. In particular, the first correction purpose was to reduce the asymetry due to the structure of the detector, reproducing a different detection efficiency, as a function of the azimuth angle. The second correction aimed at reproducing the primary CRs flux exploiting the observed $cos\theta$ distribution of secondary muons as an estimation of the detector efficiency. Then, one other correction was needed in order to compensate for the non-uniform sky exposure in time. Finally, the last correction aimed at reducing the seasonal effect caused by variations of the atmospheric temperature. It is now possible to obtain the distribution of the arrival directions in equatorial coordinates for both data and MC, shown in fig. 5.23.

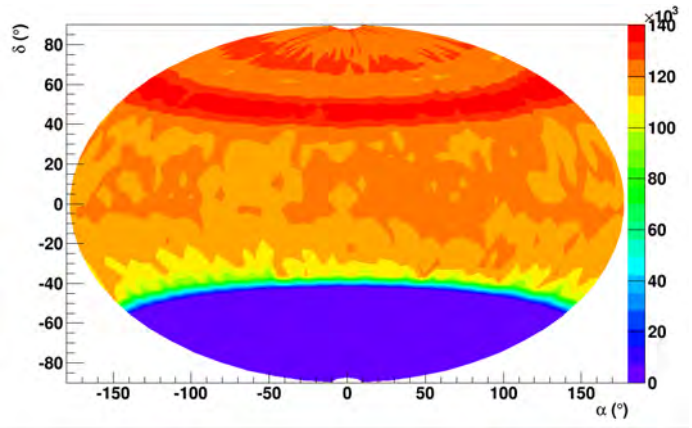

(a)

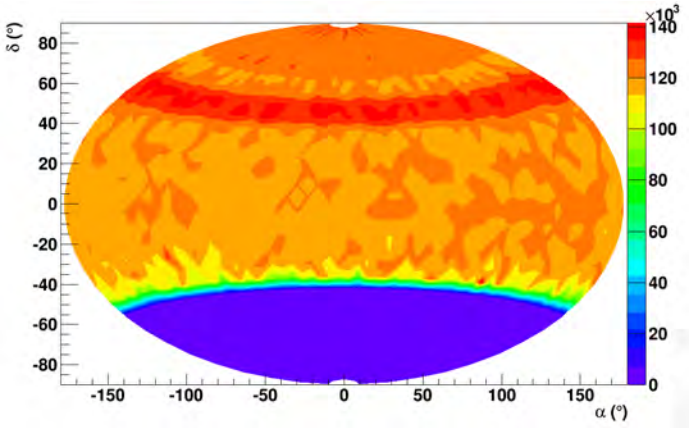

(b)

Figure 5.23: Distribution of events in equatorial coordinates. Binning $6° \times 6°$. (a) Data corrected using azimuth and zenith distributions obtained from data itself. (b) MC corrected using azimuth and zenith distributions obtained from MC itself.

It is evident that the two maps are not completely uniform. The first feature that can be noted is that, fixing a right ascension α angle and moving along the relative declination δ_α band, a variation of the number of events as large

as 50% can be observed. However, it is possible to perform an analysis of the anisotropy along the right ascension since declination bands with an almost constant number of events as a function of α have been obtained.

We divide the map in equatorial coordinates in 30×60 angular bins $n(\alpha, \delta)$ in declination ($\Delta\delta = 6°$) and right ascension($\Delta\alpha = 6°$). For each bin in declination we evaluate the average $\bar{n}_{\delta_j} = \frac{1}{\sum P_{i,j}} \sum_{i=1}^{60} n(\alpha_i, \delta_j) P_{i,j}$. This value is used to normalize to 1 the content of each bin in right ascension $n(\alpha_i, \delta_j)$ and to search for anisotropies as deviations from 1. This procedure gives rise to the CR *relative intensity maps* shown in fig 5.24 for data (a) and MC (b).

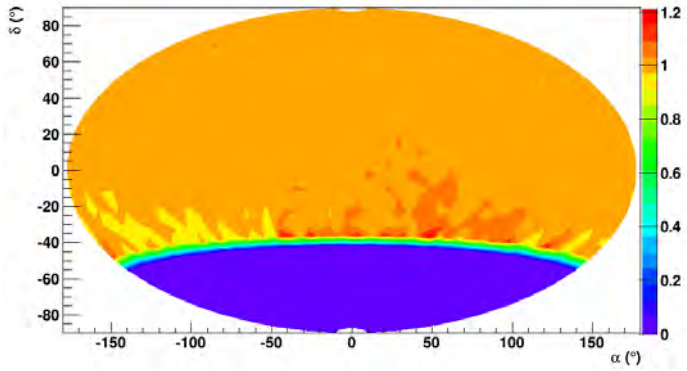

(a)

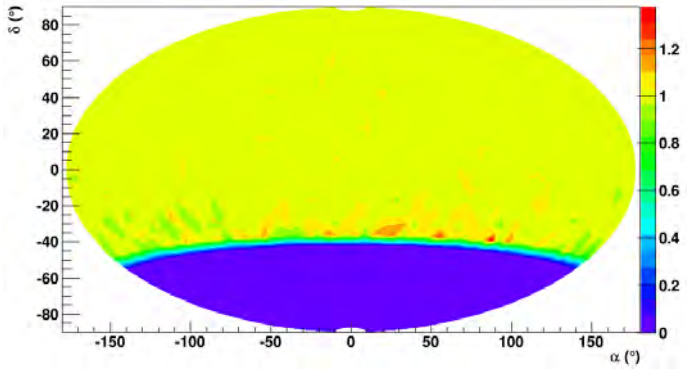

(b)

Figure 5.24: Relative intensity maps in equatorial coordinates for data (a) and MC (b). Binning $6° \times 6°$.

The first map shows an excess for values of α between 0° and 100° ($[0°, 100°]$ if the right ascension is expressed from 0° to 360°) and a deficit between $-180°$ and 0° and between 100° and 180° ($[100°, 360°]$). The map for the simulated events is instead more uniform and the two zones above-mentioned are not visible. Fig. 5.25 shows the anisotropy profile in right ascension obtained by accumulating the relative intensity distributions from the declination belts for data (a) and MC (b). It is possible to note the same trend already observed in the relative intensity maps: the anisotropy profile for data shows a more evident oscillatory trend with respect to the MC profile.

To quantify the scale of the anisotropy, the right ascension dependence of

the data has been fitted to a first- second- and third- order harmonic function of the form (see Appendix B):

$$f'(\alpha) = A_1 \cdot cos(\alpha - \phi_1) + B, \tag{5.17}$$

$$f''(\alpha) = A_1 \cdot cos(\alpha - \phi_1) + A_2 \cdot cos2(\alpha - \phi_2) + B, \tag{5.18}$$

$$f'''(\alpha) = A_1 \cdot cos(\alpha - \phi_1) + A_2 \cdot cos2(\alpha - \phi_2) + A_3 \cdot cos3(\alpha - \phi_3) + B. \tag{5.19}$$

Moreover, the two graphs have also been fitted with the equation of a line in order to test the hypothesis of constant trend:

$$f^0(\alpha) = m \cdot \alpha + q \quad , \quad m = 0 \tag{5.20}$$

Fig. 5.25 shows the anisotropy profiles along the right ascension for both data and MC together with the four functions used for the fits. The parameters values obtained with the fit are reported in tab. 5.1.

Since the distributions show a large dispersion of data, it is unlikely to find a function which represent satisfactorily the obtained trends. The parameters obtained from the fit suggest that for both data and MC the hypothesis of constant trend is the worst description of the distributions.

Concerning the fit with the three harmonics, it is evident that the hypothesis of oscillatory trend cannot be totally excluded for the MC events, whose distributions are expected to be uniform after corrections. This implies that there could still be, in the analysis procedure for example, a systematic effect that causes an apparent anisotropy.

However, the fit with the harmonics give different values of amplitudes and phases for the data distribution with respect to the MC. This suggests that the modulation effect along the R.A. in the MC distribution is not coincident with the one which causes the modulation in the data distribution.

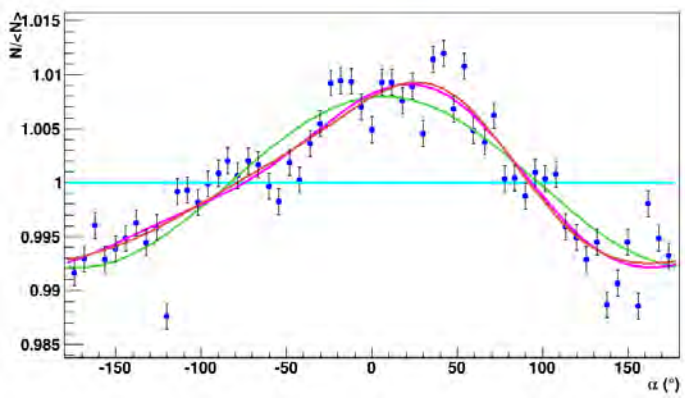

(a)

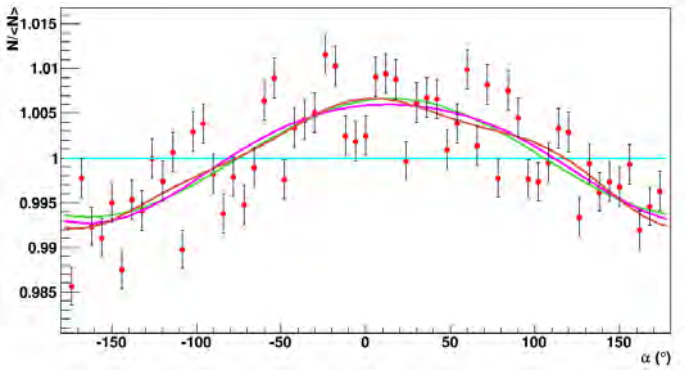

(b)

Figure 5.25: Anisotropy profiles for data (a) and MC (b). The results of the fit are also shown: the light blue line shows the linear fit ($y = m \cdot x + q$), the green line shows the fit with the first harmonic ($y = A_1 \cdot cos(x - \phi_1) + B$), the pink line shows the fit with the second harmonic ($y = A_1 \cdot cos(x - \phi_1) + A_2 \cdot cos2(x - \phi_2) + B$) and the brown line shows the fit with the third harmonic ($y = A_1 \cdot cos(x - \phi_1) + A_2 \cdot cos2(x - \phi_2) + A_3 \cdot cos3(x - \phi_3) + B$).

	Linear Fit	
	q	χ^2/ndf
data	1.0000 ± 0.0001	1678/59
MC	1.0000 ± 0.0002	476/59

	First Harmonic			
	$A_1(10^{-3})$	$\phi_1(^\circ)$	B	χ^2/ndf
data	7.92 ± 0.21	0.12 ± 0.03	1.0000 ± 0.0001	333/57
MC	6.63 ± 0.40	0.26 ± 0.06	1.0000 ± 0.0003	198/57

	Second Harmonic					
	$A_1(10^{-3})$	$\phi_1(^\circ)$	$A_2(10^{-3})$	$\phi_2(^\circ)$	B	χ^2/ndf
data	7.92 ± 0.22	0.12 ± 0.03	1.74 ± 0.21	0.68 ± 0.60	1.0000 ± 0.0001	268/55
MC	6.62 ± 0.40	0.26 ± 0.06	0.68 ± 0.39	1.87 ± 0.29	1.0000 ± 0.0003	195/55

	Third Harmonic							
	$A_1(10^{-3})$	$\phi_1(^\circ)$	$A_2(10^{-3})$	$\phi_2(^\circ)$	$A_3(10^{-3})$	$\phi_3(^\circ)$	B	χ^2/ndf
data	7.92 ± 0.21	0.12 ± 0.03	1.74 ± 0.22	0.69 ± 0.06	-0.39 ± 0.22	-0.25 ± 0.18	1.0000 ± 0.0001	265/53
MC	6.62 ± 0.40	0.26 ± 0.06	0.68 ± 0.40	1.87 ± 0.29	-0.78 ± 0.40	-1.06 ± 0.17	1.0000 ± 0.0003	191/53

Table 5.1: Results of the four fits.

Chapter 6

Conclusions

In this work, data collected by the ANTARES detector in the period 01/01/2009 - 31/12/2011 has been analysed with the intention of searching for the large scale anisotropy in the high energy primary Cosmic Rays arrival directions, already observed by several experiments both in the Northern and in the Southern emispheres [47] [48] [49] [19]. Since several factors can mimic an apparent anisotropy preventing from obtaining the real distributions of data, the first step was to remove such systematic effects with a series of corrections. The first aspect which needs to be taken into account is the granularity of the apparatus that is not a compact structure but it is composed of twelve lines separated at a distance of about 60 m (fig. 5.6). Those lines are equipped with a series of PMTs which are used to observe the Cherenkov light emitted along the track in water traveled by the high energy muon produced in the atmospheric showers after the interaction of the primary cosmic rays with the atmosphere. The arrangement of the lines induce a different capability of muon detection depending on the muon arrival direction, causing a deformation of the azimuth distributions (fig. 5.4 (a)).

Moreover, the zenith distribution undergoes an alteration as well (fig. 5.4 (b)) due to both the amount of atmosphere traversed by the produced muon and the not uniform reconstruction efficiency of the apparatus.

Furthermore, the sky exposure, which is the amount of time in which each angular bin in equatorial coordinates is visible for the detector, is clearly uneven due to several factors: the ANTARES latitude, which causes that different sky regions are in the detector field of view in different times in a sideral day, the selection of the runs used for the analysis and the fact that some runs are used for calibrations and tests. This effect has been corrected as well normalising the number of events from a certain angular bin with the fraction of time in which that bin has been visible (fig. 5.16).

The same selection and cuts have been applied to both data and MonteCarlo events, with the corrections being obtained from the two distributions separately since the observed not perfect agreement between data and MonteCarlo does not allow to use the angular distributions of the simulated events to correct the distributions of the real events (fig 5.10).

Since one of the possible effect that can modify the observed muon flux, causing an apparent anisotropy, is the seasonal variation of the atmospheric temperature, the rate of observed muons and the variation of the air temperature have been studied in order to see a possible correlation. Indeed, increases of the

air temperature during summer lower the average gas density; the less dense medium allows a longer mean free path of the mesons (parents of the muons) and increases the fraction of them that decay to produce muons before interacting. In particular, as already studied by other underground experiments [60] [61] [62], it is expected to observe an annual modulation in the muon intensity of the order of $\sim 3\%$. Even if the high fluctuations in the muon rate have not allowed to verify such correlation (fig. 5.22), data have been corrected in order to compensate for the known effect due to fluctuations in the atmospheric temperature.

The corrected obtained maps in equatorial coordinates (fig 5.23) show an evident dependence on the declination. However, the events distribution along the right ascension is uniform and this allows to perform an analysis of the anisotropy in each declination band. Therefore, the two relative intensity maps (fig. 5.24) have been obtained by dividing the content of each angular bin by the mean value of the bin contents in the relative declination band. Then, in order to quantify the scale of the anisotropy, the right ascension dependence of the data has been fitted to a first-, second- and third- order harmonic function together with a line, used to test the hypothesis of constant trend for the MC distribution. The obtained results (fig. 5.25) show that the hypothesis of oscillatory trend cannot be completely excluded for the MC distribution, indicating an eventual systematic effect which causes an apparent anisotropy. However, since different values of amplitudes and phases have been obtained with the harmonics fit for the two distributions, the modulation effect along the R.A. in the data distribution cannot be explained by the same effect which causes the modulation in the MC distribution.

Appendix A

Celestial Coordinates

In order to specify sky positions, astronomers have developed several coordinate systems. Each uses a coordinate grid projected on the Celestial Sphere, in analogy to the Geographic coordinate system used on the surface of the Earth. The celestial sphere is an imaginary sphere of gigantic radius, centered on the Earth. All objects which can be seen in the sky can be thought of as lying on the surface of this sphere. Since their distances are indeterminate, only the direction toward the object to locate it in the sky is needed. The coordinate systems differ only in their choice of the fundamental plane, which divides the sky into two equal hemispheres along a great circle (the fundamental plane of the geographic system is the Earth's equator). Each coordinate system is named for its choice of fundamental plane.

A.1 Equatorial Coordinates

The Equatorial coordinate system is the most closely related to the Geographic coordinate system, because they use the same fundamental plane, and the same poles. The projection of the Earth's equator onto the celestial sphere is called the Celestial Equator. Similarly, projecting the geographic Poles onto the celestial sphere defines the North and South Celestial Poles.

However, the geographic system is fixed to the Earth, i.e. it rotates as the Earth does, while the Equatorial system is fixed to the stars, so it appears to rotate across the sky with the stars.

The latitudinal (latitude-like) angle of the Equatorial system is called Declination (δ) ($[-90^\circ, 90^\circ]$). It measures the angle of an object above or below the Celestial Equator. The longitudinal angle is called the Right Ascension (α). It measures the angle of an object East of the Vernal Equinox [1] γ (see fig. A.1). Unlike longitude, Right Ascension is usually measured in hours instead of degrees, because the apparent rotation of the Equatorial coordinate system is closely related to Local Sidereal Time (LST) and Hour Angle (h). In particular, the Right Ascension can be obtained from the Hour Angle as $\alpha = LST - h$.

[1] the Vernal Equinox is the point on the Celestial Sphere in which the Celestial Equator and the Ecliptic intersect. The Ecliptic is an imaginary Great Circle on the Celestial Sphere along which the Sun appears to move over the course of a year.

Since a full rotation of the sky takes 24 hours to complete, there are (360 degrees / 24 hours) = 15 degrees in one Hour of Right Ascension.

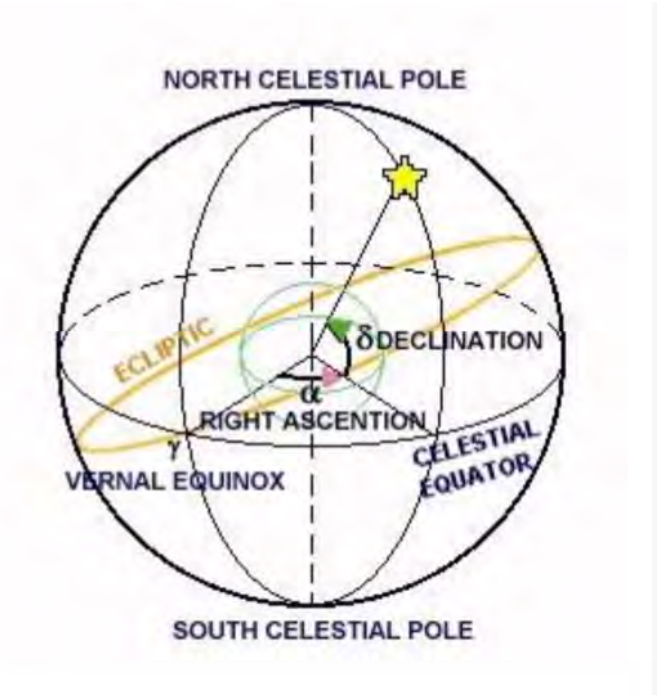

Figure A.1: Equatorial coordinates system.

A.2 Horizontal Coordinates

The Horizontal (or Local) coordinate system uses the observer's local horizon as the Fundamental Plane. This conveniently divides the sky into the upper hemisphere and the lower hemisphere. The pole of the upper hemisphere is called the Zenith. The pole of the lower hemisphere is called the nadir. The angle of an object above or below the horizon is called the Altitude (H) and it is defined in the angular range [$-90°$,$90°$]. The angle of an object around the horizon (measured from the North point, toward the East) is called the Azimuth (ϕ) [$0°$,$360°$] (see fig. A.2). Sometimes the H coordinate is replaced with the Zenith angle θ ([$0°$,$180°$]) which is defined as $\theta = 90° - H$.

The Horizontal Coordinate System is fixed to the Earth, not the Stars. Therefore, the Altitude and Azimuth of an object changes with time, as the object appears to drift across the sky. In addition, because the Horizontal system is defined by the observer local horizon, the same object viewed from different locations on Earth at the same time will have different values of Altitude and Azimuth.

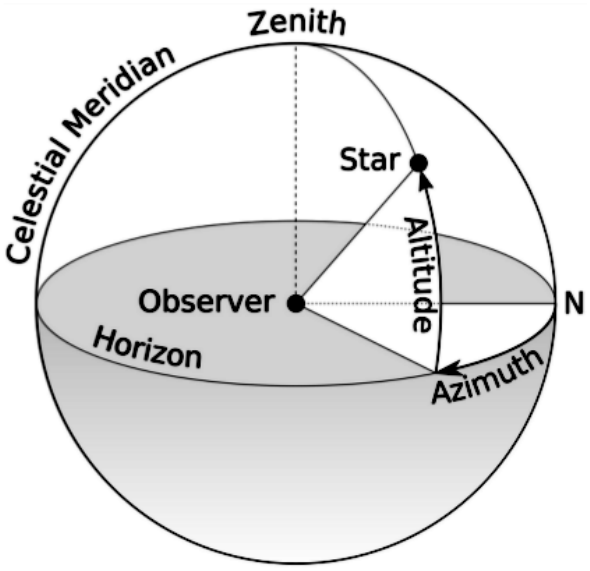

Figure A.2: Horizontal coordinates system.

A.3 Coordinate transformation

It is possible to pass from the equatorial coordinates (h and δ) to the horizontal coordinates (θ and ϕ) and viceversa by means of the following relations:

- the hour angle h can be obtained from the local coordinates through the equation

$$tgh = -\frac{cos\phi}{cot\theta cos\lambda - sin\lambda \sin\phi} \tag{A.1}$$

  where λ is the latitude of the observer. As described in A.1, the hour angle h is defined as $h = LST - \alpha$, with α being the right ascension and LST the local sideral time.

- the declination δ can be obtained from the local coordinates with the equation:

$$sin\delta = sin\lambda cos\theta + sin\lambda sin\theta sin\phi \tag{A.2}$$

Appendix B

Spherical Harmonics and Multipole Expansion

B.1 Spherical Harmonics

Given a spherical coordinates system, the position of a point on a unit sphere is described by the versor:

$$\hat{r} = (sin(\theta)sin(\phi), sin(\theta)cos(\phi), cos(\phi)) \tag{B.1}$$

where θ and ϕ represent the zenith and the azimuth angle respectively. The spatial distribution on the unit sphere of a set of objects can be described by means of a set of functions, known as spherical harmonics, which depend on the two angles where θ and ϕ. The spherical harmonics $Y_l^m(\theta, \phi)$ are the angular portion of the solution to Laplace's equation in spherical coordinates where azimuthal symmetry is not present. Writing $F = \Phi(\phi)\Theta(\theta)$ in this equation gives:

$$\frac{\Phi(\phi)}{\sin\theta}\frac{d}{d\theta}(sin\theta\frac{d\Theta}{d\theta}) + \frac{\Theta(\theta)}{sin^2\theta}\frac{d^2\Phi(\phi)}{d\phi^2} + l(l+1)\Theta(\theta)\Phi(\phi) = 0. \tag{B.2}$$

Multiplying by $sin^2\theta/(\Theta\Phi)$ gives

$$\left[\frac{sin\theta}{\Theta(\theta)}\frac{d}{d\theta}(sin\theta\frac{d\Theta}{d\theta}) + l(l+1)sin^2\theta\right] + \frac{1}{\Phi(\phi)}\frac{d^2\Phi(\phi)}{d\phi^2} = 0 \tag{B.3}$$

Using separation of variables by equating the ϕ-dependent portion to a constant gives

$$\frac{1}{\Phi(\phi)}\frac{d^2\Phi(\phi)}{d\phi^2} = -m^2 \tag{B.4}$$

which has solutions

$$\Phi(\phi) = Ae^{-im\phi} + Be^{im\phi} \tag{B.5}$$

Plugging in B.4 into B.3 gives the equation for the θ-dependent portion, whose solution is

$$\Theta(\theta) = P_l^m(cos\theta) \tag{B.6}$$

where $m = -l, -(l-1), ..., 0, ..., l-1, l$ and $P_l^m(z)$ is an associated Legendre polynomial. The spherical harmonics are then defined by combining $\Phi(\phi)$ and $\Theta(\theta)$,

$$Y_l^m(\theta,\phi) \equiv \sqrt{\frac{2l+1}{4\pi}\frac{(l-m)!}{(l+m)!}} P_l^m(cos\theta)e^{im\phi} \tag{B.7}$$

where the normalization is chosen such that

$$\int_0^{2\pi}\int_0^{\pi} Y_l^m(\theta,\phi)\bar{Y}_{l'}^{m'}(\theta,\phi)sin\theta d\theta d\phi = \int_0^{2\pi}\int_{-1}^{1} Y_l^m(\theta,\phi)\bar{Y}_{l'}^{m'}(\theta,\phi)d(cos\theta)d\phi = \delta_{mm'}\delta_{ll'} \tag{B.8}$$

Here, $\bar{z}$ denotes the complex conjugate and δ_{mn} is the Kronecker delta. Some of the lower spherical harmonics are reported in fig. B.1.

$Y_{0,0} = \frac{1}{(4\pi)^{1/2}}$	$Y_{2,0} = \left(\frac{5}{16\pi}\right)^{1/2}(3\cos^2\theta - 1)$
$Y_{1,0} = \left(\frac{3}{4\pi}\right)^{1/2}\cos\theta$	$Y_{2,1} = -\left(\frac{15}{8\pi}\right)^{1/2}\sin\theta\cos\theta e^{i\phi}$
$Y_{1,1} = -\left(\frac{3}{8\pi}\right)^{1/2}\sin\theta e^{i\phi}$	$Y_{2,-1} = \left(\frac{15}{8\pi}\right)^{1/2}\sin\theta\cos\theta e^{-i\phi}$
$Y_{1,-1} = \left(\frac{3}{8\pi}\right)^{1/2}\sin\theta e^{-i\phi}$	$Y_{2,2} = \left(\frac{15}{32\pi}\right)^{1/2}\sin^2\theta e^{2i\phi}$
	$Y_{2,-2} = \left(\frac{15}{32\pi}\right)^{1/2}\sin^2\theta e^{-2i\phi}.$

Figure B.1: Spherical Harmonics up to $l = 2$, $-l < m < l$

B.2 Multipole Expansion

Any distribution $F(\theta,\phi)$ on the unit sphere can be described by means of a multipole expansion, i.e. through a combination of spherical harmonics Y_l^m, each of whom multiplied by a coefficient a_l^m:

$$F(\theta,\phi) = F_0^{'}\sum_{l=0}^{\infty}\sum_{m=-l}^{l} a_l^m Y_l^m(\theta,\phi) \approx F_0^{'}\sum_{l=0}^{n}\sum_{m=-l}^{l} a_l^m Y_l^m(\theta,\phi) \tag{B.9}$$

with n defining the maximum approximation and F_0 being a constant.

- $n = 0$ gives the isotropic component of the distribution $F(\theta,\phi)$:

$$F(\theta,\phi) \approx F_0^{'}a_0^0 Y_0^0(\theta,\phi) = F_0^{'}a_0^0 = const \tag{B.10}$$

- n=1 gives the dipolar component:

$$\begin{aligned} F(\theta,\phi) &= F_0^{'}\sum_{l=0}^{1}\sum_{m=-1}^{1} a_l^m Y_l^m(\theta,\phi) \\ &= F_0^{'}(a_0^0 + \sum_{m=-1}^{1} a_l^m Y_l^m(\theta,\phi)) \\ &= F_0(1+\hat{e}(\theta,\phi)\cdot\vec{D}(\theta_{dip},\phi_{dip})) \\ &= F_0\left(1+\frac{1}{3}\begin{pmatrix} Y_1^1 \\ Y_1^{-1} \\ Y_1^0 \end{pmatrix}\cdot\vec{D}(\theta_{dip},\phi_{dip})\right) \end{aligned} \tag{B.11}$$

  where

$$\hat{e}(\theta,\phi) = \begin{pmatrix} sin\theta sin\phi \\ sin\theta cos\phi \\ cos\phi \end{pmatrix} = \frac{1}{3}\begin{pmatrix} Y_1^1 \\ Y_1^{-1} \\ Y_1^0 \end{pmatrix} \tag{B.12}$$

  is the versor of the generic direction (θ,ϕ), while $\vec{D}(\theta_{dip},\phi_{dip})$ is the dipole vector relative to the direction $(\theta_{dip},\phi_{dip})$, and defined as:

$$\vec{D} = \begin{pmatrix} D_x \\ D_y \\ D_z \end{pmatrix} = \begin{pmatrix} \sqrt{3}/a_0^0\cdot a_1^1 \\ \sqrt{3}/a_0^0\cdot a_1^{-1} \\ \sqrt{3}/a_0^0\cdot a_1^0 \end{pmatrix} = \begin{pmatrix} sin\theta_{dip} sin\phi_{dip} \\ sin\theta_{dip} cos\phi_{dip} \\ cos\phi_{dip} \end{pmatrix} \tag{B.13}$$

- Greater values of n give a better approximation of the function $F(\theta,\phi)$.

Appendix C

Large Scale Anisotropy analysis methods

C.1 East - West method

The "East-West method" [56] is a differential method, as it is based on the analysis of the difference of the counting rates in the East ($N_E(t)$) and West ($N_W(t)$) directions with respect to the field of view of the detector for a certain value of the local sideral time t (fig. C.1). The method is largely independent of experimental effects, that is, it does not require corrections for acceptance and/or for atmospheric effects. The total counting rate of events observed in either the Eastern or the Western half of the field of view of an EAS array experiences different kind of variations during a sidereal day. Those may be caused either by experimental effects (changes of measurement conditions during the data taking, atmospheric effects on EAS, etc.) and/or by real variations in the primary CR fluxes from different parts of the sky. The East-West method is aimed at reconstructing the equatorial component of a genuine large scale pattern by using only the difference of the counting rates of the Eastern and Western hemispheres. The effects of experimental origin, being independent of the incoming direction, are expected to be removed through the subtraction.

Through the spherical harmonic expansion, the difference $N_E(t) - N_W(t)$ is related to the amplitude A_n and the phase ϕ_n of the spherical harmonic functions by the relation:

$$\Delta N_{EW} = \frac{N_E(t) - N_W(t)}{N_E(t) + N_W(t)} \approx \sum_n A_n sin(n(t - \phi_n)) \tag{C.1}$$

This method relys on the righ ascension α modulation due to the relation $\alpha = t - h$ with the local sideral time t and the hour angle h.

C.2 Forward - Backward method

The technique of forward-backward asymmetry (FB) uses the number of events (N_F and N_B) collected in some small time interval $\Delta\xi$ in two "telescopes", i.e.

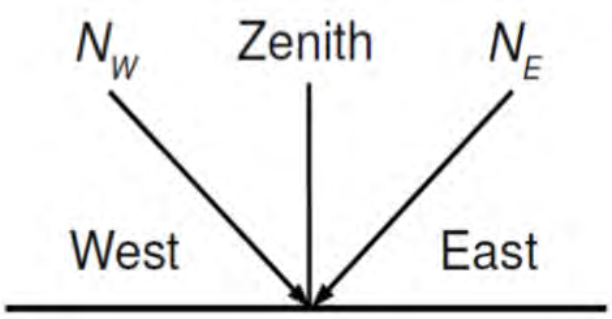

Figure C.1: Illustration of the E-W method.

pixels of small and equal solid angle, at the same forward and backward angle as shown in Fig. C.2:

$$FB = \frac{N_F - N_B}{N_F + N_B} \tag{C.2}$$

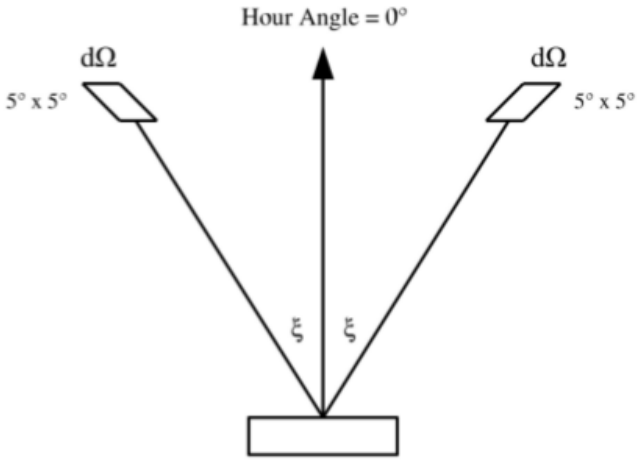

Figure C.2: Diagram showing the definition of ξ used in the calculation of the forward-backward asymmetry for a single dec. band and a given 30 minute histogram. ξ is in the direction of hour angle.

The expression of FB is manifestly independent of overall detector rate (as in the East - West method), as can be seen from the invariance of FB under the substitution N_F, $N_B \to cN_F$, cN_B , a common requirement in all experiments

using the atmosphere as part of their detector.The analysis method utilizes the rotation of the Earth to search for a coherent modulation of FB during a 24 hour day. The FB modulation does not directly give the anisotropy of the sky, but is a function of it. As a region of the sky with an excess cosmic-ray flux relative to the average (a positive anisotropy region) is swept into the forward "telescope" FB becomes more positive; when the same excess is swept into the backward "telescope", FB becomes negative. One can think of FB as a coarse "derivative" of the actual anisotropy of the sky. Thus the FB modulation is a tool to obtain the quantity of interest, the fractional anisotropy (i.e. deviation from uniformity) of the sky.

Once fixed a declination band δ the amplitude A_n and the phase ϕ_n of the spherical harmonic expansion can be obtained as:

$$\Delta N^{\delta}_{FB}(\alpha_0, \delta\xi) = \frac{N_{\alpha_0,\delta}(+\Delta\xi) - N_{\alpha_0,\delta}(-\Delta\xi)}{N_{\alpha_0,\delta}(+\Delta\xi) + N_{\alpha_0,\delta}(-\Delta\xi)} \approx \sum_n A_{n,\delta} sin(n(\alpha_0 - \phi_{n,\delta})) \tag{C.3}$$

where α is the right ascension given by the local sideral time LST (α = LST - ξ).

C.3 Equi - Zenith method

In the Equi - Zenith method ([57]) all the events detected by EAS experiments are collected into different clusters according to their local sidereal time (t) and direction (zenith θ,azimuth ϕ) in the horizontal coordinate system. All the events clusters in the bin centered on (t, θ, ϕ) are considered as coming from the same direction, and the average of $\sum_{\phi' \neq \phi} N_{off}$ (t, θ, ϕ) is used as the background of N_{on} (t, θ, ϕ). (Here ϕ' means that other azimuth bins in the same zenith direction are used to calculate the background of (t, θ, ϕ) except N_{on} (t, θ, ϕ') itself.)

Given the plane configuration of the EAS detectors, the detection efficiency is independent on the azimuth angle for any given zenith band. All the events simultaneously collected in the same zenith band are used as an estimation of the background in order to correct effects caused by environmental variations.

Then the coordinates of N_{on} and N_{off} are converted into equatorial coordinates and all events from different time bins and with different values of θ and ϕ corresponding to the same values of the Ra and Dec, summed; the background N_{bkg} (Ra,Dec) is treated in the same way. From the above discussion, the number of signal and background events are:

$$N(Ra, Dec) = \sum_{t,\theta,\phi} N_{on}(t, \theta, \phi) \quad , \quad N_{bkg}(Ra, Dec) = \sum_{t,\theta,\phi} \frac{\sum_{\phi' \neq \phi} N_{off}(t, \theta, \phi')}{n - 1} \tag{C.4}$$

where n is the number of azimuthal bins at zenith angle θ. A value of a χ^2 function is than calculated, based on the ratio of the observed values of $N_{on}(t, \theta, \phi)$ to the ideal values, I, of the CRs intensity as a function of (t, θ, ϕ). $I_{i,j}$ is defined as the CRs relative intensity for declination bin (j) and right ascension bin (i), while $\frac{N_{t,\theta,\phi}}{I_{i,j}}$ and $\frac{N_{t,\theta,\phi'}}{I_{i',j'}}$ are the number of events and background.

Finally, the χ^2 equation is defined as :

$$\chi^2 = \sum_{t,\theta,\phi} \frac{(\frac{N_{t,\theta,\phi}}{I_{i,j}^{k+1}})^2 - \frac{1}{n_\theta} \sum_{\phi'=1}^{n_\theta} \frac{N_{t,\theta,\phi'}}{I_{i',j'}}}{(\frac{N_{t,\theta,\phi}}{I_{i,j}^{k+1}})^2} \tag{C.5}$$

where k represents the iteration times. After many iterations, a minimized χ^2 value is obtained, and the values of $I_{i,j}$ that provide this minimum.

Bibliography

[1] V. F. Hess. *Uber Beobachtungen der durchdringenden Strahlung bei sieben Freibal-lonfahrten. Phys. Z., 13:1084–1091, 1912.*

[2] Y. S. Yoon *et al. Cosmic-ray Proton and Helium Spectra from the First CREAM Flight. Astrophys. J., 728:122, February 2011. arXiv:1102.2575, doi:10.1088/ 0004-637X/728/2/122..*

[3] R. Abbasi *et al. All-Particle Cosmic Ray Energy Spectrum measured with 26 IceTop Stations.*, arXiv:1202.3039 [astro-ph.HE]

[4] J. Abraham *et al. Measurement of the energy spectrum of cosmic rays above* 10^{18} *eV using the Pierre Auger Observatory. Pierre Auger Collaboration.* Phys. Lett. B 685, 239 (2010)

[5] J. Abraham *et al. Observation of the Suppression of the Flux of Cosmic Rays above* $4 \times 10^{19} eV$. *Phys. Rev. Lett., 101(6):061101, August 2008.* arXiv:0806.4302, doi: 10.1103/PhysRevLett.101.061101.

[6] K. Greisen. *End to the Cosmic-Ray Spectrum? Phys. Rev. Lett., 16:748–750, April 1966.*

[7] G. T. Zatsepin and V. A. Kuz'min. *Upper Limit of the Spectrum of Cosmic Rays. Soviet J. Exp. Theor. Phys., 4:78, August 1966.*

[8] K. Kotera, A.V. Olinto, *The astrophysics of ultrahigh-energy cosmic rays.* Annu. Rev. Astron.Astrophys. 49, 119–153 (2011) arXiv:1101.4256 [astro-ph.HE]

[9] A. Muecke *et al., Monte-Carlo simulations of photohadronic processes in astrophysics. Comput.Phys. Commun. 124, 290–314 (2000).* arXiv:astro-ph/9903478

[10] J. A. M. Bleeker. *The Century of Space Science*. Springer, 2001.

[11] M. Spurio *Particles and Astrophysics. A Multi-Messenger Approach* Astronomy and Astrophysics Library. Springer, 2015

[12] T. K. Gaisser. *Cosmic Rays and Particle Physics.* Cambridge University Press, 1990.

[13] M. Aguilar *et al.*, (AMS-02 collaboration) AMS-02 provides a precise measure of cosmic rays. CERN Courier 53 (2013) 8, 23–26.

[14] A. Obermeier *et al., The boron-to-carbon abundance ratio and galactic propagation of cosmic radiation.* Astrophys J 752, 69 (2012)

[15] E. Fermi. *On the Origin of the Cosmic Radiation. Phys. Rev., 75:1169–1174, Apr1949.*

[16] M.S. Longair, *High Energy Astrophysics, 2nd edn. (Cambridge University Press, Cambridge, 1994).*

[17] A. M. Hillas. *The Origin of Ultra-High-Energy Cosmic Rays.* Annu. Rev. Astron.Astrophys., 22:425–444, 1984.

[18] W. Baade and F. Zwicky. *Cosmic Rays from Super-novae. Proceedings of the National Academy of Science,* 20:259–263, May 1934. doi:10.1073/pnas.20.5.259.

[19] *R. Abbasi et al. An Absence of Neutrinos Associated with Cosmic-Ray Acceleration in γ-Ray Bursts. Nature*, 484:351–354, April 2012. arXiv:1204.4219

[20] Markov, M. A. *On high energy neutrino physics.* in Proceedings of the 10th International Conference on High Energy Physics (1960).

[21] T. Chiarusi, M. Spurio, *High-energy astrophysics with neutrino telescopes.* Eur. Phys. J. C65, 649 (2010)

[22] M. Amram *et al., The ANTARES optical module,* Nucl. Instr. and Meth. A484 (2002) 369-383. or arXiv:astro-ph/0112172

[23] J.A. Aguilar *et al., Study of large hemispherical photomultiplier tubes for the ANTARES neutrino telescope,* Nucl. Instr. and Meth. A555 (2005) 132-141. or arXiv:physics/0510031 [physics.ins-det]

[24] J.A. Aguilar *et al. ANTARES: the first undersea neutrino telescope* Nuclear Inst. and Methods in Physics Research, A 656 (2011) pp. 11-38 or arXiv:1104.1607 [astro-ph.IM]

[25] Aguilar, J. A. et al. (ANTARES Collaboration). *A fast algorithm for muon track reconstruction and its application to the ANTARES neutrino telescope.* Astropart. Phys., 34 (2011), 652 – 662

[26] Heijboer, A. J. *Track Reconstruction and Point Source Searches with ANTARES.* Ph.D. thesis, Amsterdam University (2004).

[27] Bogazzi, C. *Searching for Point Sources of High Energy Cosmic Neutrinos with the ANTARES telescope.* DOI: 10.7529/ICRC2011/V04/0295

[28] Aguilar, J. A. *et al. (ANTARES Collaboration). The data acquisition system for the ANTARES neutrino telescope.* Nucl. Instr. and Meth. A, 570(2007), 107. arXiv:astro-ph/0610029

[29] Aguilar, J. A. et al. (ANTARES Collaboration). *Performance of the front-end electronics of the ANTARES Neutrino Telescope. Nucl. Instr. and Meth. A, 622 (2010), 59* arXiv:1007.2549 [astro-ph.IM]

[30] M. de Jong, *The ANTARES Trigger Software*, ANTARES internal note, ANTARES-SOFT-2005-005.

[31] M. de Jong, *The TriggerEffiency program,*, ANTARES internal note, ANTARES-SOFT-2009-001

[32] C. Riviere. "Run-by-run Monte Carlo simulation for ANTARES: v2". Antares Internal Note, 2012.

[33] D. J. L. Bailey. Genhen v5r1 software documentation, ANTARES internal note, ANTARES-SOFT-2002-004.

[34] P. Antonioli *et al. A three-dimensional code for muon propagation through the rock: MUSIC.* Astroparticle Physics, Vol. 7, No. 4, pp. 357 – 368, 1997 arXiv:hep-ph/9705408

[35] Carminati, G.*et al. MUPAGE: User Guide.* ANTARES internal note, ANTARES-Soft/2007-004.

[36] Navas, S. and Thompson, L. *KM3 user guide and reference manual.* ANTARES internal note, ANTARES-SOFT-1999-011.

[37] G. Ingelman *et al. LEPTO 6.5 - A Monte Carlo generator for deep inelastic lepton-nucleon scattering.* Computer Physics Communications, Vol. 101, No. 1-2, pp. 108 – 134, 1997. arXiv:hep-ph/9605286

[38] A.M. Brown *Positioning system of the ANTARES Neutrino Telescope*, arXiv:0908.0814 [astro- ph.IM]

[39] M. Prouza, R. Smída, *The galactic magnetic field and propagation of ultra-high energy cosmic rays.* Astron. Astrophys. 410, 1–10 (2003) arXiv:astro-ph/0307165

[40] M. Kachelriess. *Lecture Notes on High Energy Cosmic Rays* (2008). arXiv:0801.4376

[41] P. Abreu *et al., Search for first harmonic modulation in the right ascension distribution of cosmic rays detected at the Pierre Auger Observatory.* Astroparticle Physics 34 (2011) 627–639. arXiv:1103.2721. Results updated at the ICRC 2013 (arxiv:1310.4620)

[42] A. H. Compton and I. A. Getting. *An Apparent Effect of Galactic Rotation on Intensity of Cosmic Rays.* Phys. Rev., 47:817–821, Jun 1935. doi:10.1103/PhysRev. 47.817

[43] M. Aglietta *et al., Evolution of the cosmic-ray anisotropy above 10* ^{14} *eV.* Astrophys. J. Lett. 692(2), L130–L133 (2009) arXiv:0901.2740 [astro-ph.HE]

[44] R. Abbasi *et al., Observation of Anisotropy in the Galactic Cosmic-Ray Arrival Directions at 400 TeV with IceCube.* Astrophys J. 746, 33 (2012) arXiv:1109.1017 [hep-ex]

[45] K. Nagashima, K. Fujimoto, and R. M. Jacklyn. *Galactic and Helio tail-in of Cosmic Rays as the Origin of Sidereal Daily Variation in the Energy Region* $< 10^4$ *GeV.* J. Geophys. Res., 103:17429–17440, August 1998. doi:10.1029/98JA01105.

[46] M. Amenomori *et al. Anisotropy and Corotation of Galactic Cosmic Rays. Science*, 314:439–443, 2006. arXiv:astro-ph/0610671

[47] G. Guillian *et al. Observation of the Anisotropy of 10 TeV Primary Cosmic Ray Nuclei Flux with the Super-Kamiokande-I Detector.* Phys. Rev. D, 75(6):062003, Mar 2007. doi:10.1103/PhysRevD.75.062003. arXiv:astro-ph/0508468

[48] A. A. Abdo *et al. The Large Scale Cosmic-Ray Anisotropy as Observed with Milagro.* Astrophys. J., 698:2121–2130, 2009. arXiv:0806.2293

[49] S. Cui *et al. Study on Large-Scale CR Anisotropy with ARGO-YBJ Experiment.* In Proc. of the 32 nd ICRC, Beijing, China, July 2011. ID 0041. doi:10.7529/ICRC2011/V01/0041.

[50] S. Fukuda *et al. The Super-Kamiokande detector*, Nucl. Instr. Meth. A 501, 418 (2003).

[51] Atkins, R., *et al. TeV Gamma-Ray Survey of the Northern Hemisphere Sky Using the Milagro Observatory.* arXiv:astro-ph/0403097

[52] J. Linsley, Phys. Rev. Lett. 34 (1975) 1530

[53] M. G. Aartsen *et al. Evidence for High-Energy Extraterrestrial Neutrinos at the IceCube Detector* , arXiv:1311.5238 [astro-ph.HE]

[54] Luis A. Anchordoqui *et al. Large Scale Anisotropy of Cosmic Rays and Directional Neutrino Signals from Galactic Sources* arXiv:1403.6628 [astro-ph.HE]

[55] L. A. Anchordoqui *et al. Pinning down the cosmic ray source mechanism with new IceCube data.*, arXiv:1306.5021 [astro-ph.HE].

[56] R.Bonino *et al. The East-West method: an exposure-independent method to search for large scale anisotropies of cosmic rays* arXiv:1106.2651 [astro-ph.IM]

[57] T.Li *et al. Evaluation of a wide-sky survey method for EAS experiments.* doi:10.1016/j.astropartphys.2012.11.001

[58] Gandhi, R. *et al. Ultrahigh-Energy Neutrino Interactions.* Astroparticle Physics, 5 (1996), 81–110.

[59] Labbate, A. *et al. Effect of neutral current interactions on high energy muon and electron neutrino propagation through the Earth.* Astropart. Phys., 23 (2005), 57 – 63. arXiv:hep-ph/0406133

[60] M. Ambrosio *et al. (MACRO coll.), Seasonal variations in the underground muon intensity as seen by MACRO* Astropart. Phys. 7 (1997) 109.

[61] P. Adamson *et al. Observation of muon intensity variations by season with the MINOS Near Detector.* arXiv:1406.7019 [hep-ex]

[62] G. Bellini *et al. Cosmic-muon flux and annual modulation in Borexino at 3800 m water-equivalent depth*, J. Cosm. Astropart. Phys. 1205, 015 (2012); hep-ex:1202.6403. arXiv:1202.6403 [hep-ex]

[63] ECMWF www.ecmwf.int/